Personalized and Tissue-Specific Melt Electrowritten Scaffolds for Coordinated Regeneration of Soft and Hard Periodontal Tissues

by

Arwa Daghrery

A dissertation submitted in partial fulfillment
of the requirements for the degree of
Doctor of Philosophy
(Oral Health Sciences)
In the University of Michigan
2021

Doctoral Committee:

Associate Professor Marco Bottino, Chair
Associate Professor Darnell Kaigler
Professor Yuji Mishina
Professor Jan Stegemann

Arwa Daghrery

daghrery@umich.edu

ORCID iD: 0000-0002-8328-1818

Dedication

To my husband, Ahmed, for his love and endless support, and for every sacrifice he has made to help me achieve my dream. To my children, Zeyad, Trki, and Ali, for the warmth, brightness, and the joy they bring into my life every single day. To my parents, Ali and Zabna Daghrery, for their continuous belief in me and the encouragement they have never ceased to provide me since childhood. To my sisters and brothers for always uplifting me with their unconditional love.

Acknowledgements

I am incredibly grateful to have had the opportunity to pursue my doctorate in oral health sciences at the University of Michigan, and for the chance to collaborate with scientists who are not only leaders within their field, but also great personal inspirations. I would like to express my sincere gratitude to my doctoral committee for their guidance and valuable advice throughout the duration of this work: Dr. Marco Bottino, Dr. Yuji Mishina, Dr. Darnell Kaigler, and Dr. Jan Stegemann.

I deeply appreciate the mentorship and guidance of my thesis advisor, Dr. Marco Bottino. I have thoroughly enjoyed having the chance to contribute to a wide variety of projects and be exposed to the new and exciting field of 3D printing. Thank you, Dr. Yuji Mishina, for being a source of unlimited guidance in my development, from my early beginnings when I first joined the OHS PhD program. Your belief in my abilities has kept me motivated throughout every obstacle. Thank you to Dr. Kaigler for providing meaningful feedback for my data analysis and insightful advice on interpreting the data. I am filled with gratitude for the advice and guidance I have received. Thank you to Dr. Stegemann for his continuous support and advice on data interpretation and presentation. I appreciate the insights provided by Dr. Brian Clarkson and Sywe-Ren Chang in manufacturing the novel F/CaP coating on the melt electrowritten scaffold developed in this thesis. I thank Dr. Sarit Bhaduri, Jos Malda, and Miguel Castilho for contributing their time and knowledge to the critical analysis of the data presented.

I would like to thank all members of the Bottino laboratory for their kindness and assistance with experimental design, animal studies, and insightful feedback: Jinping Xu, Jessica A. Ferreira, and Isaac J. de Souza Araújo.

I thank Honghao Zhang and all members of the Yuji Mishina laboratory, for their helpfulness, training, and unique scientific perspectives during my first laboratory rotation. Thank you to Han Kyoung Choi and all members of Dr. Fei Liu's laboratory—I appreciate all the limitless support and amazing experience I gained during my second laboratory rotation.

Several staff from Core Facilities across the entire University of Michigan were generous with their time and valuable discussion. I want to thank Taocong Jin at the Molecular Biology Core Laboratory for all his help and support with my PhD work. Thank you to Chris Strayhorn (School of Dentistry, Histology Core) and Michelle Lynch (School of Dentistry, micro-CT Core) for their help with sample preparation and analysis. Thank you to Zhongrui Li for training and explaining numerous details associated with XRD. Thank you Nancy S. Muyanja and Haiping Sun from the Michigan Center for Materials Characterization for my training in scanning electron microscopy (SEM) and energy dispersive x-ray spectroscopy (EDAX) Thank you Binyamin Jacobovitz from microscopy core for training with confocal imaging. Thank you to James Windak from the School of Chemistry for my training with FTIR, DSC, and TGA. Thank you, Damon Hoff, from the SMART Center, for my training with AFM. I want to thank all clinical faculties from the CRSE Department; it has been a genuine pleasure working with all of you. I give special thanks to Dr. Ronald Heys, Dr. Peter Yaman, and Dr. Joseph Dennison for their unlimited support. I thank the entire committee of the Oral Health Sciences Master's Program: Dr.

Elisabeta Karl, Dr. Darnell Kaigler, Dr. Daniel Chiego, Dr. Livia Tenuta, and Amy Watson. Serving on the committee has been an incredible experience and I am certain that everything I have learned from your expertise will continue to help me in my future career as a faculty member.

I would like to thank Dr. Vesa Kaartinen, our program director, and Kimberly Smith for always being there to support and care not only about me, but my family, as well.

Thank you to my funding agency from my home country of Saudi Arabia, Jazan University, Faculty of Dentistry in Jazan, for supporting me financially as I pursued a master's degree and PhD from the University of Michigan. Thank you to all the academic advisors and staff at the Saudi Cultural Mission for their help and support these past several years.

I would like to thank my friends, Hadise Kabil and Heba Mitwalli, for all their encouragement, support, and for always lending me a friendly ear.

Finally, I want to thank my beloved husband, who has shown me patience and devotion at every turn. Making you and our children proud has been my most precious source of motivation.

Table of Contents

List of Figures

Abstract

Periodontitis is a chronic inflammatory, bacteria-triggered disorder affecting nearly half of American adults. If left untreated, it leads to severe destruction of the periodontium, *i.e.*, the alveolar bone, periodontal ligament (PDL), and cementum, ultimately leading to tooth loss. Current clinical therapeutic approaches include subgingival scaling, periodontal flap surgery, guided tissue regeneration (GTR), and guided bone regeneration (GBR).[1] The formation of new bone, cementum, and periodontal ligament (PDL) is a possible objective of these modalities; however, outcomes are not always predictable, due to varying degrees of destruction and highly complex tissue architecture. This underscores the urgent need for superior strategies to amplify regenerative capacity, regardless of damage severity.

Melt electrowriting (MEW) is a novel strategy that allows customization to the desired size, configuration, and architecture of a given scaffold. It allows for the production of consistent fiber morphology and diameter approaching submicron magnitudes, which, in turn, allows for the recapitulation of the tissue-specific cell microenvironment. Thus, a MEW-based approach to form fiber-guiding scaffold would offer a geometric organization for bone-PDL interface.

In this dissertation work, we show the potential of highly ordered scaffolds engineered via melt electrowriting (MEW) in guiding soft (PDL) and hard (bone) periodontal tissue regeneration. Our *in vitro* findings show that the presence of the aligned fibers result in a robust expression of ligamentogenic markers, while the strands' spacing

of MEW constructs play a vital role in the upregulation of osteogenic markers. Moreover, *in vitro* findings strongly suggest that aligned and porous MEW constructs promote macrophage elongation and further polarization toward M2 macrophage, the prohealing phenotype. Meanwhile, the incorporation of osteoconductive fluorinated calcium phosphate coating, has been shown to positively impact mineralized tissue formation. The fiber morphology of F/CaP-coated scaffolds revealed a unique nanostructured surface depicted as irregular-shaped nanoparticles (~ 50-150 nm) and a homogenous rough layer covering each individual fiber. The presence of a nanostructured F/CaP coating led to a marked upregulation of osteogenic genes and attenuated bacterial growth. The reduced bacterial growth, even with a rougher F/CaP coated surface, suggests an antimicrobial action due to the coating's composition.

Collectively, to regenerate tissue-specific architecture and recapitulate the physiological function of native periodontal tissues, a scaffold with tailored properties and bioactive functional was developed. Altogether, our findings confirmed that the tissue-specific scaffolds with F/CaP-coated, bone compartment, and aligned PDL compartment are biocompatible and lead to periodontal tissue regeneration when implanted in a well-established rat mandibular periodontal fenestration defect model.

CHAPTER 1

Introduction

1.1 Problem Statement

Periodontitis is a chronic inflammatory disease affecting approximately 47% of adults 30 years of age and older. If left untreated, it leads to severe destruction of the periodontium; *i.e.*, the alveolar bone, periodontal ligament (PDL), and cementum, eventually ending in tooth loss.[1,2] The goal of periodontics has been to regenerate the tooth-supporting structures that have been destroyed because of disease progression. Subgingival scaling, periodontal flap surgery, guided tissue regeneration (GTR), and guided bone regeneration (GBR) are some of the current clinical therapeutic modalities.[3] The formation of new bone, cementum, and periodontal ligament (PDL) is a possible objective of these modalities; however, outcomes are not always predictable.

Despite evidence that some level of tissue regeneration may occur following a regenerative procedure,[4] complete regeneration may be an unrealistic goal in many situations partly due to the complexity of the periodontal tissue architecture. The ligament component of the periodontium is a multifunctional fibrous tissue and plays a crucial role in optimizing various biomechanical and biophysical responses to the masticatory force.[4] Therefore, the acquisition of well-oriented PDL fibers with alveolar bone regeneration is of great significance in periodontal tissue engineering.

Biomaterial-based strategies, which provide 3D templates and biomimetic extracellular matrix (ECM) environments, have been utilized for periodontal tissue regeneration.[5] While significant advances have been made in scaffold-based approaches, these models fail to recapitulate the native architecture and mechanical properties of the native PDL-alveolar bone.[7] Collectively, designing scaffolds to closely mimic native tissue might be helpful for enhanced PDL and bone formation through improving the microstructure and perhaps the function of regenerated tissue.[8]

Many attempts to treat large defects and regenerate lost periodontal complex (bone-PDL-cementum) have utilized additive manufacturing (AM) techniques (*e.g.*, fused deposition modeling (FDM) and selective laser sintering (SLS) to manufacture scaffolds.[9] These scaffolds have low spatial resolution, and are often several orders of magnitude larger than native ECM fibers—mainly collagen fibrils—resulting in poor cell-seeding efficiency and proliferation, and uneven scaffold coverage.[6]

Nanofibrous scaffolds produced by electrospinning (ESP) are an interesting alternative and have been presented to promote cell attachment and stimulate cell function. Solution electrospinning (ES) is one of the most popular methods for fabricating nanofibrous scaffolds, because it is simple to use, reasonably affordable, and versatile in terms of polymer selection and incorporation of biologically active compounds (*e.g.*, growth factors).[7] However, the ES technique results in subsequent layers of deposition and, thus, compresses the layers below, creating a flat, densely packed structure, thus limiting cellular growth and infiltration.[8]

Over the past decade, there has been increasing interest in accurately depositing electrospun fibers using approaches, such as short spinneret/collector distances, pre-

structured substrates, and controlled electric fields. Controlling the deposition of ESP fibers would allow fiber creation in a direct writing mode.[6,9] The principles of thermal polymer extrusion and electrospinning have been combined in melt electrowriting (MEW). [9] The application of an electrical field to draw a molten polymer directly and continuously out of a spinneret towards a computer-controlled collector plate, allows highly-ordered fiber deposition and stacking to create 3D scaffolds. [9,10] MEW combines the surface benefits of ESP fibrous scaffolds with the repeatability and design capabilities of AM methods.[9] In MEW, the produced fibers' diameter reaches 2 μm to 20 μm.[10] The microscale diameter of MEW fibers offers the potential to create true 3D structures with cell invasive ability, which, so far, are difficult to obtain using ESP.[6]

The patterns can be created using the collector with predefined *XY* translation, and the fibers are stacked to build 3D constructs.[11] In this way, utilizing MEW to fabricate a multiscale scaffold that allows for compartmentalized tissue healing and utilizes a tissue-specific structure is a key to controlling the spatiotemporal events leading to periodontal regeneration. Such a scaffold will allow for the simultaneous regeneration of soft and hard tissues.

Our approach focuses on using 3D printed MEW to obtain a scaffold presenting features on the macro (scaffold structure), micro (pore size for the bone compartment and fiber alignment for PDL compartment), and nanoscale (surface topography) levels for the guidance of bulk and oriented tissue formation of both mineralized and soft tissues. The experimental elements in this work emphasize the development and evaluation of a novel biphasic scaffold for integrated tissue regeneration. The innovation lies in the rational design of a complex scaffold system that facilitates the regeneration of soft and hard

periodontal tissues in a coordinated manner. The broader implications of this work include the elucidation of interactions between biomaterial substrates and cells, guiding cellular commitment toward osteogenic and/or ligamentogenesis formation and providing a critical insight into the factors that guide cell differentiation into tissue-specific lineages.

1.2 Existing Limitations of Current Periodontal Regenerative Therapies

Periodontal tissues destruction might occur because of cancer, severe trauma, congenital abnormality, and progressive destructive diseases. The damage compromises the function of the complex soft and hard tissues of the periodontium, leading to irreparable deformity. [2,12,13] The periodontium is composed of (PDL), cementum, gingiva, and alveolar bone that support teeth. Progressed periodontal tissue destruction compromises the alveolar bone and undermines the surrounding apparatus, subsequently leading to tooth loss. Current clinical treatment approaches include subgingival scaling and root planing, periodontal flap, guided tissue regeneration, and guided bone regeneration (GTR/GBR).[2]

Meanwhile, autologous bone grafts have widely been used to reconstruct craniofacial bone, *e.g.*, alveolar bone. Despite success in avoiding complications associated with allograft or xenograft, such as immunogenicity, this approach is associated with vast morbidity and the need for multiple surgeries accompanied by other complications and infection,[14] particularly if the graft fails to confer the anatomy of the craniofacial region due the shape of multitissue structures.

Remarkably, resorbable and non-resorbable membranes have been also utilized for periodontal tissue regeneration; they are combined with osteoconductive materials

(*i.e.,* calcium phosphates, bioactive glass) or growth factors, such as platelet-derived growth factor (PDGF), bone morphogenetic proteins (BMPs), and fibroblast growth factor (FGF).

GTR is a membrane-based approach applied to hinder epithelial tissues down growth into the defect area to prevent formation of long, junctional epithelium. Thus, it stabilizes the space, while providing a niche for host progenitor cells to recolonize and differentiate into new attachment apparatus.[3,10]

While significant advances have been made in scaffold-based approaches, these strategies failed to recapitulate the native architecture and mechanical properties of the native PDL-alveolar bone.[15] Many preclinical investigations endeavored to regenerate large periodontal defects using scaffolds fabricated via AM techniques.[16] The resolution (*i.e.*, fiber diameter) of the generated scaffolds are often many orders of magnitude larger than the collagen fibers of ECM, particularly collagen fibrils, resulting in poor cell seeding efficiency and proliferation, as well as nonuniform scaffold coverage.[10] Importantly, nanofibrous scaffolds produced by solution electrospinning (ES) (ESP) are an interesting, versatile alternative in terms of polymer selection and incorporation of biologically active compounds to support cell attachment and activity.[17] However, the ES technique results in uncontrolled compressed layers' deposition, thus creating a flat, densely-packed structure, hence limiting cellular growth and infiltration.[17]

Over the past decade, there has been a growing interest in accurately depositing electrospun fibers; using approaches provides controlled fiber deposition and reproducibility over scaffold design in a direct writing mode. Successfully, MEW has

shown superiority in fabricating scaffolds with predefined design using FDA-approved polymers, such as poly(ε-caprolactone) (PCL).[6]

The scaffold design for periodontal tissue has several potentially detrimental factors related to cellular infiltration and tissue ingrowth.[18] In general, pore size and interconnectivity, and appropriate mechanical properties have been acknowledged as the most important scaffold design parameters.[6] The aforementioned key substrates' structural parameters can be used to control differentiation and tissue formation.[24]

The scaffold's pore sizes and interconnectivity, which refer to space between the walls and connection between these pores along the construct**,** influence a range of cellular processes, diffusion of nutrients, metabolites, and waste products.[8] A pore size range between 150 μm and 1500 μm has been investigated for applications in bone tissue engineering, thus allowing for cellular growth and vascularization.[8,19] Furthermore, fibrous tissue orientations play an important role in improving the biomechanical and biophysical responses of PDLs.[20] Angulated PDLs between the teeth and alveolar bone, in particular, play a key role in masticatory/occlusal stress absorption and distribution, as well as optimization of mineralized tissue remodeling.

However, a challenging limitation for controlling the perpendicular angulations of ligamentous bundles remains. A fiber-guiding scaffold strategy could favor the formation and integration of key structures of the tooth-ligament-bone interface.[15] Guiding cells in a structurally relevant direction via substrate has been shown to stimulate cell behavior when creating organized tissues, thus mimicking their native form and function, including cardiac and nerve tissue.[21] Given the limitations of the current periodontal regenerative approach, the main goal of this research is to utilize 3D printed-MEW to obtain a scaffold

presenting features on the macro (scaffold structure), micro (pore size for bone compartment and fiber alignment for PDL compartment), and nanoscale (surface topography) levels to guide both bulk and oriented tissue formation of mineralized and soft periodontal tissues.

1.3 Thesis Aims

Current clinical periodontal regenerative approaches have limited potential to simultaneously guide multi-tissue regeneration. To address these limitations, this work emphases to develop multiscale scaffold competent to regenerate both soft and mineralized periodontal tissues. The **overall objectives** are: (i) develop a scaffold that can positively influence cell behavior and fate to simultaneously drive mineralized and soft tissue formation, and (ii) understand the effects of scaffold architecture to guide periodontal regeneration using both *in vitro* and *in vivo* models. The results of this work will have a positive impact by establishing a feasible strategy in scaffold design to better understand the clinical potential of scaffold architecture to improve periodontal regeneration outcomes. We anticipate the findings will lead to novel regenerative periodontics therapeutics to be further validated using clinically relevant large animal models.

AIM 1: To fabricate 3D-printed highly porous MEW scaffold capable of promoting bone formation and evaluating biological function both *in vitro* and *in vivo.*

Hypothesis 1: 3D-printed, highly porous MEW scaffold will provide greater capacity to promote bone formation.

AIM 2: To fabricate 3D-printed scaffolds with different orientations and examine their effectiveness in creating *a local environment for periodontal tissue engineering via "*Immune-Osteogenic/ligamentogenic-informed" biomaterials.

Hypothesis 2: Highly oriented 3D-printed scaffolds will create a local environment for periodontal tissue engineering via "Immune-Osteogenic/ligamentogenic-informed" biomaterials.

AIM 3: To fabricate 3D scaffolds with Bone/PDL tissue-specific complexity and evaluate the biological effectiveness of the scaffolds using the periodontal fenestration defect repair model.

Hypothesis 3: 3D-printed MEW scaffold with Bone/PDL tissue-specific complexity will facilitate coordinated guidance for soft and hard periodontal tissue regeneration in vivo.

1.4 Dissertation Contents

Chapter 2 of this dissertation provides an in-depth review of the 3D-printed Melt electrowriting principle and its potential application for bone and periodontal ligament regeneration, in addition to covering the most advanced hierarchical scaffolds for multi tissue and tissue interface regeneration that promotes soft and hard tissue regeneration. **Chapter 3** presents a distinctive design of a 3D-printed MEW, defect-specific scaffold for periodontal regeneration capable of enabling the differentiation of resident progenitor cells, thus guiding the coordinated growth of soft and hard periodontal tissues, while

affording antimicrobial properties. Additionally, in this chapter we also investigated limitations of the current design that guided us toward the modifications presented in Chapter 4. **Chapter 4** explores the potential of a collagen-infused construct to enhance vascularization and tissue infiltration in the subcutaneous model for further exploration of this approach for the development of 3D-printed highly aligned/porous MEW-infused collagen scaffolds to promote simultaneous collagenous soft tissue and osseous tissue formation, with a particular focus on exploring the *in vitro* immunomodulatory potential and identifying scaffold fiber configuration (alignment), which is optimal for cellular alignment that leads to tissue alignment and further explores the potential of scaffold design to direct the hierarchical formation of bone and PDL. **Chapter 5** provides important relevant statements that collectively summarize the results obtained in Chapters 3-4: the innovation, advantage, disadvantage of this approach, and limitations. Finally, the potential application and outlook towards supporting periodontal and bone regeneration is discussed.

1.5 References

(1) Eke, P. I.; Dye, B. A.; Wei, L.; Slade, G. D.; Thornton-Evans, G. O.; Borgnakke, W. S.; Taylor, G. W.; Page, R. C.; Beck, J. D.; Genco, R. J. Update on Prevalence of Periodontitis in Adults in the United States: NHANES 2009 – 2012. *J Periodontol* **2015**, *86* (5), 611–622. https://doi.org/10.1902/jop.2015.140520.

(2) Bottino, M. C.; Thomas, V.; Schmidt, G.; Vohra, Y. K.; Chu, T.-M. G.; Kowolik, M. J.; Janowski, G. M. Recent Advances in the Development of GTR/GBR Membranes for Periodontal Regeneration—A Materials Perspective. *Dental Materials* **2012**, *28* (7), 703–721. https://doi.org/10.1016/j.dental.2012.04.022.

(3) Bottino, M. C.; Thomas, V.; Janowski, G. M. A Novel Spatially Designed and Functionally Graded Electrospun Membrane for Periodontal Regeneration. *Acta Biomater* **2011**, *7* (1), 216–224. https://doi.org/10.1016/j.actbio.2010.08.019.

(4) Gauthier, R.; Jeannin, C.; Attik, N.; Trunfio-Sfarghiu, A.-M.; Gritsch, K.; Grosgogeat, B. Tissue Engineering for Periodontal Ligament Regeneration: Biomechanical Specifications. *Journal of Biomechanical Engineering* **2020**, *143* (3). https://doi.org/10.1115/1.4048810.

(5) Kim, J. H.; Park, C. H.; Perez, R. A.; Lee, H. Y.; Jang, J. H.; Lee, H. H.; Wall, I. B.; Shi, S.; Kim, H. W. Advanced Biomatrix Designs for Regenerative Therapy of Periodontal Tissues. *J Dent Res* **2014**, *93* (12), 1203–1211. https://doi.org/10.1177/0022034514540682.

(6) Robinson, T. M.; Hutmacher, D. W.; Dalton, P. D. The Next Frontier in Melt Electrospinning: Taming the Jet. *Advanced Functional Materials* **2019**, *29* (44), 1904664. https://doi.org/10.1002/adfm.201904664.

(7) Daghrery, A.; Aytac, Z.; Dubey, N.; Mei, L.; Schwendeman, A.; Bottino, M. C. Electrospinning of Dexamethasone/Cyclodextrin Inclusion Complex Polymer Fibers for Dental Pulp Therapy. *Colloids and Surfaces B: Biointerfaces* **2020**, 111011. https://doi.org/10.1016/j.colsurfb.2020.111011.

(8) Loh, Q. L.; Choong, C. Three-Dimensional Scaffolds for Tissue Engineering Applications: Role of Porosity and Pore Size. *Tissue Eng Part B Rev* **2013**, *19* (6), 485–502. https://doi.org/10.1089/ten.teb.2012.0437.

(9) Chen, F.-M.; Liu, X. Advancing Biomaterials of Human Origin for Tissue Engineering. *Prog Polym Sci* **2016**, *53*, 86–168. https://doi.org/10.1016/j.progpolymsci.2015.02.004.

(10) Dubey, N.; Ferreira, J. A.; Malda, J.; Bhaduri, S. B.; Bottino, M. C. Extracellular Matrix/Amorphous Magnesium Phosphate Bioink for 3D Bioprinting of Craniomaxillofacial Bone Tissue. *ACS Appl. Mater. Interfaces* **2020**, *12* (21), 23752–23763. https://doi.org/10.1021/acsami.0c05311.

(11) Muerza-Cascante, M. L.; Haylock, D.; Hutmacher, D. W.; Dalton, P. D. Melt Electrospinning and Its Technologization in Tissue Engineering. *Tissue Eng Part B Rev* **2015**, *21* (2), 187–202. https://doi.org/10.1089/ten.TEB.2014.0347.

(12) Dwivedi, R.; Kumar, S.; Pandey, R.; Mahajan, A.; Nandana, D.; Katti, D. S.; Mehrotra, D. Polycaprolactone as Biomaterial for Bone Scaffolds: Review of Literature. *J Oral Biol Craniofac Res* **2020**, *10* (1), 381–388. https://doi.org/10.1016/j.jobcr.2019.10.003.

(13) Petrovic, V.; Zivkovic, P.; Petrovic, D.; Stefanovic, V. Craniofacial Bone Tissue Engineering. *Oral Surgery, Oral Medicine, Oral Pathology and Oral Radiology* **2012**, *114* (3), e1–e9. https://doi.org/10.1016/j.oooo.2012.02.030.

(14) Du, Y.; Guo, J. L.; Wang, J.; Mikos, A. G.; Zhang, S. Hierarchically Designed Bone Scaffolds: From Internal Cues to External Stimuli. *Biomaterials* **2019**, *218*, 119334. https://doi.org/10.1016/j.biomaterials.2019.119334.

(15) Pilipchuk, S. P.; Fretwurst, T.; Yu, N.; Larsson, L.; Kavanagh, N. M.; Asa'ad, F.; Cheng, K. C. K.; Lahann, J.; Giannobile, W. V. Micropatterned Scaffolds with Immobilized Growth Factor Genes Regenerate Bone and Periodontal Ligament-Like Tissues. *Adv Healthc Mater* **2018**, *7* (22), e1800750. https://doi.org/10.1002/adhm.201800750.

(16) Rasperini, G.; Pilipchuk, S. P.; Flanagan, C. L.; Park, C. H.; Pagni, G.; Hollister, S. J.; Giannobile, W. V. 3D-Printed Bioresorbable Scaffold for Periodontal Repair: *Journal of Dental Research* **2015**. https://doi.org/10.1177/0022034515588303.

(17) Blakeney, B. A.; Tambralli, A.; Anderson, J. M.; Andukuri, A.; Lim, D.-J.; Dean, D. R.; Jun, H.-W. Cell Infiltration and Growth in a Low Density, Uncompressed Three-Dimensional Electrospun Nanofibrous Scaffold. *Biomaterials* **2011**, *32* (6), 1583–1590. https://doi.org/10.1016/j.biomaterials.2010.10.056.

(18) Carter, S.-S. D.; Costa, P. F.; Vaquette, C.; Ivanovski, S.; Hutmacher, D. W.; Malda, J. Additive Biomanufacturing: An Advanced Approach for Periodontal Tissue Regeneration. *Ann Biomed Eng* **2017**, *45* (1), 12–22. https://doi.org/10.1007/s10439-016-1687-2.

(19) Filippi, M.; Born, G.; Chaaban, M.; Scherberich, A. Natural Polymeric Scaffolds in Bone Regeneration. *Front. Bioeng. Biotechnol.* **2020**, *8*. https://doi.org/10.3389/fbioe.2020.00474.

(20) Pilipchuk, S. P.; Monje, A.; Jiao, Y.; Hao, J.; Kruger, L.; Flanagan, C. L.; Hollister, S. J.; Giannobile, W. V. Integration of 3D Printed and Micropatterned Polycaprolactone Scaffolds for Guidance of Oriented Collagenous Tissue Formation In Vivo. *Adv Healthc Mater* **2016**, *5* (6), 676–687. https://doi.org/10.1002/adhm.201500758.

(21) Jiang, W.; Li, L.; Zhang, D.; Huang, S.; Jing, Z.; Wu, Y.; Zhao, Z.; Zhao, L.; Zhou, S. Incorporation of Aligned PCL–PEG Nanofibers into Porous Chitosan Scaffolds Improved the Orientation of Collagen Fibers in Regenerated Periodontium. *Acta Biomaterialia* **2015**, *25*, 240–252. https://doi.org/10.1016/j.actbio.2015.07.023.

Park, C. H.; Rios, H. F.; Jin, Q.; Sugai, J. V.; Padial-Molina, M.; Taut, A. D.; Flanagan, C. L.; Hollister, S. J.; Giannobile, W. V. Tissue Engineering Bone-Ligament Complexes Using Fiber-Guiding Scaffolds. *Biomaterials* **2012**, *33* (1), 137–145. https://doi.org/10.1016/j.biomaterials.2011.09.057.

CHAPTER 2

Unveiling The Potential of Melt Electrowriting in Regenerative Dental Medicine

Abstract

For nearly three decades, tissue engineering strategies have been leveraged to devise effective therapeutics for dental, oral, and craniofacial (DOC) tissues regeneration and treat permanent deformities caused by many debilitating health conditions. In this regard, additive manufacturing (AM) allows the fabrication of personalized scaffolds that have the potential to recapitulate native tissue architecture and biomechanics through several 3D printing techniques. Among these, melt electrowriting (MEW) is a versatile direct writing process that allows the development of well-organized fibrous constructs with fiber resolutions ranging from micron to nanoscale. Precisely, MEW offers great prospects for the fabrication of scaffolds mimicking tissue specificity, healthy and pathophysiological microenvironments, personalized multi-scale transitions, and functional interfaces for tissue regeneration in medicine and dentistry. Worth noting, MEW can be converged with other AM technologies and cell-laden scaffold fabrication (bioprinting) for multi-tissue compartmentalization, interconnectivity, and predetermined cell commitment. Here, we first present the engineering principles of MEW and the most relevant design aspects for transition from flat to more anatomically relevant 3D structures while printing highly-ordered constructs. Secondly, we provide a critical appraisal of contemporary achievements using melt electrowritten scaffolds to study and guide soft and hard tissue

regeneration and draw a parallel on how to extrapolate proven concepts for applications in DOC tissue regeneration. Finally, we offer a combined engineering/clinical perspective on the fabrication of hierarchically organized MEW scaffold architectures and the future translational potential of site-specific, single-step scaffolds to address tissue and tissue interfaces in regenerative dental medicine.

Keywords: melt electrowriting, 3D printing, biofabrication, dentistry, regeneration, scaffolds.

2.1 Introduction

Numerous health conditions, such as cancer, severe trauma, congenital deformity, and progressive destructive diseases, may compromise and damage the function of complex tissues in the craniofacial region, including bone, cartilage, and soft tissues, leading to irreparable deformity.[1–3] As a result, a plethora of reconstructive therapies have been described in the literature since the inception of the field of tissue engineering. However, these reconstructions primarily focus on repairing bone defects using graft materials from either autologous, homologous, or heterologous sources.[3] Despite the osteoinductive outcomes achieved with bone grafts, the need for two surgical areas, the extended morbidity for autologous grafts and the variable results from the allogenic and xenogeneic grafts,[4] continue to pose significant clinical concerns. For this, the concepts of regenerative medicine and bone tissue engineering have emerged to overcome the shortcomings of traditional reconstructive techniques.

Over the last decades, countless approaches have been proposed following the principles of tissue engineering to develop safe and effective therapies for dental, oral, and craniofacial (DOC) tissues regeneration **(Fig. 1)**. In essence, approaches involving

the utilization of scaffolds, biomolecules (*e.g.*, growth factors), and/or cells have been offered to repair or regenerate DOC tissues.[3] To that end, a range of biomaterials, including polymers (natural and synthetic), ceramics and composites have been used in the fabrication of scaffolds, *i.e.*, matrices for facilitating the migration, support or transport of cells and/or biomolecules to encourage tissue neoformation. Importantly, biomaterial-based scaffolds must not only recapitulate the three-dimensional (3D) architecture of the extracellular matrix (ECM) of native tissues, but also its tissue-specific mechanics and biochemical features for functional tissue regeneration.[3]

Since its establishment, the field of regenerative medicine has stimulated considerable advances in the creation of biomimetic scaffold templates of the ECM through several techniques, including, but not limited to, electrospinning, solvent casting/particulate-leaching, thermally induced phase separation, among others.[3] Noteworthy, although the conventional, solution-based electrospinning has been regarded as a versatile, facile, and reasonably inexpensive fabrication method,[5,6] the lack of control over fiber deposition results in formation of densely-packed sheet-like structure that limits cellular infiltration and vascularization.[5–7] On the other hand, AM technologies have emerged as a potential solution to engineer scaffolds capable of replicating the complex 3D organization of human tissues. For instance, fused deposition modeling (FDM), which is based on the selective dispensing of a molten polymer through a nozzle, allows for the generation of mechanically-robust 3D scaffolds and implants.[8] Recently, aiming at the fabrication of 3D scaffolds and implants that combine conflicting properties such as mechanical performance and high porosity, the concept of digital design via optimization techniques or parametric design has been coupled with AM technologies.[9–

[13] Regrettably, while FDM-processed scaffolds can be modified with bioceramics to afford better biological properties, for example in bone tissue engineering applications,[8,14,15] these scaffolds present low spatial resolution, and morphological features that are several orders of magnitude larger than native ECM, and therefore not able to resemble the digital designed, computational optimized model.[6,16] Thus, aiming to circumvent the low resolution of scaffolds processed via FDM and the poor organization of electrospun alternatives, the principles of thermal polymer extrusion and electrospinning have been combined in a process titled Melt Electrospinning Writing, or simply Melt ElectroWriting (MEW).[16,17]

MEW consists on the application of an electrical field to draw a molten polymer directly and continuously out of a spinneret towards a computer controlled planar or rotating collector plate **(Fig. 2A-B)**.[18–20] The collector substrate translates at a speed close to that of the jet which allows highly-ordered fiber deposition and stacking to create 3D scaffolds and architectures.[17] Hitherto, MEW has demonstrated to be a major enabling tool in regenerative medicine, capable of generating highly-ordered porous structures with fiber filaments ranging from a few hundred nanometers to several microns.[17,21–23] This 3D printing technology is distinct from others in that the high fiber diameter resolution (nano/micrometer) is accompanied with the capability to print one-centimeter thick 3D structures.[22] This differs from other extrusion-based 3D printing technologies, like FDM, that have filament diameter resolution limits around 100 μm or are restricted in fabricating macroscale volume objects. In fact, the highly defined architecture is the reason why MEW processed structures provide great potential for engineering tissue-specific ECM-like scaffolds, pathophysiological microenvironments, personalized and functional

implants for DOC tissue regeneration, as well as very recently for the precise patterning of cell-laden, micron-scale biomaterial fiber.[24] Here, we offer a brief, yet critical review of the physical principles of MEW and the key aspects involved in the design of tissue- and interface-specific scaffolds for applications in regenerative dental medicine. To the best of our knowledge, we offer first-hand perspective on its untapped potential in DOC tissue regeneration with emphasis in the regeneration of mineralized craniofacial tissues, as well as tissue interfaces (*e.g.*, bone-periodontal ligament). As a future outlook, we highlight upcoming directions associated with the use of MEW as a versatile technology for personalized and functional scaffolds for DOC tissue regeneration and as 3D *in vitro* platform for investigating head and neck tumors.

2.2 Melt Electrowriting – Physical Principles

To surpass issues regarding fiber orientation and layer organization, in addition to incomplete solvent evaporation commonly associated with solution electrospinning, polymer melts have been used to fabricate constructs with controlled fiber diameter, pore size, and 3D architecture. Poly(ε-caprolactone) [PCL] has been the most amenable polymer for MEW, due to its relatively low melting point, semi-crystallinity and rapid solidification, stable thermal and rheological properties, and biocompatibility.[25] Although a range of degradable and non-degradable polymers has been used to obtain MEW scaffolds and constructs, such as polypropylene (PP), a photocurable poly(l-lactide-co-ε-caprolactone-co-acryloyl carbonate), and water-soluble poly(2-ethyl-2-oxazoline), none of them reached (yet) the accuracy of the constructs processed with PCL.[26] Apart from that, to surpass low elastic properties of PCL, thermoplastic elastomers (TPE) materials

can be melt-processed by thermoplastic techniques and exhibit low stiffness like elastomers and can be used to fabricate scaffolds through MEW.[26]

MEW was conceptualized to achieve better control over fiber deposition and orientation from polymer melts.[25] The use of a computer controlled moving collector allows for the accurate deposition of nano- to micron-sized fiber diameters.[6] By moving the collector at speeds matching the jet extrusion speed, the molten polymer can form straight lines in precise patterns that solidify upon polymer cooling. These precisely deposited fibers can be consistently laid on top of each other to reproducibly build personalized scaffolds,[17,25] but require careful optimization between key material- and instrument-based parameters.[27]

Material-based parameters include the molecular weight of the molten polymer, viscosity, and electrical conductivity. Meanwhile, instrument-factors encompass the applied electric voltage, speed of the moving collector, spinneret diameter, distance from the spinneret to the collector, and extrusion pressure.[6,27] From a material viewpoint highly viscous and low conductivity polymers are considered more stable against sideway paths of polymer jet. Under typical conditions, once the balance between temperature and polymer viscosity has been established, adjusting the aforesaid instrument parameters is key to produce defect-free structures. For instance, increasing pressure increases mass flow; however, high pressure and flow rates for low-viscosity solutions would make it difficult to precisely generate micron scale and highly complex arrangements.[28]

The electrohydrodynamic phenomenon stabilization and continuous flow of polymer melt can be achieved by adjusting the applied voltage and extrusion pressure for direct-writing on the substrate.[29] Insufficient electrical force, the main fiber pulling force,

leads to the formation of long beads that randomly buckle and largely impair homogeneous fiber deposition, usually defined as pulsing behavior.[17,30] Conversely, higher electrical forces impact on continuous polymer flow and the presence of remnant charges trapped in the polymer fibers, which affects predominantly fiber stacking.[29,31] Moreover, the speed and translating directions while collecting the polymer jet influence the deposition accuracy.[27] Importantly, to precisely print a highly-ordered scaffold, the collector speed must equal the rate of polymer mass flow, *i.e.*, a parameter known by critical translation speed (CTS), where the shape of the direct-written fiber changes from sinusoidal to a linear morphology.[25,29,30] In detail, increasing the speed of the collector above the CTS allows the polymer stretching and subsequently shapes the jet into a more pronounced catenary profile allowing the formation of thinner fibers.[29,31] In sum, balancing the above-mentioned parameters is essential to achieving well-organized fiber scaffolds. The next topic conveys critical information related to design criteria and how they influence the final characteristics of MEW scaffolds.

2.3 Designing MEW Scaffolds

It is well-established that the “ideal tissue-specific” scaffold should support suitable biological response via cell-scaffold interaction, amongst other parameters such as mechanical and structural support. That interaction is strongly influenced by fiber diameter and overall scaffold layout pattern.[32–34] Below, we discuss key aspects that influence the design of MEW scaffolds, their role in supporting better regenerative outcomes, as well as ongoing efforts of translating the fabrication of MEW scaffolds from design to more anatomically relevant, non-flat surfaces, as only a few DOC tissues are completely flat.

2.3.1 Fiber diameter

Generally, the diameter of MEW fibers tends to be one order of magnitude bigger than those obtained by solution-based electrospinning. Nonetheless, the submicron-to-micron scale diameter allows for production of highly-ordered and porous scaffolds.[25,31] Numerous studies have investigated the effect of MEW parameters (*e.g.*, melting temperature, applied voltage, pressure, collector speed, nozzle diameter, etc.) on the resulting fiber diameter and several groups have systematically explored variable MEW parameters in regards to that **(Table 1)**. In brief, controlling both polymer dispensing pressure and collector speed permits to create a full spectrum of fiber diameters.[31] Thinner fibers (~ 3-30 μm) are formed when the collector speed surpasses the CTS and mechanical stretching of the molten jet.[28,29] In contrast, fiber thickening from 2 μm to 7 μm occurs as a result of high flow rate, *i.e.*, increasing polymer dispensing pressure from 0.5 to 4 bar.[31] In fact, the flow rate of polymer melt appears to be a key factor governing fiber diameter.[35] Nevertheless, these aspects are valid, without any variations, for the applied voltage since higher voltages tend to decrease fiber diameter. Thus, adjusting these parameters leads to fibers with well-defined diameters in a scale that more closely mimics the collagen fibers in the ECM.[16] As elegantly described in a recent review, controlling the electrified jet has prevented the fiber pulsing effect that results in predictability and reproducibility of fiber deposition.[17] Moreover, Hrynevich *et al.* created a full spectrum of different fiber diameter in the range of (2–50 μm) using a single nozzle by alternating both pressure and collector speed.[31] Although reducing the fiber diameter of MEW is still challenging, the fiber diameter of melt electrowritten PCL constructs was successfully and significantly reduced through the insertion of an acupuncture needle into

the nozzle.[22] That insightful adaptation reduced the lumen of the end edge and produced fibers with diameters of approximately 300 nm,[22] which might be extrapolated and used while processing nanoscale MEW patterns to DOC applications. Hence, through MEW, in a single fabrication step, a multilayer construct valid for a tissue specific application can be fabricated.[17,31] That is extremely relevant for the regeneration of complex defects involving multiple tissues and tissue-interfaces of hierarchically organized DOC tissues, such as bone, periodontal ligament (PDL) and the temporomandibular joint (TMJ).

2.3.2 Strand spacing and laydown pattern

Scaffold pore size and interconnectivity have been acknowledged as two of the most prominent design parameters dictating cellular response and function **(Fig. 3A-C)**.[6,32] In MEW, strand spacing is greatly influenced by the laydown angle and significantly impacts the mechanical performance of the scaffolds. In brief, as the spacing increases from 0.5 mm^2 to 1 mm^2 the axial stiffness drops as high as 48%, indicating that smaller strand spacing provides adequate compacted structures to preserve mechanical strength. In contrast, increasing the space allows a 20% higher yield strain to make the scaffolds recoverable after deformation.[36] Moreover, from a biological viewpoint, producing scaffolds with varying strand/fiber spacing from 100 µm to 750 µm allows for suitable cellular attachment and growth, leading to improved cell bridging and proliferation.[32,37] While larger spacing impacts cell survival, smaller spacing better supports cell viability and growth behavior.[32,37–39] The effect of strand/fiber spacing and shape is also evident in directing cell-cell interaction and phenotype commitment.[40] Therefore, it is possible to guide cell behavior by controlling strand/fiber spacing to direct progenitor cells attachment, proliferation, and lineage commitment.

In the last few years, apart from highly-order and box-shaped scaffolds, MEW has proven its ability to imitate structures with more complex geometries.[20,41,42] For instance, cardiac tissue holds a unique structural organization and mechanical environment known to guide cell orientation and commitment. Accordingly, MEW was utilized to obtain organized fibers capable of improving cellular response to mechanical anisotropy and guide the alignment of cardiac progenitor cells.[20] Moreover, in a serpentine-shaped layout, the semi-circular fibers straighten their shape, allowing for higher extensions under uniaxial tensile load, and mimicking the viscoelastic nature of heart valves.[43] The pre-programmed MEW serpentine structures have the potential to mimic the wavy nature and viscoelastic properties of collagen fibers of heart valves, and exhibited mechanical strength similar to conventional materials used in aortic grafts **(Fig. 4A-B)**.[43] Remarkably, sinusoidal MEW patterns displayed non-linear stress-strain behavior and low stress at initial strain under uniaxial tensile loading, thus approximating to the non-linear behavior of crimped collagen fibrils present in tendons and ligaments.[44] These findings emphasize the ability of MEW to produce tissue-specific scaffolds/constructs that replicate the arrangement and mimic the biomechanics of the tissue to be regenerated. Thus, the crimped nature and the micro-anatomical organization of collagen bundles within the periodontal ligament (PDL) can be captured via applying MEW principle. These concepts can also be extrapolated to mimic native temporomandibular ligaments functions on controlling physiological mandibular movements and the stability of the disc.

2.3.3 Voluminous constructs

For the fabrication of voluminous constructs, typically above 2-mm thick, accurate fiber stacking has been considered an issue due to remnant electrical charges trapped in already deposited fibers, and the “jet lag” phenomenon, where the electrified molten jet is deposited on the collector at a discrete distance behind the position of the nozzle.[25] That slight difference is more evident as the number of layers increase, which in turn affects the accuracy of the construct.[25] Indeed, the fabrication of scaffolds mimics not only the structural complexity of a given tissue but also resembles its size, which is one of the end goals for tissue regeneration. Strikingly, Saidy *et al.* have successfully replicated the complex geometries of real size aortic root and sinus of Valsalva using a two-component collector to minimize electric field instabilities and improve control on the fibers’ deposition **(Fig. 4C)**.[45] It is also noteworthy that MEW has been employed to obtain degradable medical devices for cardiac treatments. For instance, coronary stents of PCL and reduced graphene oxide (PCL-rGO) were combined to prepare stents in various diameters and architectures via MEW **(Fig. 4D)**. The constructs demonstrated ability of being crimped and re-expanded to enable catheter deployment, and improved endothelialization.[46] These findings contribute to design patient-specific scaffolds and move towards on translating the technology to the clinical realm.[46] Meanwhile, the physical principles correspondent to limited volume of MEW constructs have been studied.[30] Variable working distances were established via computational modeling system to maintain constant electrostatic forces during printing. The established computational simulation allows for the production of highly-ordered large volume construct of maximum height ~ 7 mm by alternating voltage profiles. Nonetheless, the control over the microscale layer shifting has permitted the creation of tilted walls in a construct. Outstandingly,

modifications in the amplitude (*i.e.*, a layer-on-layer shift in the range of the printing paths), inward, and outward tilts, were controlled to foster the overhanging design **(Fig. 5A)**.[23] This strategy opens new horizons on designing nature-inspired scaffolds for applications in regenerative medicine and dentistry in particular, where supportive interfacial layer is needed between structurally and mechanically dissimilar soft and hard tissues, such as cementum-PDL or PDL-bone. Moreover, it opens new possibilities to replicate the circular shape of osteons in native cortical bone.

Until now, a few regenerative principles have been applied to dentistry, considering the complex anatomy of tooth structures, mineralized enamel, dentin and soft-core dental pulp and the surrounded periodontium. To build such structure a high-resolution volumetric complex to support the diversity in each layer is needed. Conceptually, Liashenko *et al.* have created layer-by-layer deposition of polymer melt with a higher level of accuracy not only to produce 3D constructs but to fabricate an ultrafast high resolution self-assembly constructs using the advantage of EHD jet deflection printing **(Fig. 5B)**.[47] This strategy might unlock some of the current limitations of MEW, *i.e.*, fabrication of large volumes and decrease fabrication time. These contributions would be pivotal to direct the path of building tissue-specific constructs to regenerate a variety of DOC tissues affected by trauma, disease, or congenital anomalies.

2.3.4 From flat to anatomically relevant substrates

To date, the majority of MEW research has focused on a “in-plane” printing approach, where structures are manufactured in the same plane as the substrate/build plate. In almost all cases this means that structures are deposited onto a flat substrate. In addition, to ensure a constant electrostatic force, which is responsible for pulling the

fibers in MEW, the substrate/build plate is typically composed of conductive metallic materials, such as copper, stainless steel, or aluminium. Obviously, these inherent requirements do not represent the resorbable biomaterials and natural anatomical structures that tissue engineering and regenerative dental medicine aims to recreate.[48] Recent reports have shown that MEW can also accurately print microstructured fiber meshes into anatomically relevant shapes **(Fig. 4 and Fig. 5)**, such as convex-shaped structures, and onto clinically relevant biomaterials, including hydrogel, bioceramics and thermoplastics. These findings have been applied to the fabrication of anatomically-shaped MEW scaffolds that can follow the contour of a diarthrodial joint surface, which could also be wisely applied to osteochondral interfaces of the temporomandibular joint (TMJ).

In a few other recent studies researchers have included a 4th rotary axis beneath the deposition printhead to produce structures of increasing complexity on cylindrical mandrels. McColl *et al.*, developed an advanced tool of web-based mathematical application for planning continuous direct-writing path complex tubular frame of diameter as small as 1.5 mm **(Fig. 5C)**.[18] Equally innovative, MEW was effectively leveraged to devise tubular scaffolds replicating kidney tubules.[19] Rhombus-shaped constructs mimicking kidney's proximal tubules were engineered to facilitate exchanges with vasculature and improve the filtration process.[19] The ability to develop tubular structures has tremendous clinical value not only for engineering vascular structures but also for salivary glands tubules regeneration after tumor resection. Apart from that, DOC region structures such as TMJ and periodontal tissues are under continuous loading which is critical for material design. A material with negative Poisson's ratio *e.g.*, auxetic materials

that expand rather than contract upon loading may support blood vessels against collapse and allow regeneration.[49] Recently, Paxton *et al.* represented auxetic tubular scaffold fabricated via MEW. Upon loading, the material showed 80.8% increase in diameter and Poisson's ratio of − 5.8.[49] Collectively, these extraordinary findings emphasize that the design freedom of MEW has translation potential in the development of patient/defect-specific scaffolds for complex functional tissues and thus hold great impact in DOC tissue regeneration.

2.4 Convergence of materials and technologies for hierarchical complex structures fabrication

A hierarchically structured construct composed of interconnected pores offers significant increase in overall mechanical properties to provide both haptotaptic and mechanotransducive environment for cells to establish the regenerative process.

Hydrogels are an important class of biomaterials that contain significant amounts of water, and which have numerous applications in regenerative dental medicine. Classically, hydrogels provide a 3D microenvironment for cells comparable to the ECM of native tissues. Although hydrogels have been used to support extensive cellular differentiation, they are intrinsically soft and lack the mechanical competence needed for load-bearing applications.[50,51] Therefore, hydrogel reinforcement using well-organized, low volume fraction polymeric meshes obtained by MEW offers an opportunity to mimic both the mechanical and biological microenvironments of native tissues, such as articular cartilage,[50] periodontium, and TMJ. The customizable network composites of hybrid hydrogels and MEW meshes, emulating a fluid-saturated environment and organic stretchable curvy structures, were successfully obtained to resemble collagen fiber

architectures of cartilaginous tissues **(Fig. 6A)**.[52] Worth noting, the mechanism of reinforcement with the soft hydrogel combined with MEW fibers when loaded in compression is based on the tensioning of the thin polymeric fibers upon lateral displacement of the regenerative hydrogel component. Additionally, multiscale and Finite Element (FE) modeling revealed that the fiber interconnections further contribute to this significant load carrying-ability of the hybrid structures.[53] The large magnitude of reinforcement (>50x) at low fiber fraction is especially exciting as the design possibilities of the organized support structures are extensive and still remain to be fully explored, particularly for the reconstruction of DOC tissues.

Remarkably, the capacity of MEW/Hydrogel-based constructs as biomimetic approaches can be further maximized via incorporation of therapeutic drugs and/or bioactive molecules in dental pulp and periodontal tissue regeneration. For example, we recently reported on the use of MEW PCL fibrous meshes to tune the mechanical properties of bioactive amorphous magnesium phosphate (AMP)-modified gelatin methacryloyl (GelMA) hydrogel for bone regeneration **(Fig. 6B)**.[6] Besides, the mechanical reinforcement, the presence of AMP at 5% favored high mineralization and stimulated *in vivo* bone formation.[6] Furthermore, additional design modifications such as the combination of “out-of-plane” MEW constructs, specifically intended to stabilize an existing structure, has shown to enhance the shear modulus of the composite, regardless of gel percentage and crosslinking density **(Fig. 5D)**.[54]

Although the use of polymeric MEW fibers to strengthen hydrogels showed promising results when exposed to compressive forces, the interplay of compressive, shear, and tensile stresses that human tissues are subjected to is not yet fully addressed,

particularly in functional tissues such as those in the DOC complex. Despite the encouraging outcomes, the integration of MEW structures into a hydrogel is typically a two-step process, where the construct is fabricated first then embedded within a cell-free or cell-laden hydrogel. The aforementioned approach limits the freedom of design of the microfiber architectures, as well as the use of multiple materials and cell types observed in DOC region. In this way, for the reconstruction of tissue interfaces as well as highly-organized tissues, a single biofabrication platform is desirable. Thus, using the convergence of 3D printing and bioprinting technologies enables fabrication of scaffold systems with improved spatial control over cell positioning and biomolecules distribution.[10,55] In order to mimic tissue-specificity and multi-tissue interfaces, multiphasic constructs have been realized by converging MEW with other 3D (bio)printing technologies, as well as distinct materials. Even though biphasic scaffolds using FDM and MEW,[56] MEW and CaP-coated FDM constructs **(Fig. 7A)**,[57,58] or the combination between electrospinning and MEW[59] for hard and soft tissue compartments in bone and ligaments have demonstrated improved interconnectivity and regenerative capacity, their multiphasic architectures are mostly achieved by merging techniques and materials in post-fabrication steps. Briefly, multiple techniques are not used simultaneously while printing multiphasic scaffolds, but every compartment is printed individually and merged or combined by superposition after the previous phase is finished. By contrast, in MEW, multiphasic scaffolds can be obtained in a single-step by alternating parameters such as laydown patterns, collector speed, and extrusion pressure, thus facilitating multi-tissue and tissue-specific scaffold fabrication.[31,60] Notably, a clinically promising strategy ingeniously converged MEW and bioceramic printing to engineer hard-to-soft tissue

interfaces **(Fig. 7B)**.[61] Likewise, the fabrication of polymeric scaffolds via MEW with a heterogenous gradient of strands spacing led to improved bone formation *in vivo* **(Fig. 7C)**.[62]

Bi-layered microfibrous architecture MEW scaffolds, that combine a densely distributed crossed fibrous mat (superficial tangential zone, STZ) and a uniform box structure (middle and deep zone, MDZ), were able to capture the native functional properties of both the STZ and MDZ zones of native cartilage.[60] Importantly, the incorporation of a viable STZ reinforcing layer improved the load-bearing properties of bioengineered constructs, particularly when incongruent surfaces are compressed. Moreover, to validate the design approaches in a non-empirical way, a numerical-based approach has been developed for patient-specific soft network composites.[63] The *in silico* design library facilitates materials selection with appropriate architecture to adopt the zonal variation in tissue interface comparable to native tissues. The systematic evaluation of design parameters and their relation to the mechanical properties provides critical insights to fabricate multiphasic constructs. This is particularly important for managing coordinated regeneration events of soft and hard tissues, and their interfaces (*e.g.,* bone-PDL and TMJ). Noteworthy, DOC tissues comprise architecturally complex structures, hence engineering those structures requires tissue-specific approaches, provide cellular instructive cues at spatial and temporal levels. In this sense, a single platform of convergence 3D (bio)printing technologies yield resolution and spatial control for optimal cell distribution and improved biomechanics. A higher level of reinforced forms of hydrogel/MEW constructs by alternated printing of both hydrogel and MEW has been established.[38,165] In a forward-looking study, Ruijter *et al.* described the convergence

between bioprinting and MEW in a single biofabrication platform, which allowed the assembly of mechanically stable constructs with spatial distribution of different cell types without compromising cell viability and differentiation of mesenchymal stromal cells (MSCs) **(Fig. 8A)**.[64] Moreover, both hard-to-soft tissue interfaces can be strongly integrated via convergence of spatial cell printing and mechanical reinforcing fiber constructs obtained by MEW.

The convergence of complementary biofabrication tools (*e.g.*, 3D (bio)printing and MEW) has the potential to yield scaffold systems that would control the dynamics of cell commitment in compartmentalized tissues and interfaces transition. This would possibly represent creating constructs able to recognize and adapt to the continuous changes of the microenvironment and support tissue growth. Conspicuously, Constante *et al.*, reported novel shape morphing anisotropic patterns using 4D printing, based on programmed deposition of MEW fibers and extrusion printing of methacrylated alginate hydrogel that supported the alignment of myofibroblasts to a high degree **(Fig. 8B)**.[65] Recently, Castilho *et al.*, described the concept of cell electrowriting (CEW) to print highly-ordered cell-laden hydrogel-based bioinks through a modified MEW device at room temperature **(Fig. 8C)**.[24] In detail, by engineering two photo-responsive hydrogel bioinks based on protein-based polymers with different gelation chemistry (gelatin and silk fibroin), that are compatible with electrodeposition principles, the authors[24] demonstrated the fabrication of 3D ordered cell-laden constructs (squares, hexagons, and curved patterns) with reduced fiber sizes (5 to 40 μm) that supported and maintained high cell viability post-printing.

In aggregate, the integration of fiber technologies with extrusion or electrohydrodynamic based bioprinting enhances control over spatial and local distribution of different cell types and improved mechanical competence of bioprinted constructs, while simultaneously expanding manufacturing capabilities to better reproduce local composition of cellular microenvironments.

2.5 Application of MEW scaffolds

Despite the striking advances and latest understanding of the impact of MEW in regenerative therapies, the translation of engineering-driven concepts to the clinics relies on a series of biological factors. Next, we discuss how MEW scaffolds interact with different cell types and biomolecules for tissue regeneration.

2.5.1 MEW scaffolds and cell behavior

Many studies have demonstrated that MEW scaffolds can resemble unique features of the native ECM and regulate a high level of cellular events.[21,32,66] The cell behavior, in terms of morphology and molecular signaling, is affected by scaffold topography, strands spacing, and scaffold laydown patterns.

Cellular orientation is of particular concern in tissues that have a high level of cell alignment. The highly hierarchical organization, of orthopedic and periodontal ligament tissues conveys elasticity and high tensile strength crucial for bearing the physiological cyclic loading during function. The utilization of a highly organized MEW fibers, for instance, induced spontaneous cell alignment.[36] Aligned fibers were able to orient human mesenchymal stem cells (hMSCs) toward the fiber's direction where that alignment was lost in cells cultured on the other pattern.[67] Likewise, Paxton *et al*. have explored the effect

of the laydown angles on cellular behavior; scaffolds with laydown angles of 20° and 50° exhibited more uncontrolled cell bridging after 21 days compared to 90°.[36] A laydown of 90° also results in cells branching around the corners of each strand and higher YAP expression, whereas less branching was evident at 45°.[68] Moreover, shape-driven pathway is evident to direct cell phenotype commitment by modifying the biophysical characteristics of biomaterial substrates, *e.g.*, small strands spacing may tune construct stiffness and subsequently direct stem cell commitment.[40] The strand spacing of 100 μm increased toughness and yield forces up to 2.8-fold greater than (200 and 300 μm), correlated to higher nuclear YAP expression and osteogenic commitment for potential applications in hard tissue regeneration.[68] Furthermore, heterogenous gradient spacings, improve cell entrapment for an efficient cell scaffold-based therapy for osseous tissue regeneration in the presence of bioactive molecules (*e.g.*, CaP coating).[21] Of note, one of the major challenges in the production of biomaterials and the design of three-dimensional (3D) scaffolds remains to guide the innate immune response after implantation. A key player in the innate immune system in response to inflammatory conditions and overall inflammatory response at the site of biomaterial implantation is the conversion of pro-inflammatory (M1) to the anti-inflammatory, pro-healing (M2) type macrophages. A geometry-controlled biomaterial that precisely drives macrophage polarization has great clinical potential. For this purpose, Tylek *et al.* fabricated a box-shaped MEW scaffold of 100 μm down to 40 μm inter-fiber spacing. The 40 μm spacing supports human macrophage elongation and spontaneous differentiation as well us upregulation of M2 markers (CD163, CD206, and IL-10) **(Fig. 9A)**.[33] Generally, the design of biomaterials could amplify tissue regeneration via macrophage polarization to enhance

inflammation resolution and promote tissue healing, particularly in a pathogen-driven disorder such as periodontitis (gum disease). Thus, biomaterial-informed constructs are complementary, if not a potential substitute for currently employed biomolecules to direct the response of progenitor cells to promote tissue healing and subsequently regeneration in the DOC complex.

2.5.2 MEW scaffolds as 3D microenvironments to study and regenerate tissues

Because of the continuous growth of elderly population, and the need for treating dental, oral, and craniomaxillofacial defects caused by trauma, diseases and resections, it is vital to develop platforms to better understand physiological and pathologic environments to establish more predictable regenerative therapies. For instance, 3D tissue engineered platforms closely mimicking both soft and hard tissue components of oral tissues can offer invaluable *in vitro* models to investigate tissue invasion in head and neck cancer (HNC) and serve as diagnostic and therapeutic tools. HNC such as squamous cell carcinoma (SCC) deliberated one of the poor prognosis malignities that impact overall quality of patient life, therefore the establishment of true 3D *in vitro* models to help bridge the gap of available 2D culture models is central to recapitulating the complexity of HNC microenvironment.

To study cases of cancer progression and bone destruction caused by metastasis, there is a need to better mimic the complexity of tumor microenvironments. Hence, Bock (2019) reported on a platform to facilitate studying the biological processes of cancer progression in the bone compartment in a physiological context comparable to native tissue utilizing MEW technology and a co-culture system of human pre-osteoblast (hPOB) and prostate cancer cells. The 3D bone microenvironment was conferred by CaP

coating of MEW scaffold to elucidate the nature of interactions between cancer cells and osteoblasts, and the biological effects of lack of androgen on cancer progression in bone.[69] The proposed artificial metastatic tissue model holds promising for investigating cell–cell and cell–matrix interactions between bone and cancer cells in an actual 3D microenvironment.[69]

Likewise, 3D *in vitro* models that resemble the endosteal microenvironment would allow to study treatment modalities of blood and immune-related diseases. Cascante *et al.* established a physiologically relevant 3D microenvironment utilizing MEW to sustain the suitability of placenta-derived mesenchymal stem cells (plMSCs) co-cultured with primary human osteoblasts (hOBs). The endosteal bone-like microenvironment supports the proliferation and migration of primary human hematopoietic stem cells (HSCs) when compared to 2D environment.[70] Another example, a MEW radial construct filled with Matrigel® was conceptualized to investigate glioblastoma cell migration, as a result of matrix concentration and the topographical cues of MEW fibers **(Fig. 9B)**.[71] The reinforced Matrigel with MEW mesh allows the characterization of glycine receptor-transfected cells electrophysiologically in 3D.[42]

The design of MEW constructs provides retention and enabled long-term structural integrity to improve differentiation of stem cells (*e.g.*, adipose derived stromal cell). McMaster *et al*. cultured multicellular spheroids in a 360 µm box-shaped scaffold supported only with two single catching fibers **(Fig. 9C).** Apart from the efficacy of the proposed scaffold in adipose engineering, utilizing the tailorable MEW scaffold for the seeding of multicellular spheroids may be readily transferred to engineering cartilage tissue for which pellet culture is frequently used or pre-seeded endothelial cells prior to

spheroid insertion for vascularized, sheet-like structures.[34] Furthermore, MEW provides ability to scale expansion up for cell-based and immunotherapy. For instance, defined spaces and high surface area of MEW lattice construct allows to recapitulate the dynamic interactions of primary human lymphoid tissues and induction of proliferative signals for T cell expansion.[72] Taken together, a deep understanding of the cell and molecular signatures in health and disease conditions affecting the structures of the DOC complex is key to designing proper scaffolds, as well as 3D *in vitro* platforms to improve therapeutics potential.

2.5.3 Rebuilding vascularization and innervation via MEW

DOC tissues present hierarchically organized vascularization and innervation. Moreover, it is not uncommon to see trauma, or injuries to vessels and nerves due to iatrogenic procedures. In regenerative therapies, the vascularization of engineered constructs enhances cell signaling and avoids core necrosis. However, *in vitro* vascularization of biofabricated tissues is challenging due to vascular network geometry, critical for cell survival, metabolic activity, and differentiation potential. MEW constructs/scaffolds, combined with a cell-accumulation technique, would allow for the formation of controlled capillary-like network structures.[73] The combination of MEW and electrospinning allowed for the formation of a simultaneous layer-specific native vessel, recapitulated the tunica intima and tunica media, and relevant progenitor cell sources for vascular grafts.[74] Moreover, MEW constructs and cell-based therapies have many applications to produce multiple specialized tissues. Tubular MEW constructs provided an orthotopic platform that mimicked the periosteal microenvironment and a cocultured

system of human endothelial and bone marrow mesenchymal stem cells (BM-MSCs) resembled both the vascular and osteogenic niche of native bone.[75]

Likewise, 3D printed neural regeneration strategies have also emerged as new therapeutic approaches for neural diseases and injuries. For instance, the development of cortical neurons in fiber-reinforced matrices demonstrated to be possible to mimic the native embryonic brain environment, thus laying the groundwork for studying the neuronal cells network in a 3D environment under normal and pathophysiological conditions.[76] From a dental perspective, further insights in the field would favor the development of strategies to recover micro-innervation and proprioception of the dental pulp after necrosis, and the regeneration of damaged nerves or chronic paresthesia after trauma, resection, or iatrogenic dental procedures.

2.5.4 MEW-based scaffolds for regeneration of DOC tissues and interfaces

Craniomaxillofacial bones and connective tissues organization are complex in size, confinement, and function, compared to other regions in the human body. Strategies to regenerate dentin microtubular structure lost by caries, or the intimate interaction among disc, ligaments, and craniomandibular bones in the TMJ remain elusive. Nonetheless, as previously mentioned in this review, the freedom of design, printability and resolution of MEW scaffolds can guide future strategies for tooth and TMJ regeneration.

A biphasic construct was fabricated to replicate bone-ligament-bone (BLB) interfaces simulating the native anterior cruciate ligament organization.[67] The specific geometries of the construct influence cell orientation and growth, while the mechanical performance at the interface is a key feature to improve tensile properties. These

approaches can further direct BLB interfaces regeneration in craniomaxillofacial region.[67] Moreover, current insights on MEW and hydrogels combination may lead to the fabrication of specific constructs mimicking the structure, and native mechanical and biological behavior of the TMJ. Functionalized hydrogels deliver bioactive molecules such as bone morphogenetic protein 2 (BMP2) combined with biphasic FDM and MEW scaffolds replicating both cancellous and cortical bone.[57] Alternatively, hard-to-soft tissue interfaces reconstruction, through MEW and hydrogels combination, emulates viscoelasticity and stress relaxation behavior of cartilage and ligaments, in response to mechanical loading.[50,52] Nonetheless, the highest complexity in DOC tissues is probably in the periodontium (*i.e.*, gingiva, cementum, periodontal ligament, and alveolar bone), working as a single complex system with supportive, protective, and proprioceptive functions.[3] To date, the management of periodontal tissue destruction has encompassed scaling and root planing, flap surgery, biologics (*e.g.*, enamel matrix derivative), bone grafting, and guided tissue regeneration by means of a degradable membrane that, while serving as a barrier against soft tissue infiltration, allows resident progenitor cells to promote the regeneration of periodontal tissues. Although existing therapeutics can lead to some degree of tissue regeneration, the low predictability and efficacy in cases of extreme tissue destruction call for improved strategies that can better replicate the three-dimensional (3D) and multi-tissue complexity of periodontal defects. Precisely, there are currently no approaches to predictably regenerate defects with considerable bone loss and avoid tooth extraction. Thus, there is an emerging quest for personalized (tissue- and defect-specific) solutions that can guide the coordinated growth and development of the periodontal attachment apparatus to prolong the lifetime of the patient's natural dentition.

Currently, there is no clinically available technology that offers the opportunity to create personalized scaffolds to predictably address regeneration of the periodontal attachment apparatus on root surfaces with severe bone loss. It is, therefore, well understood that highly complex defects impair the quality and amount of vascular and cellular elements, and, by consequence, are less favorable for the success of a regenerative strategy.[77] Due to its versatility and the possibility of incorporating bioactive molecules and drugs, while preserving the mechanical properties and degradability, conventional electrospinning has extensively fostered the development of guided tissue/bone regeneration (GTR/GBR) membrane-driven approach for DOC tissues. However, conventional electrospinning does not allow the development of specific designs to regenerate site-specific defects.[5,78] In this sense, mimicking the complexity of the periodontal individual compartments and interconnectivity stands as the most critical issue regarding scaffold-based periodontal regeneration.

Fortunately, the advent of 3D (bio)printed regenerative approaches has provided new treatment perspectives and MEW has arisen as a unique technology to generate scaffolds/constructs mimicking highly-complex and organized structures that can be translated to study and regenerate bone and cartilage in the craniofacial region. MEW allows the synthesis of multiphasic, site-specific or non-flat anatomically relevant designs that can be applied for different tissues and interfaces **(Fig. 10)**.[48] These concepts have been initially translated for periodontal regeneration, where a multilayer membrane, fabricated by MEW, provided an optimal substrate for tissue growth at the same time acted as a barrier against soft-tissue cells invagination, and displayed bacteria-tightness.[39] Moreover, combining MEW with other techniques address structural

compartmentalization of both hard and soft tissues.[59] For example, converging MEW and traditional electrospinning, with bone marrow-derived mesenchymal stem cells (BMMSCs) and periodontal ligament stem cells (PDLSCs) cell sheets, fostered bone and periodontal ligament regeneration.[59] Additionally, biphasic membranes combining FDM-CaP, for bone compartment, and MEW for PDL compartment, showed improved interconnectivity between the bone and periodontal ligament compartments in *in vivo* subcutaneously implanted dentin slice's model.[56] To that end, the advantages associated with MEW and the opportunities to integrating this promising AM tool with well-established 3D (bio)printing technologies represent a clear path to the translation of scaffolds that replicate not only the micron-scale, but also the complex 3D geometries of periodontal defects.

2.6 Conclusions and future perspectives

Recapitulating hierarchical organization, along with the biological and mechanical behavior of hard and soft tissues and interfaces, is the ultimate goal of tissue regeneration. To date, a plethora of AM technologies have been used to synthesize scaffolds for application in regenerative medicine and dentistry, and this review focused on the emergence of MEW as a relevant strategy to build constructs with freedom of design and accuracy, while recapitulating native tissues' arrangement. In the same way, MEW allows the combination with other AM technologies to fabricate hybrid scaffolds that address tissue complexity, biological, and physical properties. Although MEW is an outstanding technology that aids in replicating the nature, size, and organization of tissues, the full possibilities of this fairly novel approach in the biofabrication of dental, oral, and craniofacial (DOC) structures continue to be unveiled.

As control over the technology moves forward, it is possible to design scaffolds that address major concerns related to the regeneration of DOC tissues, such as complexity of periodontal defects, mechanical and biological behavior of the TMJ, and permanent damage due to chronic diseases, trauma, and resectioning. By taming all the possibilities discussed in this review, and selecting the proper combination of materials, biomolecules, and cells; MEW provides unique conditions to create highly complex constructs/scaffolds with supportive biophysical properties to reconstruct damaged tissues in the DOC region. Moreover, melt electrowritten scaffolds' ability to recapitulate hard-to-soft tissue transitions fosters the development of site-specific constructs for alveolar bone, temporomandibular joint, tooth, and periodontal regeneration.

The applicability of MEW to precisely fabricate compartmentalized scaffolds, control over an infinite range of geometries, and recently proposed cell electrowriting (CEW) form a strong foundation for future work on cellular microenvironments and immediate cell commitment in multicellular tissue constructs. Furthermore, current studies that use MEW scaffolds for bone and connective tissues' regeneration, and possible integration with vessels and neural functionality, direct the steps towards developing site-specific scaffolds. These aspects are truly valuable when they mimic anatomic and functional tissue-specificity while printing scaffolds that regenerate the dentin-pulp complex and periodontal tissues (*i.e.,* cementum, periodontal ligament, and alveolar bone) with their respective delicate interfaces, while also providing a better understanding of the aspects involved in tumor progression in the oral and craniofacial region.

Lastly, opportunities related to the convergence of MEW with other 3D (bio)printing tools address specific response challenges for multi-tissue regeneration. In this sense,

constant improvements in the printability of high-resolution image-based scaffolds encourage work on micro- and nanoscale complex designs using converged AM technologies. It is expected that these improved scaffolds can hierarchically mimic the ECM of native tissues and have control over the profile that guides future defect-specific, single-step scaffolds for DOC tissues and tissue interfaces, and thus expedite its clinical translation.

Declaration of Competing Interest

The authors declare no competing financial interest or with respect to the authorship and/or publication of this article.

Acknowledgements

The authors are grateful for the images and cartoons designed by Kenneth Rieger (Multimedia Designer, Department, School of Dentistry, University of Michigan, Ann Arbor, MI, USA). Figure 1 was created with BioRender.com. This project was supported by funding from the National Institutes of Health (NIH, National Institute of Dental and Craniofacial Research (K08DE023552 and R01DE026578 to MCB), the Osteology Foundation (Advanced Researcher Award), OsteoScience Foundation (Peter Geistlich Research Award), the International Association for Dental Research (IADR-GSK Innovation in Oral Care Award and IADR-AO Implant Sciences Award), the American Academy of Implant Dentistry Foundation, the European Union H2020 program BRAVE (grant number 874827) and the Gravitation Program “Materials Driven Regeneration” by the Netherlands Organization for Scientific Research (024.003.013).

2.7 References

1. Petrovic, V., Zivkovic, P., Petrovic, D. & Stefanovic, V. Craniofacial bone tissue engineering. *Oral Surgery, Oral Medicine, Oral Pathology and Oral Radiology* **114**, e1–e9 (2012).

2. Dwivedi, R. *et al.* Polycaprolactone as biomaterial for bone scaffolds: Review of literature. *J Oral Biol Craniofac Res* **10**, 381–388 (2020).

3. Bottino, M. C. *et al.* Recent advances in the development of GTR/GBR membranes for periodontal regeneration--a materials perspective. *Dent Mater* **28**, 703–721 (2012).

4. Du, Y., Guo, J. L., Wang, J., Mikos, A. G. & Zhang, S. Hierarchically designed bone scaffolds: From internal cues to external stimuli. *Biomaterials* **218**, 119334 (2019).

5. Daghrery, A. *et al.* Electrospinning of dexamethasone/cyclodextrin inclusion complex polymer fibers for dental pulp therapy. *Colloids and Surfaces B: Biointerfaces* 111011 (2020) doi:10.1016/j.colsurfb.2020.111011.

6. Dubey, N. *et al.* Highly tunable bioactive fiber-reinforced hydrogel for guided bone regeneration. *Acta Biomaterialia* (2020) doi:10.1016/j.actbio.2020.06.011.

7. Hochleitner, G. *et al.* Additive manufacturing of scaffolds with sub-micron filaments via melt electrospinning writing. *Biofabrication* **7**, 035002 (2015).

8. Zhiwei, J. *et al.* 3D printing of HA / PCL composite tissue engineering scaffolds. *Advanced Industrial and Engineering Polymer Research* **2**, (2019).

9. Bas, O. *et al.* An Integrated Design, Material, and Fabrication Platform for Engineering Biomechanically and Biologically Functional Soft Tissues. *ACS Appl. Mater. Interfaces* **9**, 29430–29437 (2017).

10. Castilho, M. *et al.* Multitechnology Biofabrication: A New Approach for the Manufacturing of Functional Tissue Structures? *Trends in Biotechnology* **38**, 1316–1328 (2020).

11. Ozbolat, I. & Gudapati, H. A review on design for bioprinting. *Bioprinting* **3–4**, 1–14 (2016).

12. Boccaccio, A., Uva, A. E., Fiorentino, M., Lamberti, L. & Monno, G. A Mechanobiology-based Algorithm to Optimize the Microstructure Geometry of Bone Tissue Scaffolds. *Int J Biol Sci* **12**, 1–17 (2016).

13. Castilho, M. *et al.* Fabrication of computationally designed scaffolds by low temperature 3D printing. *Biofabrication* **5**, 035012 (2013).

14. Huang, K.-H., Lin, Y.-H., Shie, M.-Y. & Lin, C.-P. Effects of bone morphogenic protein-2 loaded on the 3D-printed MesoCS scaffolds. *Journal of the Formosan Medical Association* **117**, 879–887 (2018).

15. Hutmacher, D. W. *et al.* Mechanical properties and cell cultural response of polycaprolactone scaffolds designed and fabricated via fused deposition modeling. *Journal of Biomedical Materials Research* **55**, 203–216 (2001).

16. Chen, H. *et al.* Direct Writing Electrospinning of Scaffolds with Multidimensional Fiber Architecture for Hierarchical Tissue Engineering. *ACS Appl Mater Interfaces* **9**, 38187–38200 (2017).

17. Robinson, T. M., Hutmacher, D. W. & Dalton, P. D. The Next Frontier in Melt Electrospinning: Taming the Jet. *Advanced Functional Materials* **29**, 1904664 (2019).

18. McColl, E., Groll, J., Jungst, T. & Dalton, P. D. Design and fabrication of melt electrowritten tubes using intuitive software. *Materials & Design* **155**, 46–58 (2018).

19. Genderen, A. M. van *et al.* Topographic Guidance in Melt-Electrowritten Tubular Scaffolds Enhances Engineered Kidney Tubule Performance. *bioRxiv* 2020.09.16.300004 (2020) doi:10.1101/2020.09.16.300004.

20. Castilho, M. *et al.* Melt Electrospinning Writing of Poly-Hydroxymethylglycolide-co-ε-Caprolactone-Based Scaffolds for Cardiac Tissue Engineering. *Adv Healthc Mater* **6**, (2017).

21. Abbasi, N., Abdal-hay, A., Hamlet, S., Graham, E. & Ivanovski, S. Effects of Gradient and Offset Architectures on the Mechanical and Biological Properties of 3-D Melt Electrowritten (MEW) Scaffolds. *ACS Biomater. Sci. Eng.* **5**, 3448–3461 (2019).

22. Großhaus, C. *et al.* Melt Electrospinning of Nanofibers from Medical-Grade Poly(ε-Caprolactone) with a Modified Nozzle. *Small* **16**, 2003471 (2020).

23. Liashenko, I., Hrynevich, A. & Dalton, P. D. Designing Outside the Box: Unlocking the Geometric Freedom of Melt Electrowriting using Microscale Layer Shifting. *Advanced Materials* **32**, 2001874 (2020).

24. Castilho, M. *et al.* Hydrogel-Based Bioinks for Cell Electrowriting of Well-Organized Living Structures with Micrometer-Scale Resolution. *Biomacromolecules* (2021) doi:10.1021/acs.biomac.0c01577.

25. Brown, T. D., Dalton, P. D. & Hutmacher, D. W. Direct Writing By Way of Melt Electrospinning. *Advanced Materials* **23**, 5651–5657 (2011).

26. Hochleitner, G. *et al.* Melt Electrowriting of Thermoplastic Elastomers. *Macromolecular Rapid Communications* **39**, 1800055 (2018).

27. Muerza-Cascante, M. L., Haylock, D., Hutmacher, D. W. & Dalton, P. D. Melt electrospinning and its technologization in tissue engineering. *Tissue Eng Part B Rev* **21**, 187–202 (2015).

28. Wunner, F. M. *et al.* Printomics: the high-throughput analysis of printing parameters applied to melt electrowriting. *Biofabrication* **11**, 025004 (2019).

29. Wunner, F. *et al.* Melt Electrospinning Writing of Three-dimensional Poly(ε-caprolactone) Scaffolds with Controllable Morphologies for Tissue Engineering Applications. *Journal of Visualized Experiments* **2017**, (2017).

30. Wunner, F. M. *et al.* Melt Electrospinning Writing of Highly Ordered Large Volume Scaffold Architectures. *Advanced Materials* **30**, 1706570 (2018).

31. Hrynevich, A. *et al.* Dimension-Based Design of Melt Electrowritten Scaffolds. *Small* **14**, 1800232 (2018).

32. Abbasi, N., Ivanovski, S., Gulati, K., Love, R. M. & Hamlet, S. Role of offset and gradient architectures of 3-D melt electrowritten scaffold on differentiation and mineralization of osteoblasts. *Biomaterials Research* **24**, 2 (2020).

33. Tylek, T. *et al.* Precisely defined fiber scaffolds with 40 µm porosity induce elongation driven M2-like polarization of human macrophages. *Biofabrication* **12**, 025007 (2020).

34. McMaster, R. *et al.* Tailored Melt Electrowritten Scaffolds for the Generation of Sheet-Like Tissue Constructs from Multicellular Spheroids. *Advanced Healthcare Materials* **8**, 1801326 (2019).

35. Brown, T. D. *et al.* Melt electrospinning of poly(ε-caprolactone) scaffolds: Phenomenological observations associated with collection and direct writing. *Materials Science and Engineering: C* **45**, 698–708 (2014).

36. Paxton, N. C. *et al.* Design tools for patient specific and highly controlled melt electrowritten scaffolds. *Journal of the Mechanical Behavior of Biomedical Materials* **105**, 103695 (2020).

37. Xie, C. *et al.* Structure-induced cell growth by 3D printing of heterogeneous scaffolds with ultrafine fibers. *Materials & Design* **181**, 108092 (2019).

38. Fuchs, A. *et al.* Medical-grade polycaprolactone scaffolds made by melt electrospinning writing for oral bone regeneration – a pilot study in vitro. *BMC Oral Health* **19**, (2019).

39. Fuchs, A. *et al.* A new multilayered membrane for tissue engineering of oral hard- and soft tissue by means of melt electrospinning writing and film casting – An in vitro study. *Journal of Cranio-Maxillofacial Surgery* **47**, 695–703 (2019).

40. Brennan, C. M., Eichholz, K. F. & Hoey, D. A. The effect of pore size within fibrous scaffolds fabricated using melt electrowriting on human bone marrow stem cell osteogenesis. *Biomed. Mater.* **14**, 065016 (2019).

41. Warren, P. B., Davis, Z. G. & Fisher, M. B. Parametric control of fiber morphology and tensile mechanics in scaffolds with high aspect ratio geometry produced via melt electrowriting for musculoskeletal soft tissue engineering. *Journal of the Mechanical Behavior of Biomedical Materials* **99**, 153–160 (2019).

42. Schaefer, N. *et al.* 3D Electrophysiological Measurements on Cells Embedded within Fiber-Reinforced Matrigel. *Adv Healthc Mater* **8**, e1801226 (2019).

43. Saidy, N. T. *et al.* Biologically Inspired Scaffolds for Heart Valve Tissue Engineering via Melt Electrowriting. *Small* **15**, 1900873 (2019).

44. Hochleitner, G. *et al.* Melt electrowriting below the critical translation speed to fabricate crimped elastomer scaffolds with non-linear extension behaviour mimicking that of ligaments and tendons. *Acta Biomaterialia* **72**, 110–120 (2018).

45. Saidy, N. T. *et al.* Melt Electrowriting of Complex 3D Anatomically Relevant Scaffolds. *Front. Bioeng. Biotechnol.* **8**, (2020).

46. Somszor, K. *et al.* Personalized, Mechanically Strong, and Biodegradable Coronary Artery Stents via Melt Electrowriting. *ACS Macro Lett.* 1732–1739 (2020) doi:10.1021/acsmacrolett.0c00644.

47. Liashenko, I., Rosell-Llompart, J. & Cabot, A. Ultrafast 3D printing with submicrometer features using electrostatic jet deflection. *Nature Communications* **11**, 753 (2020).

48. Peiffer, Q. C. *et al.* Melt electrowriting onto anatomically relevant biodegradable substrates: Resurfacing a diarthrodial joint. *Materials & Design* **195**, 109025 (2020).

49. Paxton, N. C., Daley, R., Forrestal, D. P., Allenby, M. C. & Woodruff, M. A. Auxetic tubular scaffolds via melt electrowriting. *Materials & Design* **193**, 108787 (2020).

50. Visser, J. *et al.* Reinforcement of hydrogels using three-dimensionally printed microfibres. *Nature Communications* **6**, 1–10 (2015).

51. Haigh, J. N. *et al.* Hierarchically Structured Porous Poly(2-oxazoline) Hydrogels. *Macromolecular Rapid Communications* **37**, 93–99 (2016).

52. Bas, O. *et al.* Biofabricated soft network composites for cartilage tissue engineering. *Biofabrication* **9**, 025014 (2017).

53. Castilho, M. *et al.* Mechanical behavior of a soft hydrogel reinforced with three-dimensional printed microfibre scaffolds. *Scientific Reports* **8**, 1–10 (2018).

54. Ruijter, M. de *et al.* Out-of-Plane 3D-Printed Microfibers Improve the Shear Properties of Hydrogel Composites. *Small* **14**, 1702773 (2018).

55. Dalton, P. D., Woodfield, T. B. F., Mironov, V. & Groll, J. Advances in Hybrid Fabrication toward Hierarchical Tissue Constructs. *Advanced Science* **7**, 1902953 (2020).

56. Costa, P. F. *et al.* Advanced tissue engineering scaffold design for regeneration of the complex hierarchical periodontal structure. *J. Clin. Periodontol.* **41**, 283–294 (2014).

57. Sudheesh Kumar, P. T., Hashimi, S., Saifzadeh, S., Ivanovski, S. & Vaquette, C. Additively manufactured biphasic construct loaded with BMP-2 for vertical bone regeneration: A pilot study in rabbit. *Mater Sci Eng C Mater Biol Appl* **92**, 554–564 (2018).

58. Vaquette, C., Mitchell, J., Fernandez-Medina, T., Kumar, S. & Ivanovski, S. Resorbable additively manufactured scaffold imparts dimensional stability to extraskeletally regenerated bone. *Biomaterials* **269**, 120671 (2021).

59. Vaquette, C., Saifzadeh, S., Farag, A., Hutmacher, D. W. & Ivanovski, S. Periodontal Tissue Engineering with a Multiphasic Construct and Cell Sheets. *J. Dent. Res.* **98**, 673–681 (2019).

60. Castilho, M., Mouser, V., Chen, M., Malda, J. & Ito, K. Bi-layered micro-fibre reinforced hydrogels for articular cartilage regeneration. *Acta Biomaterialia* **95**, 297–306 (2019).

61. Diloksumpan, P. *et al.* Combining multi-scale 3D printing technologies to engineer reinforced hydrogel-ceramic interfaces. *Biofabrication* **12**, 025014 (2020).

62. Abbasi, N., Lee, R. S. B., Ivanovski, S., Love, R. M. & Hamlet, S. In vivo bone regeneration assessment of offset and gradient melt electrowritten (MEW) PCL scaffolds. *Biomaterials Research* **24**, 17 (2020).

63. Bas, O. *et al.* Rational design and fabrication of multiphasic soft network composites for tissue engineering articular cartilage: A numerical model-based approach. *Chemical Engineering Journal* **340**, 15–23 (2018).

64. Ruijter, M. de, Ribeiro, A., Dokter, I., Castilho, M. & Malda, J. Simultaneous Micropatterning of Fibrous Meshes and Bioinks for the Fabrication of Living Tissue Constructs. *Advanced Healthcare Materials* **8**, 1800418 (2019).

65. Constante, G. *et al.* 4D Biofabrication Using a Combination of 3D Printing and Melt-Electrowriting of Shape-Morphing Polymers. *ACS Appl. Mater. Interfaces* (2021) doi:10.1021/acsami.0c18608.

66. Dubey, N., Ferreira, J. A., Malda, J., Bhaduri, S. B. & Bottino, M. C. Extracellular Matrix/Amorphous Magnesium Phosphate Bioink for 3D Bioprinting of Craniomaxillofacial Bone Tissue. *ACS Appl. Mater. Interfaces* **12**, 23752–23763 (2020).

67. Gwiazda, M., Kumar, S., Świeszkowski, W., Ivanovski, S. & Vaquette, C. The effect of melt electrospun writing fiber orientation onto cellular organization and mechanical properties for application in Anterior Cruciate Ligament tissue engineering. *Journal of the Mechanical Behavior of Biomedical Materials* **104**, 103631 (2020).

68. Eichholz, K. F. & Hoey, D. A. Mediating human stem cell behaviour via defined fibrous architectures by melt electrospinning writing. *Acta Biomaterialia* **75**, 140–151 (2018).

69. Bock, N. Bioengineered Microtissue Models of the Human Bone Metastatic Microenvironment: A Novel In Vitro Theranostics Platform for Cancer Research. *Methods Mol. Biol.* **2054**, 23–57 (2019).

70. Muerza-Cascante, M. L. *et al.* Endosteal-like extracellular matrix expression on melt electrospun written scaffolds. *Acta Biomaterialia* **52**, 145–158 (2017).

71. Bakirci, E. *et al.* Melt Electrowritten In Vitro Radial Device to Study Cell Growth and Migration. *Advanced Biosystems* **4**, 2000077 (2020).

72. Delalat, B. *et al.* 3D printed lattices as an activation and expansion platform for T cell therapy. *Biomaterials* **140**, 58–68 (2017).

73. Bertlein, S. *et al.* Development of Endothelial Cell Networks in 3D Tissues by Combination of Melt Electrospinning Writing with Cell-Accumulation Technology. *Small* **14**, 1701521 (2018).

74. Pennings, I. *et al.* Layer-specific cell differentiation in bi-layered vascular grafts under flow perfusion. *Biofabrication* **12**, 015009 (2019).

75. Baldwin, J. G. *et al.* Periosteum tissue engineering in an orthotopic in vivo platform. *Biomaterials* **121**, 193–204 (2017).

76. Janzen, D. *et al.* Cortical Neurons form a Functional Neuronal Network in a 3D Printed Reinforced Matrix. *Advanced Healthcare Materials* **9**, 1901630 (2020).

77. Reynolds, L. P., Borowicz, P. P., Palmieri, C. & Grazul-Bilska, A. T. Placental Vascular Defects in Compromised Pregnancies: Effects of Assisted Reproductive Technologies and Other Maternal Stressors. in *Advances in Fetal and Neonatal Physiology* (eds. Zhang, L. & Ducsay, C. A.) 193–204 (Springer, 2014). doi:10.1007/978-1-4939-1031-1_17.

78. Rowe, M. J. *et al.* Dimensionally stable and bioactive membrane for guided bone regeneration: An in vitro study. *J Biomed Mater Res B Appl Biomater* **104**, 594–605 (2016).

79. Brown, T. D. *et al.* Design and Fabrication of Tubular Scaffolds via Direct Writing in a Melt Electrospinning Mode. *Biointerphases* **7**, 1–16 (2012).

80. Farrugia, B. L. *et al.* Dermal fibroblast infiltration of poly($\upepsilon$-caprolactone) scaffolds fabricated by melt electrospinning in a direct writing mode. *Biofabrication* **5**, 025001 (2013).

81. Ristovski, N. *et al.* Improved fabrication of melt electrospun tissue engineering scaffolds using direct writing and advanced electric field control. *Biointerphases* **10**, 011006 (2015).

82. Chen, F. *et al.* Additive Manufacturing of a Photo-Cross-Linkable Polymer via Direct Melt Electrospinning Writing for Producing High Strength Structures. *Biomacromolecules* **17**, 208–214 (2016).

83. Haigh, J. N., Dargaville, T. R. & Dalton, P. D. Additive manufacturing with polypropylene microfibers. *Materials Science and Engineering: C* **77**, 883–887 (2017).

84. Chen, Q. *et al.* Direct write micro/nano optical fibers by near-field melt electrospinning. *Optics Letters* **42**, 5106 (2017).

85. Hammerl, A., Diaz Cano, C. E., De-Juan-Pardo, E. M., van Griensven, M. & Poh, P. S. P. A Growth Factor-Free Co-Culture System of Osteoblasts and Peripheral Blood Mononuclear Cells for the Evaluation of the Osteogenesis Potential of Melt-Electrowritten Polycaprolactone Scaffolds. *International Journal of Molecular Sciences* **20**, 1068 (2019).

86. Brückner, T. *et al.* Prefabricated and Self-Setting Cement Laminates. *Materials* **12**, 834 (2019).

87. Bertlein, S. *et al.* Permanent Hydrophilization and Generic Bioactivation of Melt Electrowritten Scaffolds. *Advanced Healthcare Materials* **8**, 1801544 (2019).

88. Paxton, N. C. *et al.* Rheological Characterization of Biomaterials Directs Additive Manufacturing of Strontium-Substituted Bioactive Glass/Polycaprolactone Microfibers. *Macromolecular Rapid Communications* **40**, 1900019 (2019).

89. Tourlomousis, F. *et al.* Machine learning metrology of cell confinement in melt electrowritten three-dimensional biomaterial substrates. *Microsystems & Nanoengineering* **5**, 1–19 (2019).

90. Hewitt, E., Mros, S., McConnell, M., Cabral, J. D. & Ali, A. Melt-electrowriting with novel milk protein/PCL biomaterials for skin regeneration. *Biomed Mater* **14**, 055013 (2019).

91. Janzen, D. *et al.* Cortical Neurons form a Functional Neuronal Network in a 3D Printed Reinforced Matrix. *Advanced Healthcare Materials* **n/a**, 1901630.

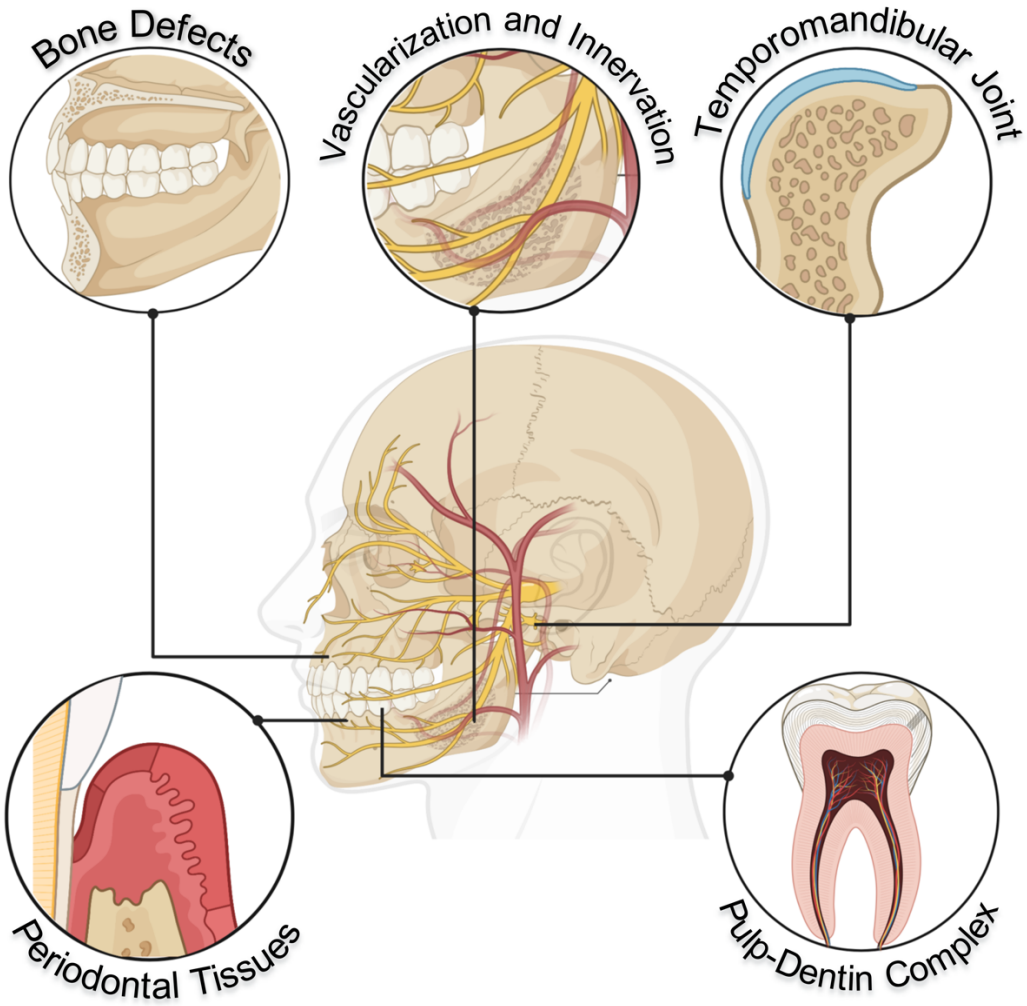

Figure 2-1 Schematic illustration of the anatomy of relevant dental, oral, and craniofacial (DOC) tissues; craniomaxillofacial bone and periodontal complex (alveolar bone, gingiva, periodontal ligament [PDL], and cementum).

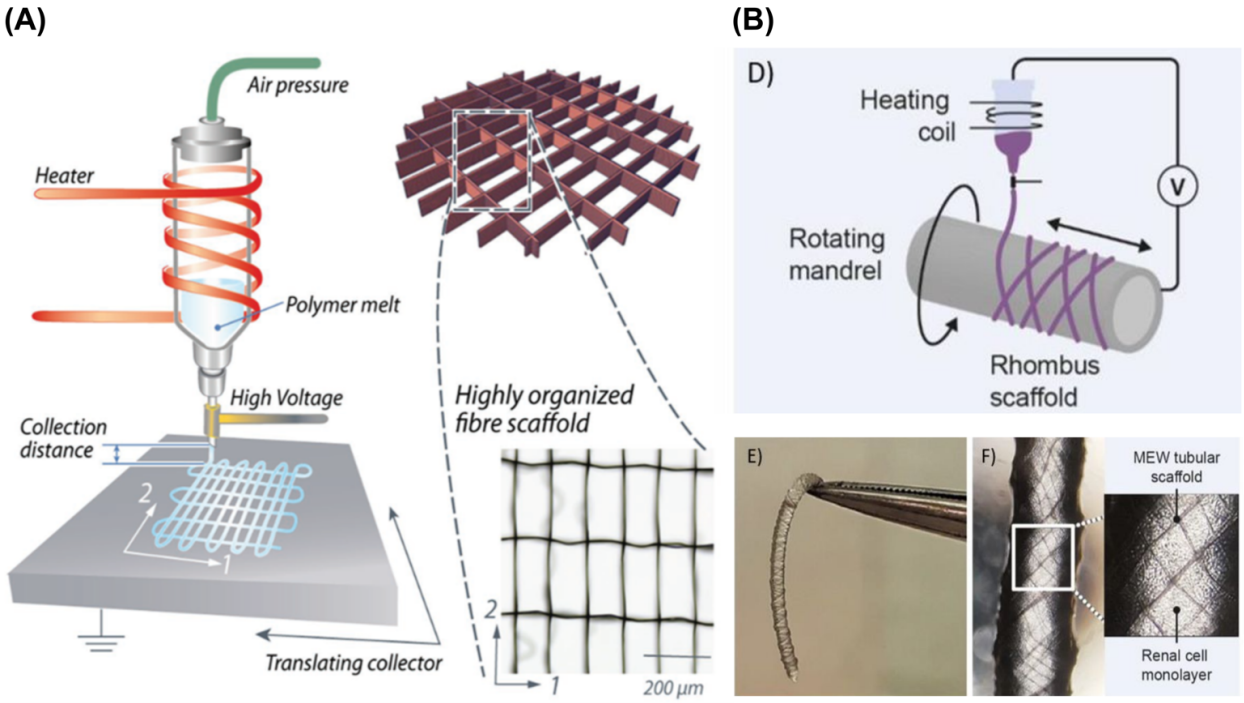

Figure 2-2 MEW devices components of air-pressure-assisted dispensing, electrical heating system, and collector at different configurations
(**A**) Flat-computer-assisted collector. From Castilho et al. (2017). **(B)** MEW fiber deposition over rotating grounded mandrel to form tubular scaffolds. From Genderen et al. (2020)

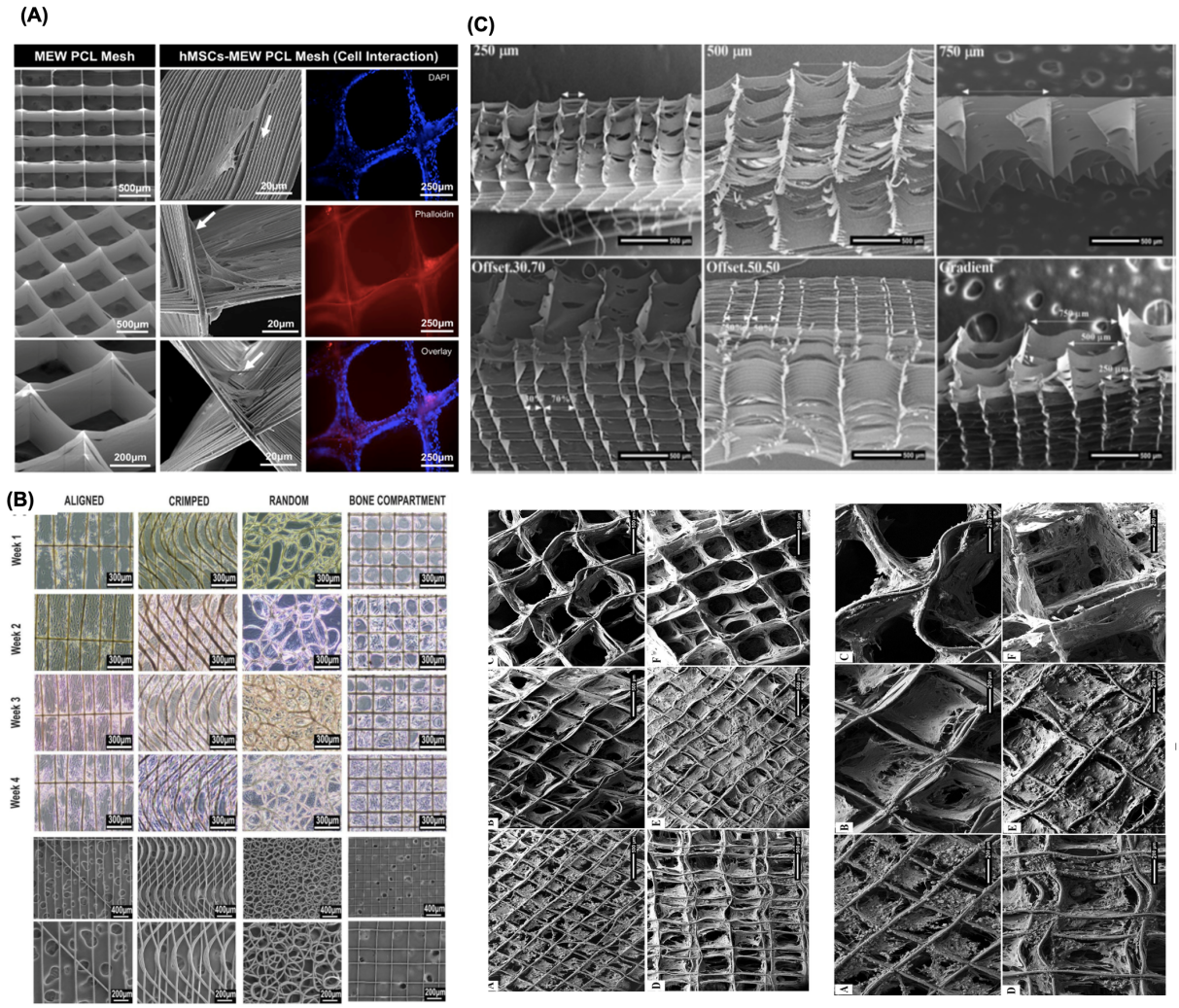

Figure 2-3 Cell's behaviors in various MEW design

(A) Well-aligned (0-90°-oriented junctions) fibrous 3D architecture with 500 µm strand spacing shows human-derived mesenchymal stem cells (hMSCs)/MEW poly(e-caprolactone) scaffold interaction. From Dubey et al. (2020). **(B)** MEW fiber orientation and cellular organization in anterior cruciate ligament tissue engineering. From Gwiazda et al. (2020). **(C)** SEM images of highly-order MEW porous and gradient scaffolds and mineralization of hOB on MEW scaffolds after 30 days of culture. From Abbasi et al. (2020)

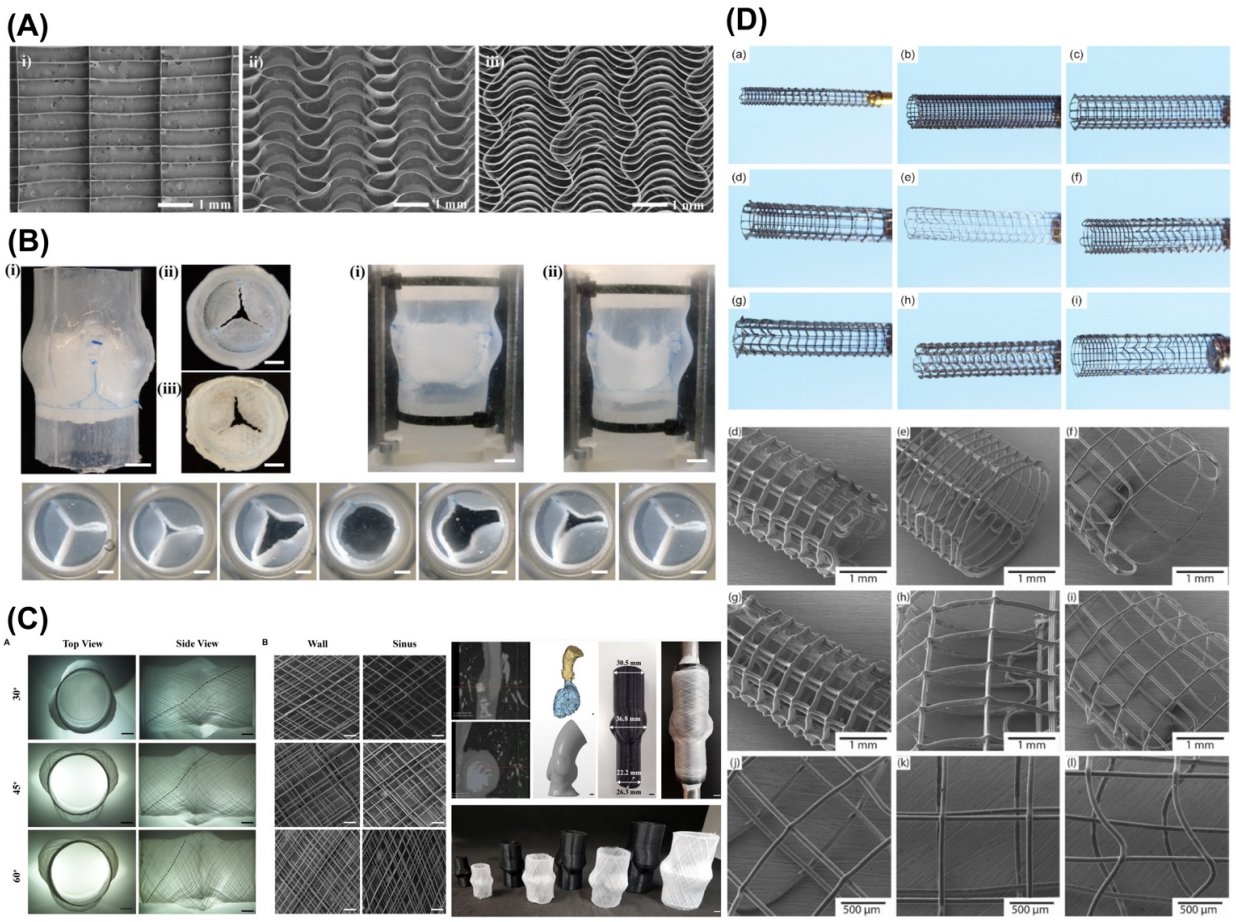

Figure 2-4 Biomimetic print designs of MES scaffolds
(**A**) Biomimetic serpentine patterns design for heart valve tissue engineering and **(B)** Custom-made flow loop system, where the MEW scaffold is sutured into a silicone aortic root as single leaflets and functionality assessment of the opening and closing sequence of the valve. From Saidy et al. (2019). (**C**) Characterization of scaffolds printed at 30°, 45°, and 60° winding angle for fabrication of personalized aortic root scaffolds. From Saidy et al. (2020). (**D**) Stent-like structures produced from polycaprolactone-reduced graphene *oxide (PCL-rGO) using MEW at multiple strut geometries. From Somszor et al. (2020).*

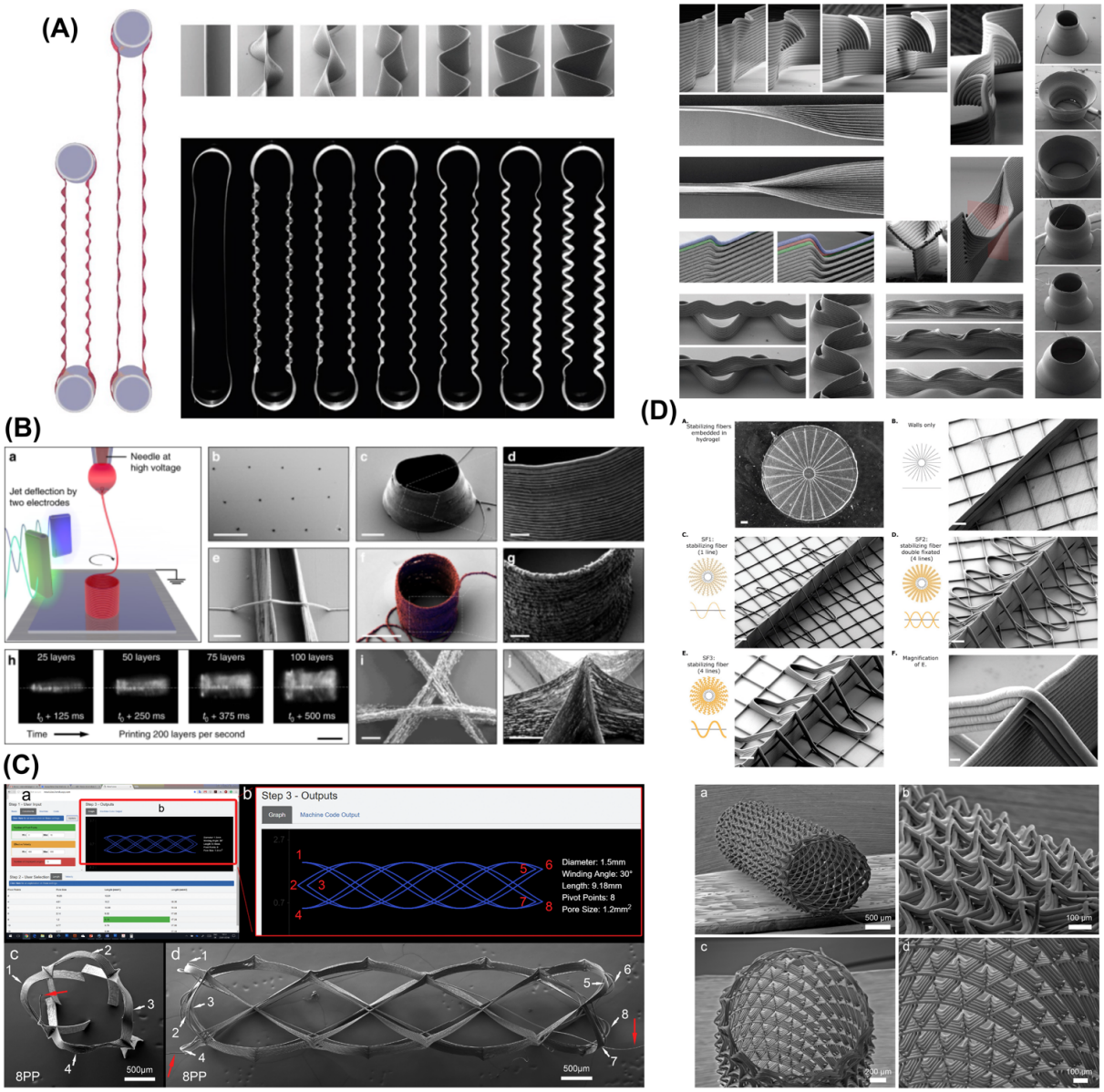

Figure 2-5 Various complex MEW scaffold design

(**A**) Novel complex overhanging structures by controlled layer shifting and multiphasic walls formed by an abrupt change in printing trajectory. From Liashenko et al. (2020). (**B**) Ultrafast 3D printing of cylindrical microstructures single suspended polyethylene oxide (PEO) fiber bridging a gap between 2 parallel nano wall using electrostatic jet deflection. From Liashenko et al. (2020). (**C**) Web-based application, to generate printing path for porous tubes like structure for TE. From McColl et al. (2018). (**D**) Variants of stabilizing fibers produced in a radial manner. From Ruijter et al. (2018).

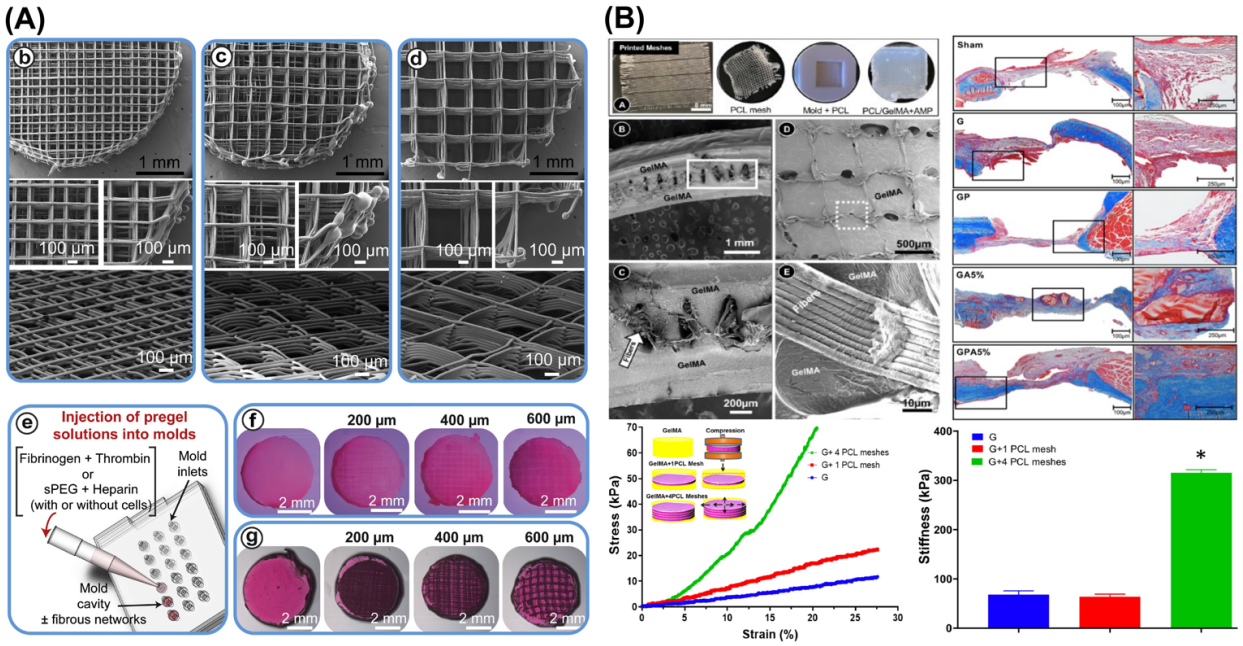

Figure 2-6 MEW–hydrogel reinforced composite approaches
(**A**) MEW enabled a good control intended 0°-90° crosshatch at 200 µm, 400 µm, and 600 µm fiber spacing for fiber-reinforced hydrogels of fibrin, sPEG/Hep and hydrogels. From Bas et al. (2017). (**B**) Amorphous magnesium phosphate (AMP) modified gelatin methacryloyl (GelMA) hydrogel infiltrated highly porous MEW PCL meshes with well-controlled 3D architecture. Note the hydrogel phase uniformly infiltrated within the highly order porous structure. Stress-strain curves and stiffness of GelMA indicates higher results when increasing the number of PCL meshes. From Dubey et al. (2020).

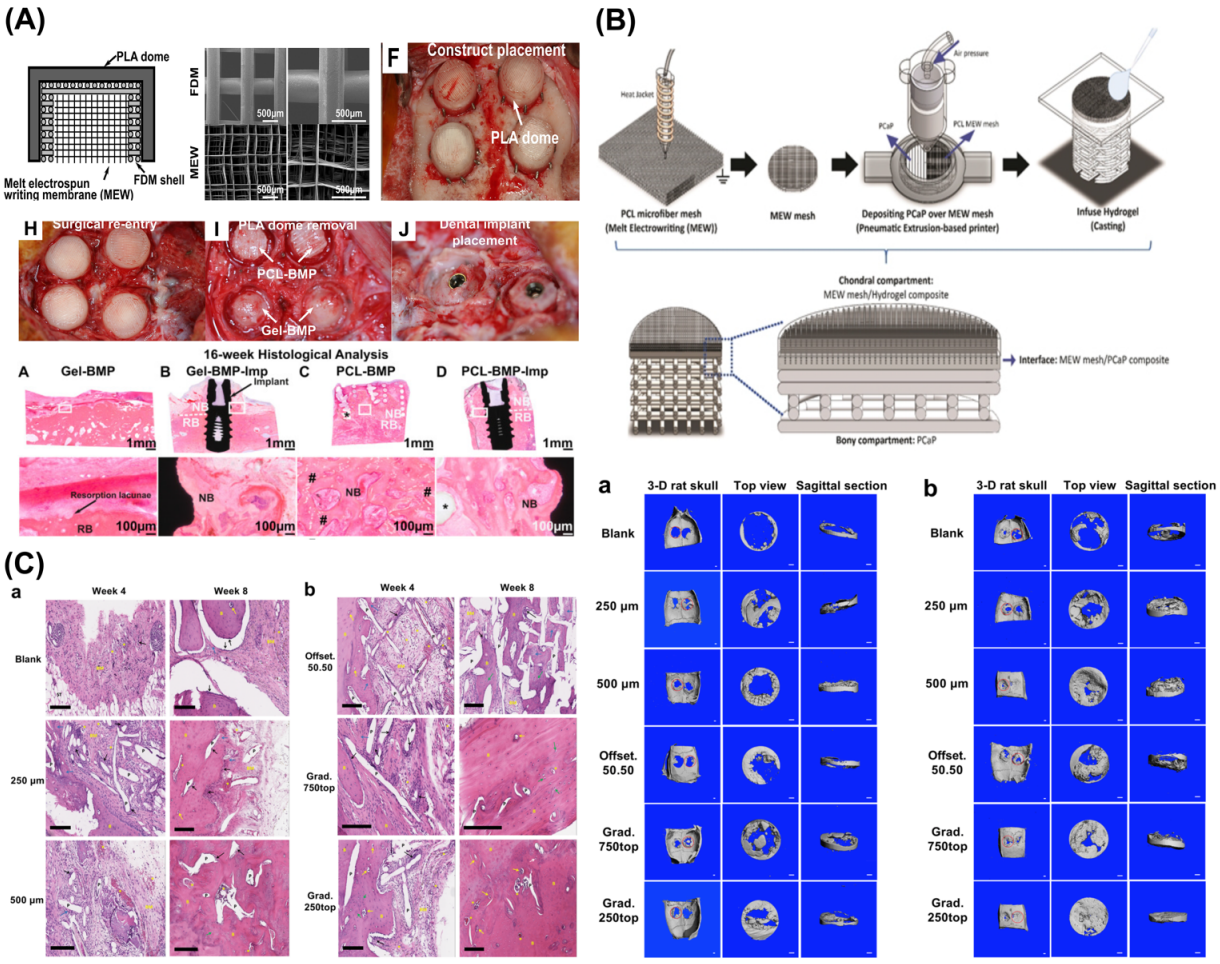

Figure 2-7 Multilayered/Multiphasic scaffolds for osteochondral and periodontal regeneration

(**A**) Multiphasic construct for vertical bone augmentation, graphic view of melt electrospun mesh inserted to FDM scaffold and PLLA dome shaped construct and Surgical implantation of constructs onto the sheep calvarium. Adapted from. From Vaquette et al. (2021). (**B**) Schematic illustration of the multiscale osteochondral construct processed via melt writing electrospun fibers reinforced hydrogel-ceramic interfaces. From Diloksumpan et al. (2020). (**C**) Bone regeneration assessment of offset and gradient MEW scaffolds implanted in rat calvarial defects and 3-D reconstructed Micro-CT images showing the degree of bone repair at 4 weeks and 8 weeks post-implantation. From Abassi et al. (2020).

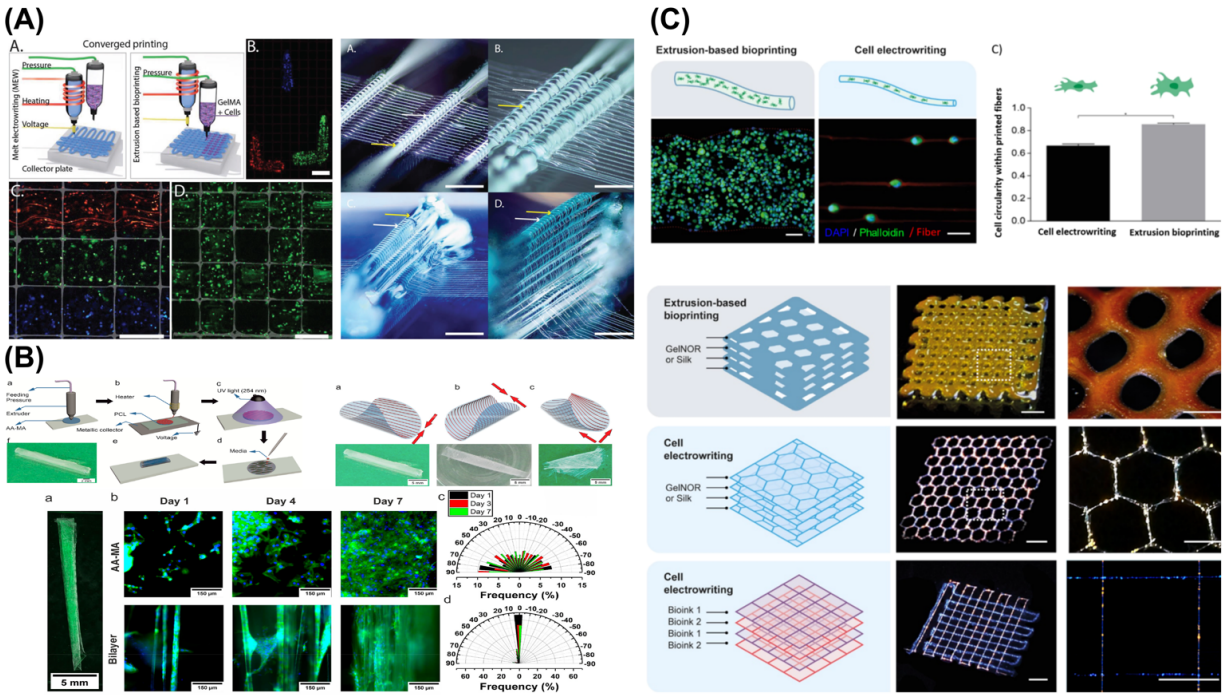

Figure 2-8 Multitechnology biofabrication approaches

(A) Cell distribution and out-of-plane printing architecture. From Ruijter et al (2019). **(B)** Bilayer self-folded tube via 3D printing and melt electrowriting (MEW) of PCL fibers on methacrylated alginate (AA-MA) hydrogel, can be folded at different directions direction; parallel, perpendicular, or diagonal-wise. The presence of MEW fibers support Myofibroblast orientation to a higher degree not achievable by AA-MA film without fibers. From Constante et al. (2021). (**C**) Cell electrowritten (CEW) fibers on gelnor-based cell-laden scaffolds compared to conventional extrusion bioprinting. Single cells precisely aligned along the pattern in CEW while extrusion-bioprinted fibers had thicker filament of multiple cells distributed homogeneously. CEW allows simultaneous multiple bioinks printing in a single construct. From Castilho et al. (2021)

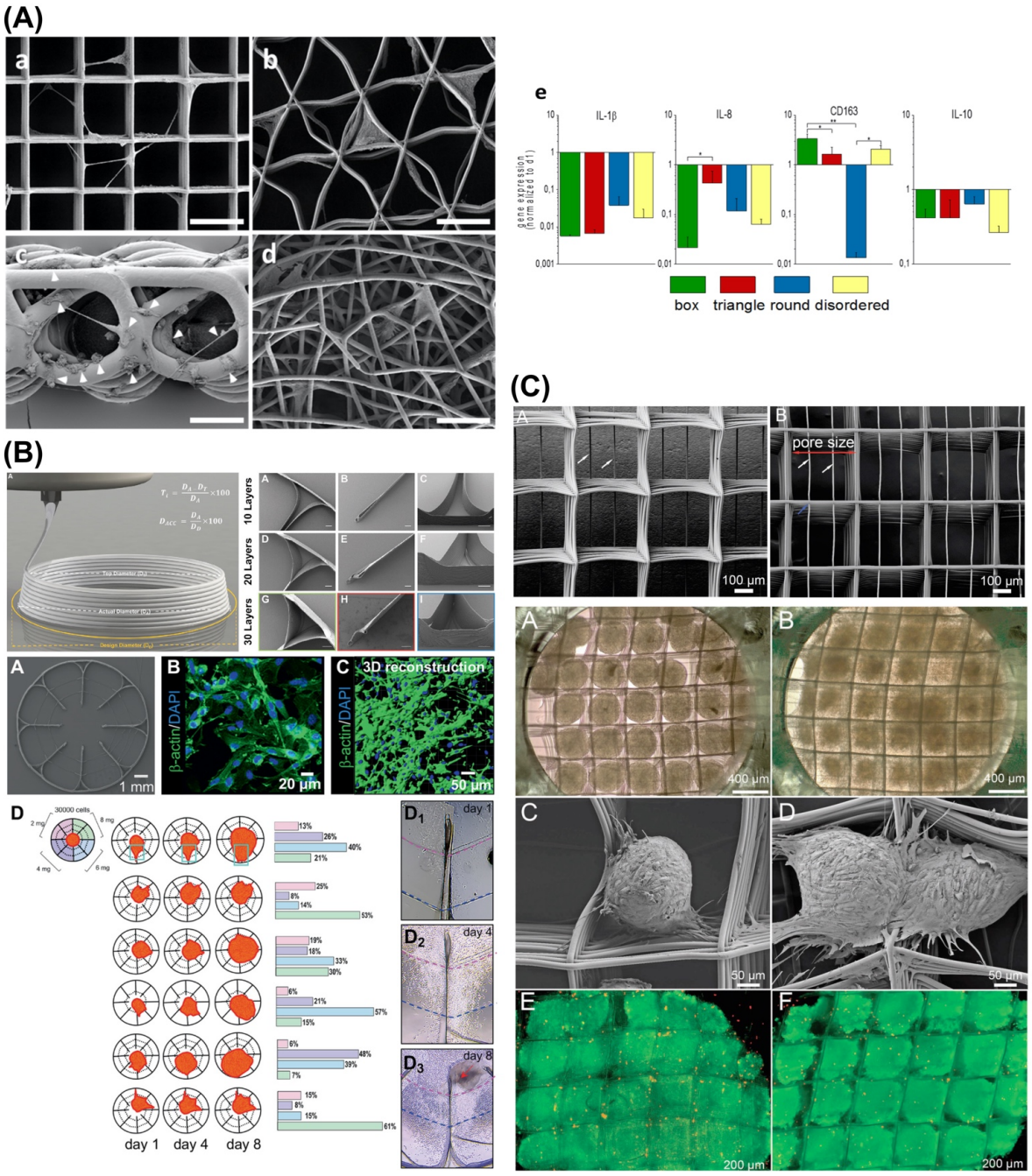

Figure 2-9 Current *In vitro* platforms for MEW for studying disease and engineering tissues

(**A**) Macrophages and MEW scaffold interaction suggested spontaneous differentiation of M1 toward the anti-inflammatory type (M2), while both M1-markers, IL-1β and IL-8, were decreased and the M2 markers, CD163 and IL-10, rather increased. From. Tylek et al. (2020)**.** (**B**) Schematic of the MEW circular structure of a 3D *in vitro* radial culture device for glioblastoma cell migration analysis. From Bakirci et al. (2020). (**C**) Adipose stem cells (ASC) spheroids in box-structured MEW scaffolds shows attachment to the fibers and adjacent spheroids. From McMaster et al. (2019).

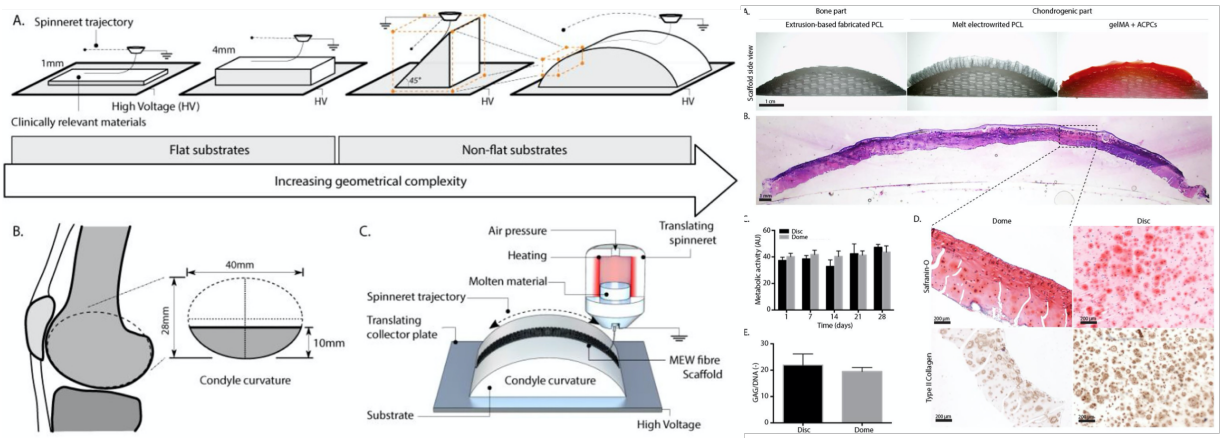

Figure 2-10 Tissue-specific scaffolds/constructs that direct stem cells differentiation and mimic the biomechanics of the tissue to be regenerated
Non flat geometries via resurfacing PCL to mimicking the contour of a human femoral condyle surface, enables cartilage-like tissue formation. From Peiffer et al. (2020).

Table

Table 1. List of studies utilized MEW based technique for fabrication of scaffold and system configurations as well as outcomes.

The following abbreviations are used: P (applied pressure), FR (flow rate), V (voltage), CD (collector distance), Tm (temperature), Vel (collector speed), S (Strand spacing) and FD (fiber diameter)

Polymers & Additives	Parameter	Design	Cell	Outcome summary	Ref.
PCL	FR= 50 µL h^{-1} V= 12 kV TM= 70 °C CD= 3 cm 21G	S=20 µm FD=21 µm	N/A	Jet and collector contact located directly below the spinneret must be close to the jet speed for controlled fiber deposition.	25
PCL/CaP	FR= 50 µL h^{-1} V= 12 kV TM= 78 °C CD= 4 cm 21G	Tubular S= 6.9-4.8x10^{-2} mm^2 FD=19.9-27.7 µm	OB	Winding angle (WA) can control scaffold pore (*e.g.*, size, shape, number and porosity). Increasing WA decreases FD and spacing.	79
PCL	FR= 10 µL h^{-1} V= 10 kV Tm= 80 °C CD= 4 cm Vel=2.5×10^{-2}m/s 23G	S= 46 µm FD=7.5 µm	Dermal fibroblast	The translational speed of the collector allows for straight fiber morphology in the MEW structure.	80

PCL	FR= 10-20 µL h^{-1} V= 4-14 kV Tm=80-90°C CD=1-3 cm 21-23G	Patterned FD= 5-35 µm	N/A	Low flow rate, collection distance and high applied voltage allow production of small FD. In contrast, high flow produces larger FD.	[35]
PCL	FR= 40 µL h^{-1} V=1.05 kV /mm TM=73 °C CD= 1 cm Vel= 750 mm/min 21G	90°-cross-hatched S= 1 mm FD= 40 µm	MC3T3	Highly ordered 2mm thick scaffold was produced by use of dual voltage power supply, positive voltage on needle tip and negative voltage on collector plate.	[81]
GelMA/PCL	FR= 18, 72 or 180 µl h^{-1} V= 8–10 kV Vel=1400 mm/min 23 G	0°to 90° l S=0.2-1 mm FD= 19.4, 48.5 and 88.5 µm	Human chondrocyte	Stiffness of the constructs significantly enhanced by enforced PCL/GelMA composite, to achieve values similar to native articular cartilage.	[50]

PCL	P= 0.5-4.0bar V= 2-10 kV TM=80-120°C CD=1-10mm Vel=1000-9000mm min^{-1} 21-33G	0-90-Box shape FD= 817 nm S=100.6 *μ*m.	N/A	Dynamic balance of MEW processing parameters allows production of high-quality small FD. NCO-sP (EO-*stat*-PO)-coated slide prevents scaffold detachment *in vitro.*	7
PCL/ Poly(2-oxazolin)/hydrogel	FR= 20μL h^{-1} V= 11.7 kV TM=120°C CD=1.5 cm 23G	90-laydown S=200-600 μm FD= 23 ± 1 μm	N/A	PAOx copolymers are amphiphilic, therefore PEtOx-ButenOx used to wetting PCL fibers and eliminate defects between PCL and hydrogel.	51
poly (LLA-ε-CL-AC)	V= 7 kV Mt=145 P=3.0 bar CD=4.5mm Vel= 7mm /s 33G	90-laydown S= 100 μm FD= 24.6 μm	N/A	Poly (LLA-ε-CL-AC) photo-cross-linkable amorphous polymer that flows upon heating at intermediate Tm and have high (T_g) rapidly solidify once melt-printed.	82

PCL/CaP/ pretreated NaOH	FR=10µl/h V=11-12 kV CD=2cm Tm=100°C 23G Vel=2000 mm/min	0-90-laydown S=100 µm FD=18 µm	OB/placenta - stem cells	3D endosteal microenvironment of CaP coated scaffold was suitable for growth and migration of HSCs towards bone matrix.	[70]
PCL/star-PEG heparin	FR= 50 µL h^{-1} V= 10 kV Tm= 78 °C CD= 4 cm 21G	Tubular scaffolds FD=8.5 µm	HUVEC and BM-MSC	*in vivo* multiphasic platform has been constructed to simulate both the cellular and morphological components of periosteum	[75]
PCL/sPEG/Hep hydrogels	FR=20 *µ*l h^{-1}. V=12-12.5kV Vel=0.7m min^{-1} Tm=100°C CD=1.5, 23G	0°–90°-laydown S=200-600 µm FD=21.36 µm	Human chondrocytes	The combination of star poly (ethylene glycol) / sPEG / Hep/PCL produces mechanical anisotropy, similar to cartilage microenvironments.	[52]

Polypropylene (PP)	P=0.5-1 bar V=6.2kV Tm= 215 °C CD=3.3 mm 25G Vel=0.625-750 mm/min	90°-laydown S=0.2-1 mm FD=16.4 µm	N/A	PP provides different designs of fibrous textiles for use in medical applications.	83
pHMGCL/PCL	pHMGCL: P=2bar V=5kV CD=3mm Vel=5 mm s^{-1} PCL: P=3 bar V=7kV CD=3mm Vel=25 mm s^{-1} Tm= 87-94 °C	Rectangle/ square S=150 µm FD=3-12 µm	Cardiac progenitor cells	MEW of pHMGCL/PCL, triangular pattern approximates the mechanical properties of native myocardial component and promote CPC's alignment for cardiac engineered tissues.	20

PCL/ GelMA	P=2bar V=7kV Tm=75 C°, 70 C° Vel=0.3m/min 23G	0–90°, 0–60° or 120° Lay-down S=250,5 or 750 µm	hBMPCs	Tuned biomechanical properties of *J*–shaped σ–ε curve (up to a strain of ~0.40) distinct phases (toe, heel and linear) resemble collagen fibril.	9
poly (methyl methacrylate)	V=3 kV Tm=250°C CD=500 µm-5 mm Vel=15 mm/s	FD=500 nm to 6 µm	N/A	Method for fabrication of a micro/nano-optical fibers MNOF based on near-field melt electrospinning.	84
PCL	P=0.8,1.5 or 2.6bar V=8, 11or 12kV Tm=65 °C CD=12mm Vel=1700,1200 or 700 mm/min 23G	0/90 or 0/60 laydown FD=3-30 µm	N/A	Small fibers of ~3-10 µm, is accessible when coordination is achieved between low pressure, moderate voltages and high collection speed. In contrast, high pressure allows for polymer flow and larger FD ~10-20 µm.	29

PCL	P=1.9 bar V=5.6 kV CD=4.5mm Tm=96°C 25G Vel=3500mm/min	Box-shape S=100 -350 μm FD=7 μm	HUVECs and NHDF	Orientation of capillary-like structures, and guidance of neovascular-like structures to the center of the pores, dependent on the pore size of the scaffolds.	[73]
PCL/ pHEMA	P=2.0 bar V=6kV T=90°C Vel=900-1200 mm/min CD=3mm 25G	FD=13.3 μm	N/A	Out-of-plane deposition of an electrically charged polymer melt, resulting in stabilizing fibers, increased the shear modulus could potentially be used to reinforce hydrogels.	[54]
PCL/GelMA	P=3.0 bar V=5.5 kV VEL=10 mm/s Tm=90°C 23G	S=200, 400, 600 or 800 μm. FD=20 μm	N/A	MEW/hydrogel reinforcement includes fibers being pulled in tension to create lateral expansion of the hydrogel and the interconnections create multiple interlocking.	[53]

PCL	V=7, 8, or 9 kV CD=8-18mm	S=1000 µm FD=20 µm	PDL cells	Computational modeling provides numerical values of variable working distances to maintain the electrostatic force at constant level for ~7 mm height MEW construct.	[30]
(DMS-A12-HMDI	P=1-3 bar V=8-12kV Tm=80-100°C CD=8.5mm	FD=10 to 20 µm	N/A	FD is significantly influenced by the applied voltage and fiber fusion effects at the intersections allow to build a MEW construct in height.	[26]
PCL	P=0.5-4 BAR V=7kV Tm=73°C CD=6mm 22G	S=300 FD=2-50 µm	hMSCs	When the speed of the collector is kept above the CTR, the highest accuracy of MEW can be achieved. The FD can be adjusted by FR and collector speed.	[31]

PCL	P=10 to 50 kPa V=8, 10, 12 kV Tm= 80, 90 or 100 °C CD=20mm 21G	90°, 45°, 10° or round S=300 µm FD=10.4 µm	hSSCs	Fiber orientations dictate cell morphology, mechanosignalling and lineage commitment. Cells cultured in 90° laydown have shown a lower aspect ratio, greater spreading, greater cytoskeletal tension and nuclear YAP expression.	[68]
PCL/GelMA	P=1 Bar V=5 kV Tm= 85 °C CD=6mm Vel=80 mm s^{-1}	Square S=100, 200 or 400 µm FD=13 µm	Quine-derived (eMSCs)	MEW/hydrogel provides mechanically and biologically competent constructs, enhances MSCs differentiation into cartilage.	[64]
PCL	P=0.8-2.2 bar V=8-12 Tm=70-95 °C Vel=1-3x10^3mm min	Small	N/A	The degree of the electrostatic acceleration is correlated to the charge density of polymer melt and flow properties.	[28]

PCL/MATRIGEL	P= 3 bar Tm=80°C	Square S=100, 200 or 400 µm FD=9.7mm	Ltk-11 fibroblast	Electrophysiology of a glycine receptor-transfected Ltk-11 mouse fibroblast in MEW/reinforced Matrigel	[42]
PCL	FR= 400 mm/m P=1.2 bars V= 6 kV Tm=73.0 °C	0°-90° box shape S=225, 300, 375, 450 or 500 µm FD=20 µm	MG63	Box-shaped construct with pore sizes between 225 µm and 500 µm, allows for osteoblast attachment and differentiation.	[38]
PCL/CaP	P= 1.16 bar V=11kV Tm=90 °C	S= 100 µm FD=10 or 13 µm	OB and PBMC	Cell/non-mineralized ECM density in scaffold cultured OB or OB+PBMC, *in vitro* system for bone regeneration.	[85]
PCL	P= 1.2 bar V=11kV TM=73 °C CD=4mm Vel=400 mm/min 22G	90°/0° or 60° S=200 µm FD=20 µm	MG63, HaCaT and L929	Different geometries of MEW were individualized for OB attachment on one side and for keratinocytes on the other side. Film casting formed core for bacteria-tightness.	[39]

PCL	P=0.5-1.2bar Vel=500-1500 mm min	Box-shape S=360 µm FD=13-15 µm Catching, S=130 µm FD=7-8 µm	ASC-Spheroid	MEW construct tailorable to spheroid size were seeded with ASC spheroids, to further utilization for adipose tissue regeneration.	[34]
PCL/CaP cement	V= 12 kV CD=2mm 27G	Box-shape S=200, 500 or 1000 µm FD= 8 µm	N/A	Treating PCL with NaOH increases strength and maintains high fracture energy ~1.5 to 2.0 mJ / mm^2 for application in planar or curved cranial defects.	[86]
NCO-poly (ethylene oxide-stat-propylene oxide) /PCL	P=1.9bar V=5.6kV Tm=96 °C CD=4.5mm 25G	0-90-Box-shaped S=200 µm FD=7 µm	Primary hMSCs	Photo-leucine is covalently immobilized into the sP(EO-stat-PO) results in a photoactivatable scaffold that enables binding of sterically demanding molecules.	[87]

PCL/SrBG	P= 0.050 MPa FR= 2.39 mm min^{-1} V=6kV Tm= 55 °C CD= 10 mm	Square- crosshatch S= 1 mm	N/A	Platform of high ceramic-content polymer scaffolds for applications in bone tissue engineering was successfully processed.	88
PCL	FR=25µl/h V=10-12kV Tm=78°C G=21 Vel=80mm/s	0–90° or 0–45° S=19 or 35 µm FD=5 or 7 µm	Fibroblast (NHDFs)	Bioinformatics-guidance of single-cell confinement are modeled. Unlike flat surface, cells develop cluster of mature FAs at 0–45°.	89
PCL	P-2 bar V=6-6.5kV Tm=85°C CD=4.5mm Vel=280mm/min 23G	Serpentine FD=0.5 or 1 mm S=0.25, 0.5 or 1 mm	vascular smooth muscle	The serpentine structure reproduces the J-shaped strain hardening behavior and anisotropic composition of natural valve leaflets.	43
Milk proteins/PCL	P=100kPA FR= 12 mm s−1 V=20kV Tm= 85 °C	90°-angle S= 300 µm FD=50 µm	Keratinocyte & Fibroblast	Increased cell growth and infiltration into PCL/MP scaffolds have potential in dermal tissue regeneration.	90

PCL	P=70kPa Tm=80 CD=1.5 mm Vel=3mm/s	Square/ rectangle S=200 μm FD=0–50 μm	N/A	Decreased FD when stage speed is decreased and Tm increased, and vice versa. Tailoring the parameters provides structural anisotropy mimic native ECM	[41]
PCL/CaP	P=2.2 bar V=10.1kV Tm=74-85°C 23G	0°–90°' S=150 μm FD=12 μm	hPOB & prostate cancer	MEW simulate the bone-like 3D microenvironments and produce *in vitro* model to study metastases in bone.	[69]
PCL	P=10kPa V=150V Tm=90°C 21G CD=2Cm Vel=17mm s^{-1}	Square S=100, 200, or 300 μm FD=4.01 μm	hMSC	Small pore size of 100μm is optimal for hMSCs as it demonstrates the highest global stiffness, local fiber stiffness and enhances mineralization.	[40]

PCL	P=10kPa V=7kV Tm=77°C CD=1.4mm Vel=950 mm min^{-1} 30G	Box, Triangle, round or disordered S=40=100 µm FD=2.6-2.9 µm	Monocyte	Geometry and spacing from 100 to 40 µm facilitate macrophage elongation and polarization, an evidence to consider the design of biomaterials to positively impact tissue regeneration.	[33]
PCL/CaP	FR= 20 mL/h V=5-7kV Tm=80°C CD=10mm 21G	30 50% layout FD=6-10 µm	hOB	Offset and gradient scaffold have shown to upregulate ALP activity and matrix mineralization of osteoblasts.	[32]
α-TCP/ hydrogel/PCL	P=1.5bar Tm=90°C Vel= 50 mm s^{-1} V=10kV	Box-patterns S= 300 µm FD=10 µm	ACPCs and MSC	Hydrogel/ ceramic enhances adhesion strength >6.5-fold, enables structural stability in *ex vivo* osteochondral defect	[61]

PCL	P=0.05 MPa V= 4.5 for flat and 5.5 for tubular Tm= 86 °C 21G Vel= 900 mm/min	90°, 50° or 20°/crosshatch/gradient/ & tubular S=850-250 µm FD=3-16 mm	MC3T3	Customized pattern generation software has been developed to enable the design of MEW scaffolds.	[36]
PCL/ Purasorb PC 12	P=180 kPa V=8 KV Tm=75 °C CD=10mm 23G Vel=1000 mm/min	S=200 µm FD= 10-20 µm	hMSCs	Bone-Ligament-Bone (BLB)/ cell sheets construct enhanced mechanical properties regardless of the pattern and fiber orientation can induce spontaneous cell organization	[67]
PCL/ Matrigel	P=3bar V=6kV Tm=80°C CD=4mm 25G	Crosshatch S=200 µm	Cortical neuronal cells	Reinforced Matrigel have enhanced cortical neurons viability, maturity and faster dendrites formation for potential 3D study model of neuronal networks	[91]

CHAPTER 3

A Highly Ordered, Nanostructured Fluorinated CaP-Coated Melt Electrowritten Scaffolds for Periodontal Tissue Regeneration

Abstract

Periodontitis is a chronic inflammatory, bacteria-triggered disorder affecting nearly half of American adults. Although some level of tissue regeneration has been realized, its low success in complex cases demands superior strategies to amplify regenerative capacity. Herein, highly ordered scaffolds were engineered via Melt ElectroWriting (MEW), and the effects of strand spacing, as well as the presence of a nanostructured fluorinated calcium phosphate (F/CaP) coating on the adhesion/proliferation, and osteogenic differentiation of human-derived periodontal ligament stem cells, were investigated. Upon initial cell-scaffold interaction screening aimed at defining the most suitable design, MEW poly(ε-caprolactone) scaffolds with 500 μm strand spacing were chosen. Following an alkali treatment, scaffolds were immersed in a pre-established solution to allow for coating formation. The presence of a nanostructured F/CaP coating led to a marked upregulation of osteogenic genes and attenuated bacterial growth. *In vivo* findings confirmed that the F/CaP-coated scaffolds are biocompatible and lead to periodontal regeneration when

implanted in a rat mandibular periodontal fenestration defect model. In aggregate, we consider that this work will contribute to the development of personalized scaffolds capable of enabling tissue-specific differentiation of progenitor cells, and thus guide simultaneous and coordinated regeneration of soft and hard periodontal tissues, while providing antimicrobial protection.

KEYWORDS: *melt electrowriting, 3D printing, scaffold, bone, periodontitis, periodontal regeneration*

3.1 Introduction

Periodontitis (gum disease) is a ubiquitous chronic inflammatory, bacteria-triggered disorder affecting nearly 50% of American adults.[1] If left untreated, it leads to severe destruction of the periodontium (*i.e.*, cementum, periodontal ligament [PDL], and alveolar bone), eventually resulting in tooth loss.[1,2] Over the years, countless therapies have been investigated for regenerating tooth-supporting tissues lost as a consequence of periodontal disease progression. Hitherto, the management of periodontal tissue destruction encompassed scaling and root planing, flap surgery, and guided tissue regeneration by means of a degradable membrane that, while serving as a barrier against soft tissue infiltration, allows resident progenitor cells to promote the regeneration of periodontal tissues.[2] Although some level of tissue regeneration has been realized, the low success in complex cases (*e.g.*, horizontal defects) demands superior strategies to strengthen regenerative capacity, regardless of damage severity.

Recent advances associated with the development of scaffolds that provide desirable functionalities, including anti-inflammatory, antimicrobial, and regenerative attributes by means of the incorporation of drugs and/or biologics, as well as engineering tools to devise

defect-specific scaffolds, have been witnessed.[3,4] Significant progress has been made that leverages the electrospinning (solution-based) nanotechnology for the fabrication of versatile biodegradable scaffolds with three-dimensional (3D) nanofibrous microstructure resembling the extracellular matrix (ECM) of native tissues. However, this method, fails to generate scaffolds with patient-specific geometries that address the 3D architectural complexity of periodontal defects. Moreover, the rather flat, densely-packed fibrous structure of electrospun scaffolds often limit cellular infiltration.[5] Collectively, the lack of controlled fiber deposition and space between adjacent layers has ignited the search for technologies capable of not only mimicking the microstructural features of native ECM, but also creating geometrically defined scaffolds for periodontal tissue reconstruction.

Additive manufacturing (AM) technologies, such as fused deposition modeling (FDM) and selective laser sintering (SLS), have paved the way for fabrication of defect-specific scaffolds.[6] Although AM has been deployed to engineer personalized biomaterials for regenerative medicine applications (*e.g.*, tracheal splints), data from a seminal clinical study in periodontics demonstrated that, even though a patient-specific scaffold in poly(ε-caprolactone) (PCL) could be made, its overall ability to fabricate constructs with a degradation rate matching that of periodontal tissues' regeneration remains intangible, particularly due to the generally bulky nature of the printed scaffold.[6] To address this technology gap, Melt ElectroWriting (MEW) holds significant potential, since it allows for the generation of microscale fibers and controlled fiber deposition to ultimately create more physiologically relevant 3D scaffolds for periodontal tissue regeneration. Worth mentioning, MEW not only enables the fabrication of scaffolds with cell-invasive ability, but also macro- and microstructural features, such as scaffold porosity, as well as fiber

diameter and alignment to match tissue-specific requirements, respectively. Worth noting, post-processing modifications are accessible through coating strategies aiming at regulating cell differentiation and tissue formation. In this way, in view of the hydrophobic character of PCL and its poor cellular attachment ability, surface modification using plasma, alkali-treatment, or calcium phosphate (CaP) coatings has been investigated.[7] Remarkably, fluorapatite (FA), a bioceramic within the CaP family, has been shown to favorably influence osteogenic differentiation while also displaying antimicrobial action, which, in the case of periodontal regeneration, would be important for preventing bacterial colonization.[8] Moreover, Sikder *et al*. reported on the bioactivity of fluoro-hydroxyapatite coating and its potential to form bone-like apatite globules.[9]

In this work, PCL scaffolds were fabricated via MEW, the effects of strand spacing, and the presence of a fluorinated CaP (F/CaP) coating on the attachment; proliferation and osteogenic differentiation of human-derived periodontal ligament stem cells were investigated to refine the most favorable candidate for use as bone region in a zonal, tissue-specific scaffold for periodontal tissue regeneration. MEW was utilized to print box-structured scaffolds by alternating the layer deposition via 0°/90° layers to obtain three distinct strand spacings (up to 1000 µm). Upon initial screening of cell-scaffold interaction to define the most suitable scaffold design, 500 µm strand spacing was chosen. Following an alkali treatment, the aforesaid scaffolds were immersed in a pre-established solution to allow for coating formation. A nanostructured F/CaP coating was observed on the MEW printed PCL fibers through high-resolution imaging. The presence of the nanostructured F/CaP coating led to a significant increase in cell proliferation and marked upregulation of osteogenic genes. Moreover, the antimicrobial character of the F/CaP-coated scaffolds

was examined. Our data indicated a minor, yet significant action against *P. gingivalis*. *In vivo* findings demonstrated that the F/CaP-coated scaffolds are biocompatible and lead to periodontal tissue regeneration when implanted in a well-established fenestration defect model in rodents.

3.2 Results and Discussion

3.2.1 Fabrication and Characterization of MEW PCL Scaffolds

MEW was utilized to engineer highly ordered polymeric (PCL) scaffolds for periodontal regeneration (**Figure 1a)**. The scaffolds showed uniform 3D architecture in all designed strand spacings, with well-aligned fibers having an average fiber diameter of 2.3 ± 0.1 μm and an overall porosity (%) of 91.7, 93.9, and 94.4 in 500, 750, and 1000 μm strand spacing, respectively. It is well-known that PCL has low surface hydrophilicity, which limits cell adhesion.[10] In order to improve the wettability of the generated fibers and enhance cellular attachment, the scaffolds were etched with sodium hydroxide (NaOH).[11] Next, to assess the effect of the varying scaffold strand spacings on cell attachment and proliferation, human-derived periodontal ligament stem cells (hPDLSCs) were seeded, and then observed with confocal laser scanning microscopy (CLSM). Improved cell attachment and proliferation on scaffolds having 500 μm strand spacing was noted when compared to the larger (750 μm and 1000 μm) strand spacing designs (**Figure 1a)**. It was observed that scaffolds with a strand spacing of 500 μm exhibited superior cell bridging after 3 days than scaffolds with larger strand spacings. These findings confirm that strand spacing plays a role in cell attachment and proliferation.[12] For quantitative purposes, we evaluated whether increased strand spacing could affect cell viability using the

alamarBlue™ assay (**Figure 1b)**. Cell proliferation was statistically higher in 500 μm strand spacing scaffolds when compared to the other groups. At days 1 through 7, the effects of strand spacing were evident between 500 and 750 μm, while between days 7 and 28, a marked increase in viability was noted in strand spacings of 1000 μm. Particularly, on day 1 through 7 the viability of hPDLSCs on 500 μm strand spacing scaffolds was significantly greater than those in 750 and 1000 μm. Collectively, cells in small strand spacings (500 μm) had a higher contact rate, which allowed for faster spreading across strands. Our findings agree with previous studies, where cell proliferation was greatly influenced by pore size.[12,13] Noteworthy, at day 14, proliferation decreased in the 500 μm and 750 μm groups, possibly due to growth impairment due to cell-cell contact. In agreement with previous research, small strand spacings restricted cell infiltration and subsequently created more interactions between cells to promote differentiation (**Figure 1c)**, while cells in larger strand spacings were able to continue proliferating.[12,14] Altogether, due to halted proliferation in larger strand spacings at early timepoints and handling difficulties when using scaffolds with 750 *μ*m and 1000 *μ*m strand spacings, we focused on evaluating the potential of our innovative F/CaP coating solely on scaffolds with 500 μm strand spacing.

Apatite formation on inert polymers (*e.g.*, PCL) does not occur spontaneously, and specific surface modifications are needed to activate its surfaces.[11,15–19] Representative SEM images of the NaOH-etched and the F/CaP-coated scaffolds are shown in **Figure 2**. The fiber morphology of F/CaP-coated scaffolds revealed a unique nanostructured surface depicted as irregular-shaped nanoparticles (~ 50-150 nm) and a homogenous rough layer covering each individual fiber. Representative atomic force microscopy (AFM)

images of the scaffolds showed statistically significant differences in roughness. The PCL fibers of the coated scaffolds displayed the greatest mean roughness average (R_a) values, followed by the etched and pristine fibers **(Figure 2)**.

Next, we determined the chemical nature of the F/CaP coating through Fourier-transform infrared spectroscopy (FTIR) and X-ray diffraction (XRD). The FTIR spectra of the pristine (control) scaffolds showed characteristic PCL peaks at 2946 cm^{-1}, 2865 cm^{-1}, and 1720 cm^{-1}, corresponding to CH_2 and C=O stretching, respectively.[20] Meanwhile, apatite peaks were identified in the spectra of coated scaffolds (**Figure 3a)**. A broad peak stretching related to the phosphate group was identified between ~ 565 cm^{-1} and 960 cm^{-1}. Further, the broad band in the range ~ 3000-3750 cm^{-1} (O-H stretching) and the band identified at 1600 cm^{-1} suggests carbonated apatite formation.[21] The O-H stretching band at ~ 740 cm^{-1} indicates the presence of hydroxyl that bonded to fluorine (F-OH); however, the exact amount of fluorine cannot be determined.[22,23] The XRD pattern of the pristine PCL scaffolds displayed two sharp peaks at 21.4° and 23.8°, respectively (**Figure 3b)**; whereas, the coated scaffolds had a pattern similar to the non-coated scaffolds in addition to a discrete peak at ~ 31.8°, likely due to the CaP phase presence.

The thermal stability of F/CaP-coated scaffolds in comparison to non-coated (NaOH-etched) and pristine (control) are shown in **Figure 3c**. All scaffolds displayed a single-step stable thermal degradation profile with initial weight loss due to residual moisture removal, followed by degradation at 370°C, 320°C, and 350°C for pristine, non-coated, and coated scaffolds mainly attributed to large-scale thermal degradation of PCL. In addition, the residual weight of coated scaffolds at 550°C was 28.7%, thus confirming the successful chemical (F/CaP) modification. The DSC curves showed prominent

endothermic peaks of PCL at 61.9°C, 60.2°C, and 63.2°C in pristine, NaOH-etched, and F/CaP-coated scaffolds, respectively, attributed to the melting temperature (T_m) of PCL, followed by a maximum decomposition rate, which was observed at ~ 630°C in F/CaP-coated scaffolds.

To determine the chemical stability of coatings *in vitro*, the simplest physiological approaches include sample incubation in distilled water or deionized water. The ICP-MS data demonstrate constant Ca and P ions' release from the F/CaP-coated scaffolds over 7 days **(Figure 3d-e)**. At day 1, the concentrations of Ca and P reached a higher value of 3.96 and 2.35 µg/ml, respectively. While at day 3 and day 7, the concentration of ions shows constant release values of 1.85 to 1.05 µg/ml and 0.69 to 0.54 µg/ml for Ca and P, respectively. Despite the fact that the release data show continuous liberation up to 7 days of ions into water, the absence of buffer capacity does not appropriately mimic the *in vivo* scenario.[24] To simulate the *in vivo* environment, the chemical stability of F/CaP-coated scaffolds was also assessed after soaking the scaffolds in SBF. It can be seen from **Figure 3f** that after 1 week of SBF immersion, the residual mass for F/CaP-coated scaffolds was 26.3% and 21.4% for day 3 and 7, respectively. Meanwhile, when coated scaffolds were soaked in distilled water, the remaining mass was reduced nearly to half (14.1%) of the baseline data after 3 days, and to 7.9% at day 7. Collectively, the ICP-MS data and mineral phase stability (TGA) findings support the positive *in vivo* findings of abundant bone regeneration. Similarly, highly purified β-TCP in many clinical settings showed high potential to be readily absorbed and replaced by newly formed bone compared to HA, which is more resistant to biodegradation.[25,26]

The biomechanical properties of the scaffolds (*i.e.*, F/CaP-coated, non-coated (NaOH-etched), and pristine PCL with 500 μm strand spacing) were determined using a uniaxial tensile test (**Figure 3g)**. Regardless of the coating presence, the scaffolds showed a similar fracture behavior typical of most polymeric scaffolds – an initial elastic response, then considerable plastic deformation till failure.[27] The tensile strength and Young's modulus enhanced in the coated scaffolds when compared to the non-coated and significantly increased compared to pristine PCL. The data show clear enhancement of the mechanical properties as a result of uniform coating in the scaffolds. It is well-established that as the strength and rigidity of a scaffold increases, the elongation at break (%) decreases.[15] This behavior is obvious when comparing non-coated (~ 98%), pristine (~ 126.2) to F/CaP-coated scaffolds (~ 84%).

3.2.2 In Vitro Bioactivity of F/CaP-coated MEW PCL Scaffolds

The bone-forming potential of a biomaterial can be determined by evaluating the ability to form apatite on its surface *in vitro*,[16] following immersion in simulated body fluid (SBF).[17] SEM images **(Figure 4a)** show that, when F/CaP-coated scaffolds were immersed in SBF, re-precipitation of the apatite layer occurred, and it was followed by changes in the surface topography of the fibers and the formation of spherical cauliflower-like apatite morphologies. This is due to the ion exchange between the scaffold surface and SBF.[18] Meanwhile, the surface of NaOH-etched scaffolds revealed globules of mineral precipitates similar to previous observations for alkali-treated PCL upon SBF immersion.[28] Despite the trace of CaP precipitation detected in NaOH-etched scaffolds, visually, the coated scaffolds exhibited more apatite-like structures. The precipitates seen on the surface of the coated scaffolds continued to grow to form fully-covered surfaces

from day 7 to day 14 **(Figure 4a)**. Moreover, the EDS results **(Figure 4b)** showed that, as the immersion period increased, the calcium concentrations on the coated scaffolds also increased, thus reaching a ratio similar to that seen in natural bone.[29] This noticeable apatite-like phase formation on the coated scaffold likely occurred due to CaP deposition onto the scaffold's surface, which acted as a precursor of apatite and spontaneously allowed apatite growth by consuming Ca and P ions from the SBF solution.[16]

Complementary to that, **Figure 5a** shows the FTIR spectra of pristine (control), non-coated (NaOH-etched) and coated scaffolds immersed in SBF for 3 weeks, which also indicated suggestive peaks of crystalline apatite formed on the coated and the non-coated (NaOH-etched) scaffold counterpart. It should be highlighted that the PO_4^{3-} ions' main vibration bands, located ~ 1100 cm^{-1}, are overlapped with the PCL main characteristic bands. However, the emerged PO_4^{3-} absorbance at ~ 950-1100 and 550-620 cm^{-1} and the intensity of these bands increased with longer SBF immersion time. These observations are characteristic of fluorapatite and hydroxyapatite.[22] On the other hand, the carboxylate groups, formed on the non-coated scaffolds due to NaOH etching, were not sufficient to induce apatite nucleation, since less prominent bands were identified later between 14 and 21 days. The same pattern was evidenced with pristine PCL scaffolds, suggesting limited bioactivity. Additionally, the PCL peaks tended to decrease as the incubation time increased, due to partial hydrolysis of their organic component. This process is more evident for the C=O absorption peak at ~ 1720 cm^{-1} and ~ 1100 cm^{-1} and it became more noticeable as SBF immersion time increased. Importantly, the presence of OH^- and PO_4^{3-} on the surface of the F/CaP scaffolds, and the presence of a negatively charged surface, possibly attracted Ca^{2+} from SBF, leading

to the formation of Ca-rich CaP; and the process continued as the presence of calcium aggregation attracted more PO_4^{3-}.[18]

XRD patterns of F/CaP-coated, non-coated (NaOH-etched), and pristine PCL scaffolds before and after SBF immersion are shown in **Figure 5b**. A typical PCL pattern was shown in the ~ 20° and ~ 24° in pristine PCL, F/CaP-coated, and NaOH-etched scaffolds. After soaking in SBF, the F/CaP-coated group developed a broad peak in the range of 15°-25°, which should belong to the amorphous phase with small, weak crystallite, which illustrates that ion that precipitate gradually accumulate on the initial surface and belong to hydroxyapatite that gradually decreases with increasing soaking time in SBF. Non-coated (NaOH-etched) and pristine PCL scaffolds showed peaks at 31°-33°, which can be attributed to apatite formation. However, the peaks appearing at 32° that belonged to hydroxyapatite disappeared at day 21 in pristine PCL, which can indicate non-stable crystalline phase precipitation, and it might be related to weakly formed apatite as a result of the absence of -COOH on the surface of PCL. In contrast, although no clear peak at ~ 31° was evidenced in F/CaP-coated scaffolds at 7 days, after 2 weeks, a discrete peak appeared and increased after 21 days. These peaks are ordinarily associated with dicalcium phosphate dehydrate (DPCD), a possible bone substitute and nucleation precursor.[30] Thus, due to the formation of this new phase of crystalline CaP, we can state that the F/CaP-coated scaffolds are bioactive.

3.2.3 Effect of F/CaP-coated MEW PCL Scaffolds on Cell Compatibility and Function

From a cell compatibility standpoint, hPDLSC seeded on F/CaP-coated scaffolds show a significant increase in proliferation compared to non-coated scaffolds at day 3

through 14 **(Figure 6a-b)**, thus attesting to the cytocompatible character of the developed coating. Further, qualitative assessment of the role of F/CaP-coated scaffolds on cell attachment and proliferation was performed using CLSM and SEM imaging. Over time, DAPI/Phalloidin staining, along with SEM images, demonstrate hPDLSCs initially attached to the walls of the scaffold, and then to the corners of each individual strand, ultimately led to complete scaffold coverage (**Figure 6c-d)**. Focal adhesion points were prominent between cells and adjacent fibers and were more evident in the F/CaP-coated scaffolds (**Figure 6d)**.[31]

In this work, we hypothesized that the developed F/CaP nanostructured coating on the highly ordered scaffolds could enhance the osteogenic differentiation of human-derived periodontal ligament stem cells (hPDLSCs). hPDLSCs were seeded on coated and non-coated scaffolds and cultured in both basal and osteogenic conditions. At day 14, higher ALP activity was detected in the coated scaffolds cultured in basal media when compared to their non-coated counterpart cultured under the same conditions (**Figure 7a)**. This finding indicated that the coating provided the hPDLSCs the needed supplements to guide osteogenic differentiation. Furthermore, the F/CaP coating not only upregulated ALP activity, but also thrust hPDLSCs into forming mineralized nodules (**Figure 7b)**.

Alizarin red staining was used to identify mineralized matrix deposition. Worth noting, at days 14 and 21, hPDLSCs seeded on the coated scaffolds and cultured in basal media led to similar mineralization, when compared to the non-coated group cultured in osteogenic conditions. Remarkably, this observation further indicates the role of the

nanostructured coating as the predominant driving force for cellular commitment toward osteogenic differentiation. This was further confirmed through osteogenic gene expression for Runx2, Col 1, and OCN. At the early stage of osteoid matrix deposition in bone, Col 1 forms the major matrix component of ECM, whereas, in later stages, OCN is highly expressed by bone-forming cells. Additionally, Runx2 is the major regulator of BMP signaling that evokes the commitment of osteogenic differentiation, all of which was significantly upregulated at 14- and 21-days post-seeding in the coated scaffolds compared to hPDLSCs cultured in osteogenic media or on non-coated scaffolds **Figure 7c**. Overall, our nanostructured F/CaP coating promoted significant osteogenic differentiation of hPDLSCs as indicated by greater ALP activity, robust mineral deposition, and the upregulation of bone-related genes in the absence of osteogenic inducers.[4,32] Previous reports have demonstrated that CaP coatings can boost osteogenic gene expression and ALP activity in bone cells, as well as cell attachment ability and proliferation *in vitro*.[11] Furthermore, calcium and phosphorus ions have shown the ability to modulate osteoclast and osteoblast activity *in vivo*, due to their similarity to inorganic mineral phase crystals contained in bone.[11,33]

3.2.4 Effect of F/CaP-coated MEW PCL Scaffolds on Biofilm Inhibition

Fluorinated hydroxyapatite coating has been reported to exhibit higher antimicrobial activity against bacteria, such as *P. gingivalis* and *S. aureus*, than pure hydroxyapatite.[34] Moreover, the effect of surface topography on bacterial adhesion and biofilm formation has been vastly investigated.[35–39] Briefly, it is believed that the surface roughness and chemical composition of the coating influence bacterial adhesion.[40] Thus, we examined the antimicrobial potential of our nanostructured F/CaP-coated scaffolds

against *P. gingivalis*. Our data (CFU/mL) indicated minor, yet significant, action against *P. gingivalis*. AFM images demonstrated that while the surface of pristine PCL was the smoothest, both NaOH etching, and the F/CaP-coating increased the roughness of the respective fibers (**Figure 2)**. Surprisingly, the greater surface roughness presented by fibers of F/CaP-coated scaffolds did not increase bacterial adhesion and was similar to that exhibited by generally hydrophobic PCL scaffolds (**Figure 8a)**. We ponder that the fiber roughness of NaOH-etched scaffolds favored bacterial growth, which led to the highest bacterial counts. SEM images showed a significant amount of bacteria-forming microbial biofilms after 2 days of bacteria inoculation in NaOH-etched scaffolds, agreeing with the numerical (CFU/mL) findings. SEM images for both the pristine PCL and F/CaP-coated groups indicated a reduced number of viable bacteria compared to the NaOH-etched scaffolds (**Figure 8b)**. The reduced bacterial growth, even with a rougher surface, suggests an antimicrobial action due to the coating composition, as fluoride has been shown to affect bacterial metabolism.[34,41,42] Indeed, as previously highlighted by Gristina et al. in the “race for the surface” concept, where both host cells and bacteria compete to colonize implanted biomaterials,[41] here, our F/CaP-coated scaffold demonstrated bioactive, osteogenic, and antimicrobial features, critical to regenerate tissues in infection-driven diseases. Nonetheless, future experiments focusing on amplifying the antimicrobial efficacy are warranted.

3.2.5 Biocompatibility of F/CaP-coated MEW PCL Scaffolds

It is known that *in vivo* biocompatibility determines the long-term outcome of implanted scaffolds. Therefore, to determine the overall biocompatibility of the fabricated F/CaP-coated scaffolds, first, a well-established subcutaneous model was used to

explore cellular infiltration properties, morphological changes of the implanted scaffolds over time, blood vessel formation, and potential inflammatory cell response elicited by the engineered scaffolds due to their composition and/or degradation byproducts. Hematoxylin and eosin (H&E) images of retrieved and histologically processed scaffolds (*i.e.*, coated, non-coated, and thermal polymer extrusion, TPE) are shown in **Figure 9**.

A mixture of fibrin and connective tissue fibers, combined with a low extent of mononuclear cells, was observed within the explanted (7 days) scaffolds, *i.e*., F/CaP-coated and non-coated scaffolds. For both coated and non-coated scaffolds, host cells recognized the small diameter fibers as their initial attachment sites to align themselves and start the formation of collagenous ECM (**Figures 9 and 10)** over 28 days. In contrast, in TPE scaffolds, due to their large fiber diameter, a more scattered pattern of cell distribution was seen. In **Figure 9**, a significant ingrowth of host tissues can be noticed throughout the MEW scaffolds, with no observable signs of inflammation being detected at this early timepoint. Starting at day 14 post-implantation, the scaffolds of each group were integrated within tissue and the composition of this tissue was similar at day 28 (**Figure 10)**. Blood vessel ingrowth into F/CaP-coated, non-coated, and TPE scaffolds was observed. Blood vessel density increased from day 7 to day 28 in MEW scaffolds due to high porosity (**Figure 10)**. Interestingly, blood vessel infiltration was apparently higher in F/CaP-coated scaffolds, indicating that vascularization and cell invasion was enhanced in the presence of the nanostructured coating. Furthermore, blood vessel invasion not only occurred within strands, but also within strand walls in the coated scaffolds. It has been reported that the release of Ca ions from CaP-coated scaffolds

prompts endothelial progenitor cells and provokes the release of vascular endothelial growth factor (VEGF) via calcium-sensing receptor (CaSR) activation.[43,44]

3.2.6 In Vivo Evaluation of F/CaP-coated MEW/PCL Scaffolds Regenerative Capacity

Based on important *in vitro* findings, where the presence of the nanostructure F/CaP coating promoted significant osteogenic differentiation of hPDLSCs in the absence of chemical inducers, in addition to *in vivo* biocompatibility, we next pursued a clinically relevant, proof-of-concept *in vivo* study to examine the regenerative potential of the F/CaP-coated scaffolds. To that end, a well-established fenestration defect model[45,46] has been widely used to define the therapeutic efficacy of novel scaffolds and provide suitable clinical insight and a proof-of-concept prior to the larger animal model,[47] was used to mimic a clinical scenario of periodontal destruction (**Figure 11a)**.

Micro-CT and histological analyses showed that bone formation after 3- and 6-weeks post-implantation was significantly enhanced in defects treated with F/CaP-coated scaffolds, compared with non-coated scaffolds and non-treated (sham) defects (**Figures 11 and 12)**. At 3 weeks, bone volume (BV), bone fill (BV/TV) and tissue mineral density (TMD) were significantly higher in F/CaP-coated scaffolds compared to the other groups. The percent of bone fill, which indicate the amount of newly formed bone, were higher (with statistical significance $p<0.001$) in F/CaP-coated scaffolds than in the non-coated and sham groups **(Figure 11d)**. Similarly, by comparison, microCT data after 6 weeks revealed that bone volume (BV, TMD, and (BV/TV)) in F/CaP-coated scaffolds was significantly higher and demonstrated nearly complete bone coverage of the tooth roots compared to other groups. The 2D microCT images showed that F/CaP-coated scaffolds

were able to maintain PDL space similar to the non-treated lingual side. In this work, our F/CaP-coated scaffold was able to physically maintain the defect site and support infiltration and attachment of host progenitors capable of supporting the simultaneous and coordinated growth of both soft and hard periodontal tissues.

Detailed Masson's trichrome (MT) histological analysis demonstrated that the F/CaP-coated scaffold led to the regeneration of new alveolar bone, cementum, and PDL as early as 3 weeks post-implantation **(Figure 12a)**. Highly porous and micron-sized fibrous scaffolds allowed for an increase in vascularization and simultaneously supported multi-tissue periodontal regeneration **(Figure 12a)**. Compared to previous observations, the bulky nature and lack of adequate interconnected pores in scaffolds prepared via selective laser sintering (SLS) impaired wound healing and led to subsequent microbial contamination.[6] Here, the unique structure and associated porosity of the F/CaP-coated scaffolds obtained via MEW led to significantly higher amount of regenerated bone at both time points. Noteworthy, at 6 weeks post-implantation, the representative MT-stained images revealed new osteoblasts lining the organic matrix and osteocytes trapped in the lacunae of newly formed alveolar bone infiltrated with blood vessels. Moreover, newly formed connective tissue fibers were found deposited along the root dentin surface, in an orientation resembling physiologically healthy periodontal ligament (PDL) (**Figure 12b)**. Meanwhile, non-coated MEW PCL scaffolds displayed more collagenous, non-mineralized tissue and more soft tissue infiltration (**Figure 12b)**. Altogether, the engineered F/CaP-coated MEW PCL scaffolds contributed to a more robust and hierarchically organized periodontal complex of both soft (PDL) and hard (alveolar bone and cementum) tissues when compared to the non-coated scaffolds.

From a clinical standpoint, although existing therapeutics can lead to some degree of tissue regeneration, the low predictability and efficacy in cases of extreme tissue destruction call for improved strategies that can better replicate the three-dimensional (3D) and multi-tissue complexity of periodontal defects.[48] Precisely, currently, there are no approaches to predictably regenerate defects with considerable bone loss while avoiding tooth extraction. In previous work, a biphasic scaffold was engineered through the combination of fused deposition modeling to obtain an osteoconductive bone compartment using β-TCP/PCL and a periodontal ligament compartment using melt electrospinning to support PDL cell sheets (Costa et al., 2014).[39] Large pore size permitted vascularization of the cell sheets, and periodontal attachment was achieved at the dentin interface. Similarly, Criscenti et al. (2016) converged 3D printed PCL scaffolds and PLGA electrospun nanofibers to develop a triphasic scaffold aimed at mimicking the bone-to-ligament interface.[49] Although the collective results from that study demonstrated that the combination of electrospinning and 3D printing represents a promising approach for the fabrication of scaffolds for the regeneration of periodontal tissue interfaces, multiple techniques are required to fabricate each tissue-specific compartment, thus leading to additional processing steps to integrate them into a single scaffold. In our work, a highly ordered and osteoconductive scaffold that stimulates alveolar bone regeneration while serving as a barrier membrane, thus allowing resident progenitor cells to regenerate new periodontal ligament and cementum when implanted in a well-established periodontal defect model, certainly represents the first step towards the development of personalized scaffolds capable of enabling tissue-specific differentiation of progenitor cells, thus guiding the simultaneous and coordinated regeneration of soft and hard

periodontal tissues. Nonetheless, even though the fenestration defect model utilized herein provides meaningful clinical insight, future *in vivo* studies in larger animal models are necessary to determine both the regenerative and antimicrobial efficacy *in vivo*.

3.3 Conclusions

We believe that this work will contribute to the development of personalized and defect-specific scaffolds for periodontal regeneration capable of enabling the differentiation of resident progenitor cells, and thus guide the coordinated growth of soft and hard periodontal tissues, while affording antimicrobial properties.

3.4 Experimental Section

Materials: Poly(ε-caprolactone) (PCL, Mn:5000) was procured from CELLINK (Göthenburg, Sweden). All other chemical reagents and solutions were purchased from Sigma-Aldrich (St. Louis, MO, USA), unless otherwise noted—sodium hydroxide (NaOH, ≥ 98%), ethanol (99.5%), ethylenediaminetetraacetic acid calcium disodium salt (EDTA-Ca), potassium phosphate (KH_2PO_4, ≥ 99%), and potassium fluoride (KF, ≥ 99.9%). Hexamethyldisilazane (HMDS, ≥ 99%), hexadecylpyridinium chloride monohydrate (CPC), paraformaldehyde (PFA), sodium chloride (NaCl), sodium bicarbonate ($NaHCO_3$), potassium chloride (KCL), potassium phosphate dibasic trihydrate (K_2HPO_4-$3H_20$), magnesium chloride, hexahydrate ($MgCl_2$-6H20), calcium chloride ($CaCl_2$), sodium sulfate (Na_2SO_4), tris-hydroxymethylaminomethane [$(CH_2OH)_3CNH_2$], and hydrochloric acid (HCl) were used as-received without any further purification. Milli-Q deionized water from a Millipore Milli-Q ultrapure water system (MilliporeSigma, Burlington, MA, USA) was used in the experiments. Phosphate-buffered saline (PBS) was procured from GIBCO

Invitrogen (Carlsbad, CA, USA). Meanwhile, a 15% heat-inactivated fetal bovine serum (FBS) solution, alfa-minimum essential medium (α-MEM), and a 1% penicillin–streptomycin solution, was purchased from HyClone (Life Technologies Corporation, Gibco/Brl Division, Grand Island, NY, USA). Also procured were Dispase II (Cat #04942078001, Roche Diagnostics, Indianapolis, IN, USA), collagenase type II (Cat #LS004196, Worthington Biochemical Corp., Lakewood, NJ, USA), and ascorbic acid-2 phosphate (Sigma-Aldrich).

Melt Electrowriting (MEW) and Scaffold Design: PCL is an FDA-approved polymer extensively used to fabricate scaffolds for bone tissue engineering due to its general biocompatibility and well-known degradability pattern *in vivo*.[50] Here, PCL scaffolds were fabricated via melt electrowriting (MEW) using a multi-head bioprinting platform (3DDiscovery, regenHU Ltd., Villaz-St-Pierre, Switzerland) in a biosafety cabinet. The bioprinting system was designed to move on the x, y, and z axes with a printhead moving in the x and z direction and the collector platform moving in the y direction. Specifically, the MEW printhead was supplied with high-voltage power, a pneumatically regulated feeding system, and an electrical heating system to control the temperature of the metal cartridge that housed the polymer (PCL) pellets. The printing path designs were created using BioCAD; a G-code file was generated and loaded to HMI software for printing. In brief, PCL pellets were placed inside the metal cartridge capped with a 26G nozzle, then heated to 90°C for 30 min to allow enough time for the polymer to melt homogeneously. The system's pressure was optimized to 0.07 MPa.[51] The various scaffolds were printed at a feed rate of 40 mm/s and -7 kV of voltage at a distance of 4 mm from the collector. The 0/90°crosshatch design, having 500, 750, and 1000 μm strand spacings, was printed

on top of each other to form scaffolds with 450 layers. The MEW process was conducted at an ambient temperature of 21.5°C and a humidity level of ~ 38.5%. In order to increase the hydrophilicity of PCL, the scaffolds were etched in a 5M NaOH aqueous solution according to a previously reported method.[52] First, the scaffolds were washed with 70% ethanol for 15 min, then they were immersed in the aforementioned NaOH solution at RT for 4 h. After etching, the scaffolds were thoroughly rinsed with deionized (DI) water to neutralize the pH and left to air-dry overnight. Subsequently, the F/CaP coating process was performed using a modified method described elsewhere.[53] In brief, the MEW scaffolds were immersed in a solution that had a mixture of 0.10 M EDTA-Ca, 0.06 M KH_2PO_4, and 0.02 M KF and were incubated under ambient pressure at 37°C for 24 h. Finally, the scaffolds were gently taken out and washed with PBS and left to air-dry overnight. For comparison purposes, 3D printed PCL scaffolds (8×8 mm^2, 0.45-mm thick, and 500 μm strand spacing) were produced via thermal polymer extrusion (TPE). In brief, PCL pellets were heated to 90°C for 30 min, then polymer melt was extruded via a 26G nozzle under pressure of 0.6 MPa and a feed rate of 0.5 mm/s.

Morphological and Chemical Analyses: The morphology of the processed MEW PCL scaffolds (*i.e.*, non-etched, etched with NaOH, and etched with NaOH and F/CaP-coated) was investigated using a scanning electron microscope (SEM, MIRA3, FEG-SEM, TESCAN Brno, Kohoutovice, Czech Republic) equipped with an energy dispersive spectroscopy (EDX, Tescan MIRA3 FEG-EDAX) system to determine the chemical composition of the F/CaP coating. The scaffolds were mounted on Al stubs using double-sided adhesive carbon tape, and then a thin layer of Au was sputter-coated for 60 s (SPI-Module Carbon/Sputter Coater, Thermo Fisher Scientific Inc., West Chester, PA, USA)

prior to SEM imaging. Fibers (n=30) were analyzed in order to calculate their diameter using ImageJ software (National Institutes of Health, Bethesda, MD, USA). Then, a quantitative porosity analysis of the scaffolds was performed.[54,55] In brief, representative SEM images for each scaffold (n=5/group) were imported into the ImageJ software (National Institutes of Health) and processed into 8-bit files. After thresholding, the images were ready for analysis. As a result, the thresholding area represented the scaffold, and the spacing was determined using the command "Analyze → Measure." Atomic force microscopy (AFM) was performed using a TT-AFM equipment (AFM Workshop, Hilton Head Island, SC, USA) in contact mode to investigate the scaffolds (*i.e.,* pristine, non-coated, and F/CaP-coated) in terms of fiber morphology and surface roughness. Qualitative fiber roughness along the fiber long axis was determined from 10 × 10 μm images (n=4/group) using Gwyddion Software (version 2.56, Czech Metrology Institute, Jihlava, Czech Republic). To identify the presence of specific chemical groups on the MEW PCL scaffolds, Fourier-transform infrared spectroscopy (FTIR) was used to determine the effects of etching, as well as the F/CaP coating on the scaffolds and study interactions between the F/CaP coating and the polymer surface. 16 scans with spectra between 600 and 4000 at 4 cm^{-1} resolutions were recorded using an FTIR instrument in the attenuated total reflectance mode (ATR-FTIR, Thermo-Nicolet iS-50, Thermo Fisher Scientific, Inc.). Baseline correction spectra were then centered and normalized for analysis. Meanwhile, the structure and phase composition of the scaffolds were also investigated by X-ray diffraction (XRD, Rigaku Ultima IV diffractometer, Rigaku Americas Corporation, Woodlands, TX, USA) with Cu Kα (λ = 1.54 Å) in Bragg-Brentano geometry. The X-ray source and detector were coupled to scan in a 2-theta (2θ) range from 5° to

45° in a step size of 0.05° at a scan speed of 1°/min. The phase identification was performed using Rigaku's data analysis software (PDXL Version 2.6.1.2) and the Inorganic Crystal Structure Database (ICSD). The thermal properties of F/CaP-coated, non-coated, and pristine MEW PCL scaffolds were examined with differential scanning calorimetry (DSC, Perkin-Elmer DSC-7, Perkinelmer inc., Waltham, MA, USA) and thermal gravimetric analysis (TGA, Perkin-Elmer TGA-7, Perkinelmer inc.). For DSC measurements, the scaffolds were mounted in copper DSC pans, held isothermally at 25°C for 1 min and heated from 25°C to 650 °C. Similarly, for TGA, the samples were heated to 650°C at a rate of 10°C/min and a nitrogen atmosphere. The chemical stability of F/CaP-coated scaffolds was examined post-incubation in distilled water (dH_2O) and simulated body fluid (SBF). F/CaP-coated scaffolds (n=3) were immersed in 10 ml dH_2O at 37°C. After soaking for 1, 3, and 7 days, the release of Ca and P ions was determined using High Resolution Inductively Coupled Plasma Mass Spectrometry (Quadrupole-ICP-MS, Thermo Fisher Scientific, Inc., Waltham, MA, USA). Further, thermal properties and stability of the mineral phase of F/CaP-coated scaffolds after soaking in dH_2O and SBF were examined using thermal gravimetric analysis (TGA), at 3- and 7-days post-incubation. The samples were heated to 600°C at a rate of 10°C/min and a nitrogen atmosphere, and the percentage of residual mass was measured at 550°C.

Biomechanical Properties: The mechanical properties, namely: tensile strength, Young's modulus, and elongation at break of F/CaP-coated, non-coated (NaOH-etched), and pristine PCL (500 µm strand spacings), were assessed by uniaxial tensile testing (expert 5601, ADMET, Inc., Norwood, MA, USA). Rectangular-shaped scaffolds (15 mm × 3 mm × 0.45 mm) were evaluated (n=4/group) at a crosshead speed of 2 mm/min.

Mechanical data of each sample were acquired from the stress-strain curves and reported in MPa.

In Vitro Bioactivity: The *in vitro* bioactivity test was carried out by suspending the distinct scaffolds vertically in a well-established simulated body fluid (SBF) solution prepared according to the method described by Kokubo.[56,57] In brief, 8.035 g NaCl, 0.355 g $NaHCO_3$, 0.255 g KCL, 0.231 g K_2HPO_4-$3H_20$, 0.311 g $MgCl_2$-$6H_20$, 0.292 g $CaCl_2$, and 0.072 g Na_2SO_4 were dissolved in 1L of dH_2O under continuous stirring at 36.5°C and buffered at pH 7.4 with tris-hydroxymethylaminomethane [$(CH_2OH)_3CNH_2$] and 1 M hydrochloric acid (HCl). Then, the SBF was stored at 4°C to be used within 30 days of preparation. Next, F/CaP-coated, non-coated (NaOH-etched), and pristine MEW PCL scaffolds (n=3/group/timepoint) were soaked in 8 mL of SBF under 120 rpm shaking speed at 37°C and retrieved at different time intervals up to 21 days. Non-coated and pristine MEW scaffolds were used as controls. At the end of each time point, the scaffolds were gently taken out and rinsed with DI water, then left to air-dry overnight. Finally, chemo-morphological analyses were carried out by SEM/EDS, FTIR, and XRD (as mentioned above).

Cell Culture: Human periodontal ligament stem cells (hPDLSCs) previously isolated and characterized for ($CD90^+$ and $CD105^+$)[58] were used in the experiments reported herein. Briefly, human periodontal ligament (PDL) tissues were scraped from the middle part of the root surface, then grown on alpha-minimum essential medium (α-MEM). Cells were then collected and centrifuged; the resultant supernatant was removed, and the cells were resuspended in PBS containing 4 mg/mL dispase II and 2 mg/mL collagenase type II for 60 min at 37°C. The solution was inactivated with a mixture of α-

MEM, FBS, and 100 μM ascorbic acid 2 phosphate. The cells were cultured in T-25 flasks and the medium was changed every other day. For purposes of our experiments, hPDLSCs at passage 4 were expanded in α-MEM basal medium supplemented with 15% heat-inactivated FBS and 1% antibiotic/antimycotic solution. hPDLSCs were cultured at 37°C at a 5% CO_2 atmosphere. For the osteogenic differentiation assays, hPDLSCs were cultured in osteogenic differentiation media [OM] (*i.e.*, basal medium supplemented with 50 μg/mL ascorbic acid, 10 mM of β-glycerophosphate, and 10^{-8} M of dexamethasone). hPDLSCs cultured in basal media [BM] were used as the control. Of note, for all cell-related experiments, the MEW PCL scaffolds were disinfected by soaking in 70% ethanol, followed by UV irradiation (30 min on each side).

Cell Proliferation: hPDLSCs at passage 5 were harvested and seeded at a density of 6×10^4 cells per scaffold (8×8 mm^2) in 24-well low attachment plates (Corning Life Sciences, Tewksbury, MA, USA). To determine the role of the F/CaP coating on cell proliferation, alamarBlue assay (Invitrogen, Thermo Fisher Scientific, Inc.) was performed at selected time points over 28 days (n=3/group/time point). In brief, 10% of the alamarBlue assay reagent was mixed with 90% of the media; it was then added to each well and incubated for 3 h at 37°C and 5% CO_2. The dye incorporation was measured at 560 nm (excitation range is 540-570 nm) and an emission of 590 nm (emission range is 580-610 nm); using a fluorescence-based plate reader (SpectraMax iD3, Molecular Devices LLC, San Jose, CA, USA). Finally, each well was washed with PBS and replaced with fresh media.

Cell-scaffold Interaction: Confluent hPDLSCs at passage 5 were harvested and seeded on the MEW PCL scaffolds. Non-coated (NaOH-etched) scaffolds served as the

control. Briefly, using low attachment 24-well tissue culture plates (Corning Life Sciences), 6×10^4 cells/scaffold were seeded and cultured for 1, 3, and 7 days (n=3/group/time point). At each time point, the scaffolds were gently washed in PBS and the cells were fixed in 4% PFA. After 48 h, the scaffolds were first dehydrated in ascending ethanol concentrations (up to 100%), followed by incubation in hexamethyldisilazane (HMDS, Sigma-Aldrich) overnight. Finally, the constructs were mounted on Al stubs using double-sided adhesive carbon tape, and then a thin layer of Au was sputter-coated for 60s (SPI-Module Carbon/Sputter Coater, Thermo Fisher Scientific Inc.) prior to SEM imaging.

Confocal Laser Scanning Microscopy: Attachment and proliferation of hPDLSCs on F/CaP-coated and non-coated (NaOH-etched) MEW PCL scaffolds was assessed by imaging using an upright fluorescence microscope (Carl Zeiss Meditec AG, Jena, Germany) and confocal laser scanning microscopy (CLSM, Eclipse-Ti, Nikon Corporation, Tokyo, Japan). Cell-scaffold constructs were fixed in 4% PFA for 30 min at 4°C, then washed in PBS (3×). hPDLSCs were subsequently permeabilized using 0.1% Triton X-100 solution for 5 min. After PBS (2×) rinsing, the constructs were blocked using 1.5% bovine serum albumin (BSA) in PBS for 30 min and then stained with TRITC-conjugated phalloidin and DAPI (1:1200, MilliporeSigma) for 1h at RT according to the manufacturer's instructions. Finally, the constructs were gently rinsed (3×) in PBS to remove excess phalloidin conjugate and placed on a glass slide for observation under fluorescence and confocal microscopes.

ALP Activity: The ALP activity of hPDLSCs seeded on MEW PCL scaffolds was measured using the colorimetric SensoLyte pNPP ALP kit (AnaSpec Inc., Freemont, CA,

USA), following the manufacturer's recommendations. First, the wells were washed with PBS, then lysed with Triton-X-100. 50-µL supernatant was transferred to a 96-well plate and incubated for 10 min at RT. Then, 50 µL of the pNPP reagent was added to the supernatant and allowed to react for 1 h at 25°C. The absorbance was measured using a microplate reader (Spectra iD3) at 405 nm, followed by calculation of the total ALP activity based on an ALP standard of known concentration and normalized to total protein measured using a BCA protein assay kit (Thermo Fisher Scientific Inc.) (n=3/group/time point).

Alizarin Red Staining: Mineralized nodule formation was measured using Alizarin red staining (ARS, ScienCell Research Laboratories, Inc., Carlsbad, CA, USA). Cell-scaffold constructs were washed (3×) with PBS for 15 min at RT; they were then fixed with 4% PFA. Each well was washed with DI water, then stained with 1 mL of 40 mM ARS for 30 min. Finally, a destaining procedure was performed for 15 min using 10% (w/v) CPC in 10 mM sodium phosphate at pH 7.0. The absorbance was measured at 562 nm using a microplate reader (Spectra I D3) to quantify the ARS concentration (n=3/group/time point).

mRNA Expressions using Real-time PCR: The expression of osteogenic genes, namely: Osteocalcin (OCN, Hs01587814_g1), Runt-related transcription factor 2 (Runx2, Hs01047973_m1), Collagen alpha 1 (Col1A1, Hs00164004_m1), and housekeeping gene Glyceraldehyde 3-phosphate dehydrogenase (GAPDH, Hs02758991_g1), were evaluated by a quantitative polymerase chain reaction (qPCR). Briefly, the cells were harvested, and the total RNA was isolated (Purelink RNA Mini Kit, Invitrogen Corporation. Carlsbad, CA, USA). cDNA synthesis was then performed using iScript RT Supermix

(Bio-Rad Laboratories, Inc., Hercules, CA, USA). The ΔΔCq method was used to measure the relative gene expression from the quantification cycle (Cq) values retrieved by qPCR analysis. Three independent PCR reactions were performed for each sample (n=3/group/time point). qPCR results were normalized to the reference sample.

Antimicrobial Character: Colony-forming units (CFU/mL) were quantified after growing *Porphyromonas gingivalis (P. gingivalis)* ATCC® 33277 on the scaffolds for 48 h. In brief, the MEW PCL (pristine, non-coated, and F/CaP-coated) scaffolds (8×8 mm^2 and 0.45-mm thick) were adapted in CellCrown™ inserts (Scaffdex Ltd., Tampere, Finland), then kept under UV light for 30 min per each side. The set was then placed into wells of a 24-well plate (n=6), and 1 mL of Brain Heart Infusion broth (BHI, Sigma-Aldrich) + vitamin K and Hemin 5% (v/v) solution Hemin (Thermo Fisher Scientific Inc.) containing the *P. gingivalis* cultures, adjusted to an optical density of 1.0 following the McFarland scale, were inoculated on the scaffolds. The plates were anaerobically incubated for 48 h at 37°C. The samples were then carefully removed from the wells with sterile tweezers, gently washed with 0.9% saline solution to remove non-adhered cells, placed into microcentrifuge tubes with 500 µL of sterile saline solution, and vortexed for 30 sec to detach the adhered cells. Saline solution with the bacteria was submitted to serial dilution, and three drops of each dilution were placed in a Brucella sheep blood agar plate (Remel Microbiology Products, Lenexa, KS, USA) with vitamin K and hemin and anaerobically incubated for 48 h at 37°C. Next, the colonies were counted, and the values were recorded and expressed in CFU/mL. To qualitatively assess biofilm inhibition, two samples per group were fixed in 4% PFA. After 48 h, the scaffolds were first dehydrated in ascending ethanol concentrations (up to 100%), followed by incubation in

hexamethyldisilazane (HMDS, Sigma-Aldrich) overnight. Finally, the constructs were mounted on Al stubs using double-sided adhesive carbon tape; then a thin layer of Au was sputter-coated for 120 s prior to SEM imaging.

In Vivo Biocompatibility: All animal procedures were approved by the University of Michigan Institutional Animal Care and Use Committee (IACUC, protocol #PRO00008502). Nine 6-week-old male Fischer 344 rats (300-320 g) were used for the experiments (Envigo RMS, Inc., Oxford, MI, USA). All surgical procedures were performed under general anesthesia induced with isoflurane inhalation (Piramal Critical Care Inc., Bethlehem, PA, USA) (4-5%) and maintained with isoflurane (1-3%). After anesthesia, four subcutaneous pockets (for Sham, and 3 scaffold groups, *i.e.*, thermal polymer extrusion/TPE, non-coated, and F/CaP-coated) were bluntly created through short dorsal skin incisions (10 mm in length), and square-shaped samples (8×8 mm^2 and 0.45-mm thick) of F/CaP-coated and non-coated MEW PCL scaffolds were implanted (n=3/group/time point) per animal. Sham and TPE scaffolds (8×8 mm^2 and 0.45-mm thick) were used as a control. After surgery, the animals were allowed to recover from anesthesia. At 7-, 14-, or 28-days post-implantation, the animals were euthanized using CO_2, and the samples were retrieved together with the surrounding peri-implantation tissue and fixed in 10% buffered formalin prior to further analysis. After fixation, the samples were embedded in paraffin to allow sagittal cut of 6 μm-thick sections of the whole 8×8 mm^2 square samples, including the surrounding tissue, and they were stained with H&E to investigate under light microscopy for the presence of tissue ingrowth, vascularization, and inflammatory cells (Nikon E800, Nikon Corporation).

Periodontal Fenestration Defect Model: All animal procedures were approved by the University of Michigan Institutional Animal Care and Use Committee (IACUC, protocol #PRO00008502). Twelve 6-week-old male Fischer 344 rats (300-320 g) were used for the experiments. All surgical procedures were performed under general anesthesia induced with isoflurane inhalation (Piramal Critical Care Inc.) (4-5%) and maintained with isoflurane (1-3%). After anesthesia, periodontal fenestration defects (3×2×1 mm) were surgically created bilaterally in the rat mandible. Briefly, the alveolar bone, cementum, and other soft tissue structures were removed. Prior to scaffold placement, 20% barium sulfate ($BaSO_4$) was dissolved in distilled water, then the F/CaP-coated and non-coated scaffolds were coated with $BaSO_4$ to obtain the higher intensity and grayscale Hounsfield Unit. The scaffolds (n=4/group/time point) were placed inside the defects and evaluated for their ability to regenerate periodontal tissue after 3 and 6 weeks of healing. At 3- and 6-weeks post-implantation, the constructs were retrieved and fixed in 4% PFA prior to micro-computed tomography and histological analyses.

Micro-computed Tomography (Micro-CT): Newly formed bone at periodontal defect was analyzed using (Scanco μCT 100, Scanco Medical AG, Brüttisellen, Switzerland). The scan parameters were determined as follows: 360° rotation using 70 kV, 114 μA monochromatic x-rays, and 25 μm voxel sizes. An average of 500 ms per frame exposure time was maintained. The Scanco Medical System software was used for 3D image reconstruction. Then the 3D image was used to circumferentially trace to the original defect, which, hereafter, was named as the region of interest (ROI). The ROI of each sample was analyzed to identify bone volume (BV), Bone fill (BF, BV/TV), and tissue mineral density (TMD).

Histological Analysis: After the micro-CT scans, the mandibles were decalcified in EDTA for 8 weeks. The decalcified specimens were dehydrated in an ascending alcohol series, then embedded with paraffin prior to cutting into 4-μm sections. The sections were either stained with Hematoxylin and Eosin (H&E) or Masson's trichrome (MT) to identify cellular reaction and mineralized bone formation. After staining, the samples were followed by microscopic imaging using a light microscope equipped with a digital camera (Nikon E800, Nikon Corporation).

Statistics: Data are presented as Mean±SD unless otherwise noted. Group comparisons were performed using one-way or two-way ANOVA followed by pairwise Sidak multiple comparison post-hoc tests after verifying model assumptions. A two-sided 5% significance level was used for all tests. Statistical analyses were performed using SAS version 9.4 (SAS Institute, Inc., Cary, NC, USA). Microbial colony counts are presented as $\log_{10}$(CFU/mL).

Author Contributions

Arwa Daghrery performed material, biological and animal experiments including scaffolds fabrication, characterization, cell culture, molecular and biochemical studies, periodontal fenestration animal surgeries and histological analysis. Jessica A. Ferreira assisted with animal surgeries, micro-CT analysis and histology. Isaac J. de Souza Araujo performed and analyzed the bacteria experiments. George Eckert performed all statistical analyses. Brian Clarkson and Sywe-Ren Chang provided insight with F/CaP coating protocol. Jos Malda and Sarit Bhaduri critically revised the manuscript. MCB supervised, designed, revised, and finalized the manuscript, and is the corresponding author.

Conflict of Interest

The authors declare no competing financial interest.

Acknowledgements

M.C.B. acknowledges the National Institutes of Health (NIH – National Institute of Dental and Craniofacial Research, grants K08DE023552 and R01DE026578), the OsteoScience Foundation (Peter Geistlich Research Award), the International Association for Dental Research (IADR-GSK Innovation in Oral Care Award), and the American Academy of Implant Dentistry Foundation (AAIDF). The authors are indebted to Sywe-Ren Chang for his assistance with the coating experiments and for sharing his knowledge. The content is solely the responsibility of the authors and does not necessarily represent the official views of the National Institutes of Health.

3.5 References

(1) Eke, P. I.; Dye, B. A.; Wei, L.; Slade, G. D.; Thornton-Evans, G. O.; Borgnakke, W. S.; Taylor, G. W.; Page, R. C.; Beck, J. D.; Genco, R. J. Update on Prevalence of Periodontitis in Adults in the United States: NHANES 2009 – 2012. *J Periodontol* **2015**, *86* (5), 611–622.

(2) Bottino, M. C.; Thomas, V.; Schmidt, G.; Vohra, Y. K.; Chu, T.-M. G.; Kowolik, M. J.; Janowski, G. M. Recent Advances in the Development of GTR/GBR Membranes for Periodontal Regeneration—A Materials Perspective. *Dental Materials* **2012**, *28* (7), 703–721.

(3) Hasani-Sadrabadi, M. M.; Sarrion, P.; Nakatsuka, N.; Young, T. D.; Taghdiri, N.; Ansari, S.; Aghaloo, T.; Li, S.; Khademhosseini, A.; Weiss, P. S.; Moshaverinia, A. Hierarchically Patterned Polydopamine-Containing Membranes for Periodontal Tissue Engineering. *ACS Nano* **2019**, *13* (4), 3830–3838.

(4) Tan, J.; Zhang, M.; Hai, Z.; Wu, C.; Lin, J.; Kuang, W.; Tang, H.; Huang, Y.; Chen, X.; Liang, G. Sustained Release of Two Bioactive Factors from Supramolecular Hydrogel Promotes Periodontal Bone Regeneration. *ACS Nano* **2019**, *13* (5), 5616–5622.

(5) Blakeney, B. A.; Tambralli, A.; Anderson, J. M.; Andukuri, A.; Lim, D.-J.; Dean, D. R.; Jun, H.-W. Cell Infiltration and Growth in a Low Density, Uncompressed Three-Dimensional Electrospun Nanofibrous Scaffold. *Biomaterials* **2011**, *32* (6), 1583–1590.

(6) Rasperini, G.; Pilipchuk, S. P.; Flanagan, C. L.; Park, C. H.; Pagni, G.; Hollister, S. J.; Giannobile, W. V. 3D-Printed Bioresorbable Scaffold for Periodontal Repair: *Journal of Dental Research* **2015**.

(7) Abbasi, N.; Hamlet, S.; Dau, V. T.; Nguyen, N.-T. Calcium Phosphate Stability on Melt Electrowritten PCL Scaffolds. *Journal of Science: Advanced Materials and Devices* **2020**, *5* (1), 30–39.

(8) Liu, J.; Jin, T.; Chang, S.; Czajka-Jakubowska, A.; Zhang, Z.; Nör, J. E.; Clarkson, B. H. The Effect of Novel Fluorapatite Surfaces on Osteoblast-Like Cell Adhesion, Growth, and Mineralization. *Tissue Eng Part A* **2010**, *16* (9), 2977–2986.

(9) Sikder, P.; Ren, Y.; Bhaduri, S. B. Synthesis and Evaluation of Protective Poly(Lactic Acid) and Fluorine-Doped Hydroxyapatite–Based Composite Coatings on AZ31 Magnesium Alloy. *Journal of Materials Research* **2019**, *34* (22), 3766–3776.

(10) Little, U.; Buchanan, F.; Harkin-Jones, E.; Graham, B.; Fox, B.; Boyd, A.; Meenan, B.; Dickson, G. Surface Modification of Poly(ε-Caprolactone) Using a Dielectric Barrier Discharge in Atmospheric Pressure Glow Discharge Mode. *Acta Biomaterialia* **2009**, *5* (6), 2025–2032.

(11) Abbasi, N.; Abdal-hay, A.; Hamlet, S.; Graham, E.; Ivanovski, S. Effects of Gradient and Offset Architectures on the Mechanical and Biological Properties of 3-D Melt Electrowritten (MEW) Scaffolds. *ACS Biomater. Sci. Eng.* **2019**, *5* (7), 3448–3461.

(12) Abbasi, N.; Ivanovski, S.; Gulati, K.; Love, R. M.; Hamlet, S. Role of Offset and Gradient Architectures of 3-D Melt Electrowritten Scaffold on Differentiation and Mineralization of Osteoblasts. *Biomaterials Research* **2020**, *24* (1), 2.

(13) Shi, H.; Zong, W.; Xu, X.; Chen, J. Improved Biphasic Calcium Phosphate Combined with Periodontal Ligament Stem Cells May Serve as a Promising Method for Periodontal Regeneration. *Am J Transl Res* **2018**, *10* (12), 4030–4041.

(14) Babaie, E.; Bhaduri, S. B. Fabrication Aspects of Porous Biomaterials in Orthopedic Applications: A Review. *ACS Biomater. Sci. Eng.* **2018**, *4* (1), 1–39.

(15) Fernandez, J. M.; Molinuevo, M. S.; Cortizo, M. S.; Cortizo, A. M. Development of an Osteoconductive PCL–PDIPF–Hydroxyapatite Composite Scaffold for Bone Tissue Engineering. *Journal of Tissue Engineering and Regenerative Medicine* **2011**, *5* (6), e126–e135.

(16) Oyane, A.; Uchida, M.; Choong, C.; Triffitt, J.; Jones, J.; Ito, A. Simple Surface Modification of Poly(ε-Caprolactone) for Apatite Deposition from Simulated Body Fluid. *Biomaterials* **2005**, *26* (15), 2407–2413.

(17) Zadpoor, A. A. Relationship between in Vitro Apatite-Forming Ability Measured Using Simulated Body Fluid and in Vivo Bioactivity of Biomaterials. *Materials Science and Engineering: C* **2014**, *35*, 134–143.

(18) Verisqa, F.; Triaminingsih, S.; Corputty, J. E. M. Composition of Chitosan-Hydroxyapatite-Collagen Composite Scaffold Evaluation after Simulated Body Fluid Immersion as Reconstruction Material. **2017**, *884*, 012035.

(19) Ibsen, C. J. S.; Chernyshov, D.; Birkedal, H. Apatite Formation from Amorphous Calcium Phosphate and Mixed Amorphous Calcium Phosphate/Amorphous Calcium Carbonate. *Chemistry – A European Journal* **2016**, *22* (35), 12347–12357.

(20) Münchow, E. A.; Albuquerque, M. T. P.; Zero, B.; Kamocki, K.; Piva, E.; Gregory, R. L.; Bottino, M. C. Development and Characterization of Novel ZnO-Loaded Electrospun Membranes for Periodontal Regeneration. *Dent Mater* **2015**, *31* (9), 1038–1051.

(21) Bužarovska, A. Preparation and Characterization of Poly(ε-Caprolactone)/ZnO Foams for Tissue Engineering Applications. *J Mater Sci* **2017**, *52* (20), 12067–12078.

(22) Montazeri, N.; Jahandideh, R.; Biazar, E. Synthesis of Fluorapatite–Hydroxyapatite Nanoparticles and Toxicity Investigations. *Int J Nanomedicine* **2011**, *6*, 197–201.

(23) Bennett, B. T.; Beck, J. P.; Papangkorn, K.; Colombo, J. S.; Bachus, K. N.; Agarwal, J.; Shieh, J. F.; Jeyapalina, S. Characterization and Evaluation of Fluoridated Apatites for the Development of Infection-Free Percutaneous Devices. *Materials Science and Engineering: C* **2019**, *100*, 665–675.

(24) Hashmi, M. U.; Shah, S. A. Dissolution Behavior of Bioactive Glass Ceramics with Different CaO/MgO Ratios in SBF-K9 and r-SBF. *Progress in Natural Science: Materials International* **2014**, *24* (4), 354–363.

(25) Jang, H. L.; Zheng, G. B.; Park, J.; Kim, H. D.; Baek, H.-R.; Lee, H. K.; Lee, K.; Han, H. N.; Lee, C.-K.; Hwang, N. S.; Lee, J. H.; Nam, K. T. In Vitro and In Vivo Evaluation of Whitlockite Biocompatibility: Comparative Study with Hydroxyapatite and β-Tricalcium Phosphate. *Advanced Healthcare Materials* **2016**, *5* (1), 128–136.

(26) Ogose, A.; Hotta, T.; Kawashima, H.; Kondo, N.; Gu, W.; Kamura, T.; Endo, N. Comparison of Hydroxyapatite and Beta Tricalcium Phosphate as Bone Substitutes after Excision of Bone Tumors. *Journal of Biomedical Materials Research Part B: Applied Biomaterials* **2005**, *72B* (1), 94–101.

(27) Kim, J.-W.; Shin, K.-H.; Koh, Y.-H.; Hah, M. J.; Moon, J.; Kim, H.-E. Production of Poly(ε-Caprolactone)/Hydroxyapatite Composite Scaffolds with a Tailored Macro/Micro-Porous Structure, High Mechanical Properties, and Excellent Bioactivity. *Materials (Basel)* **2017**, *10* (10).

(28) Chouzouri, G.; Xanthos, M. In Vitro Bioactivity and Degradation of Polycaprolactone Composites Containing Silicate Fillers. *Acta Biomaterialia* **2007**, *3* (5), 745–756.

(29) Eliaz, N.; Metoki-Shlubsky, N. Calcium Phosphate Bioceramics: A Review of Their History, Structure, Properties, Coating Technologies and Biomedical Applications. *Materials* **2017**, *10*.

(30) Tamimi, F.; Sheikh, Z.; Barralet, J. Dicalcium Phosphate Cements: Brushite and Monetite. *Acta Biomaterialia* **2012**, *8* (2), 474–487.

(31) Hogrebe, N. J.; Reinhardt, J. W.; Gooch, K. J. Biomaterial Microarchitecture: A Potent Regulator of Individual Cell Behavior and Multicellular Organization. *J Biomed Mater Res A* **2017**, *105* (2), 640–661.

(32) Daghrery, A.; Aytac, Z.; Dubey, N.; Mei, L.; Schwendeman, A.; Bottino, M. C. Electrospinning of Dexamethasone/Cyclodextrin Inclusion Complex Polymer Fibers for Dental Pulp Therapy. *Colloids and Surfaces B: Biointerfaces* **2020**, 111011.

(33) Vaquette, C.; Ivanovski, S.; Hamlet, S. M.; Hutmacher, D. W. Effect of Culture Conditions and Calcium Phosphate Coating on Ectopic Bone Formation. *Biomaterials* **2013**, *34* (22), 5538–5551.

(34) Ge, X.; Leng, Y.; Bao, C.; Xu, S. L.; Wang, R.; Ren, F. Antibacterial Coatings of Fluoridated Hydroxyapatite for Percutaneous Implants. *Journal of Biomedical Materials Research Part A* **2010**, *95A* (2), 588–599.

(35) Kargar, M.; Chang, Y.-R.; Khalili Hoseinabad, H.; Pruden, A.; Ducker, W. A. Colloidal Crystals Delay Formation of Early Stage Bacterial Biofilms. *ACS Biomater. Sci. Eng.* **2016**, *2* (6), 1039–1048.

(36) Kelleher, S. M.; Habimana, O.; Lawler, J.; O' Reilly, B.; Daniels, S.; Casey, E.; Cowley, A. Cicada Wing Surface Topography: An Investigation into the Bactericidal Properties of Nanostructural Features. *ACS Appl. Mater. Interfaces* **2016**, *8* (24), 14966–14974.

(37) Manabe, K.; Nishizawa, S.; Shiratori, S. Porous Surface Structure Fabricated by Breath Figures That Suppresses Pseudomonas Aeruginosa Biofilm Formation. *ACS Appl. Mater. Interfaces* **2013**, *5* (22), 11900–11905.

(38) Abrigo, M.; Kingshott, P.; McArthur, S. L. Electrospun Polystyrene Fiber Diameter Influencing Bacterial Attachment, Proliferation, and Growth. *ACS Appl. Mater. Interfaces* **2015**, *7* (14), 7644–7652.

(39) Perera-Costa, D.; Bruque, J. M.; González-Martín, M. L.; Gómez-García, A. C.; Vadillo-Rodríguez, V. Studying the Influence of Surface Topography on Bacterial Adhesion Using Spatially Organized Microtopographic Surface Patterns. *Langmuir* **2014**, *30* (16), 4633–4641.

(40) Renner, L. D.; Weibel, D. B. Physicochemical Regulation of Biofilm Formation. *MRS Bull* **2011**, *36* (5), 347–355.

(41) Gristina, A. G.; Naylor, P.; Myrvik, Q. Infections from Biomaterials and Implants: A Race for the Surface. *Med Prog Technol* **1988**, *14* (3–4), 205–224.

(42) Jeyachandran, Y. L.; Narayandass, Sa. K.; Mangalaraj, D.; Bao, C. Y.; Li, W.; Liao, Y. M.; Zhang, C. L.; Xiao, L. Y.; Chen, W. C. A Study on Bacterial Attachment on Titanium and Hydroxyapatite Based Films. *Surface and Coatings Technology* **2006**, *201* (6), 3462–3474.

(43) Aguirre, A.; González, A.; Navarro, M.; Castaño, O.; Planell, J. A.; Engel, E. Control of Microenvironmental Cues with a Smart Biomaterial Composite Promotes Endothelial Progenitor Cell Angiogenesis. *Eur Cell Mater* **2012**, *24*, 90–106; discussion 106.

(44) Barbeck, M.; Serra, T.; Booms, P.; Stojanovic, S.; Najman, S.; Engel, E.; Sader, R.; Kirkpatrick, C. J.; Navarro, M.; Ghanaati, S. Analysis of the in Vitro Degradation and the in Vivo Tissue Response to Bi-Layered 3D-Printed Scaffolds Combining PLA and Biphasic PLA/Bioglass Components – Guidance of the Inflammatory Response as Basis for Osteochondral Regeneration. *Bioactive Materials* **2017**, *2* (4), 208–223.

(45) Dan, H.; Vaquette, C.; Fisher, A. G.; Hamlet, S. M.; Xiao, Y.; Hutmacher, D. W.; Ivanovski, S. The Influence of Cellular Source on Periodontal Regeneration Using Calcium Phosphate Coated Polycaprolactone Scaffold Supported Cell Sheets. *Biomaterials* **2014**, *35* (1), 113–122.

(46) Pellegrini, G.; Seol, Y. J.; Gruber, R.; Giannobile, W. Pre-Clinical Models for Oral and Periodontal Reconstructive Therapies. *Journal of dental research* **2009**, *88*, 1065–1076.

(47) Rios, H. F.; Giannobile, W. V. Preclinical Protocols for Periodontal Regeneration. 26.

(48) Ivanovski, S.; Vaquette, C.; Gronthos, S.; Hutmacher, D. W.; Bartold, P. M. Multiphasic Scaffolds for Periodontal Tissue Engineering. *J Dent Res* **2014**, *93* (12), 1212–1221.

(49) Criscenti, G.; Longoni, A.; Luca, A. D.; Maria, C. D.; Blitterswijk, C. A. van; Vozzi, G.; Moroni, L. Triphasic Scaffolds for the Regeneration of the Bone–Ligament Interface. *Biofabrication* **2016**, *8* (1), 015009.

(50) Carter, S.-S. D.; Costa, P. F.; Vaquette, C.; Ivanovski, S.; Hutmacher, D. W.; Malda, J. Additive Biomanufacturing: An Advanced Approach for Periodontal Tissue Regeneration. *Ann Biomed Eng* **2017**, *45* (1), 12–22.

(51) Dubey, N.; Ferreira, J. A.; Daghrery, A.; Aytac, Z.; Malda, J.; Bhaduri, S. B.; Bottino, M. C. Highly Tunable Bioactive Fiber-Reinforced Hydrogel for Guided Bone Regeneration. *Acta Biomaterialia* **2020**.

(52) Visser, J.; Melchels, F. P. W.; Jeon, J. E.; van Bussel, E. M.; Kimpton, L. S.; Byrne, H. M.; Dhert, W. J. A.; Dalton, P. D.; Hutmacher, D. W.; Malda, J. Reinforcement of Hydrogels Using Three-Dimensionally Printed Microfibres. *Nature Communications* **2015**, *6* (1), 1–10.

(53) Guo, T.; Li, Y.; Cao, G.; Zhang, Z.; Chang, S.; Czajka-Jakubowska, A.; Nör, J. E.; Clarkson, B. H.; Liu, J. Fluorapatite-Modified Scaffold on Dental Pulp Stem Cell Mineralization. *J Dent Res* **2014**, *93* (12), 1290–1295.

(54) Grove, C.; Jerram, D. A. JPOR: An ImageJ Macro to Quantify Total Optical Porosity from Blue-Stained Thin Sections. *Computers & Geosciences* **2011**, *37* (11), 1850–1859.

(55) Liu, H.; Du, Y.; St-Pierre, J.-P.; Bergholt, M. S.; Autefage, H.; Wang, J.; Cai, M.; Yang, G.; Stevens, M. M.; Zhang, S. Bioenergetic-Active Materials Enhance Tissue Regeneration by Modulating Cellular Metabolic State. *Sci Adv* **2020**, *6* (13), eaay7608.

(56) Kokubo, T.; Takadama, H. Simulated Body Fluid (SBF) as a Standard Tool to Test the Bioactivity of Implants. In *Handbook of Biomineralization*; Wiley-VCH Verlag GmbH, 2007; pp 97–109.

(57) Ji, L.; Wang, W.; Jin, D.; Zhou, S.; Song, X. In Vitro Bioactivity and Mechanical Properties of Bioactive Glass Nanoparticles/Polycaprolactone Composites. *Mater Sci Eng C Mater Biol Appl* **2015**, *46*, 1–9.

(58) Yeasmin, S.; Ceccarelli, J.; Vigen, M.; Carrion, B.; Putnam, A. J.; Tarle, S. A.; Kaigler, D. Stem Cells Derived from Tooth Periodontal Ligament Enhance Functional Angiogenesis by Endothelial Cells. *Tissue Eng Part A* **2014**, *20* (7–8), 1188–1196.

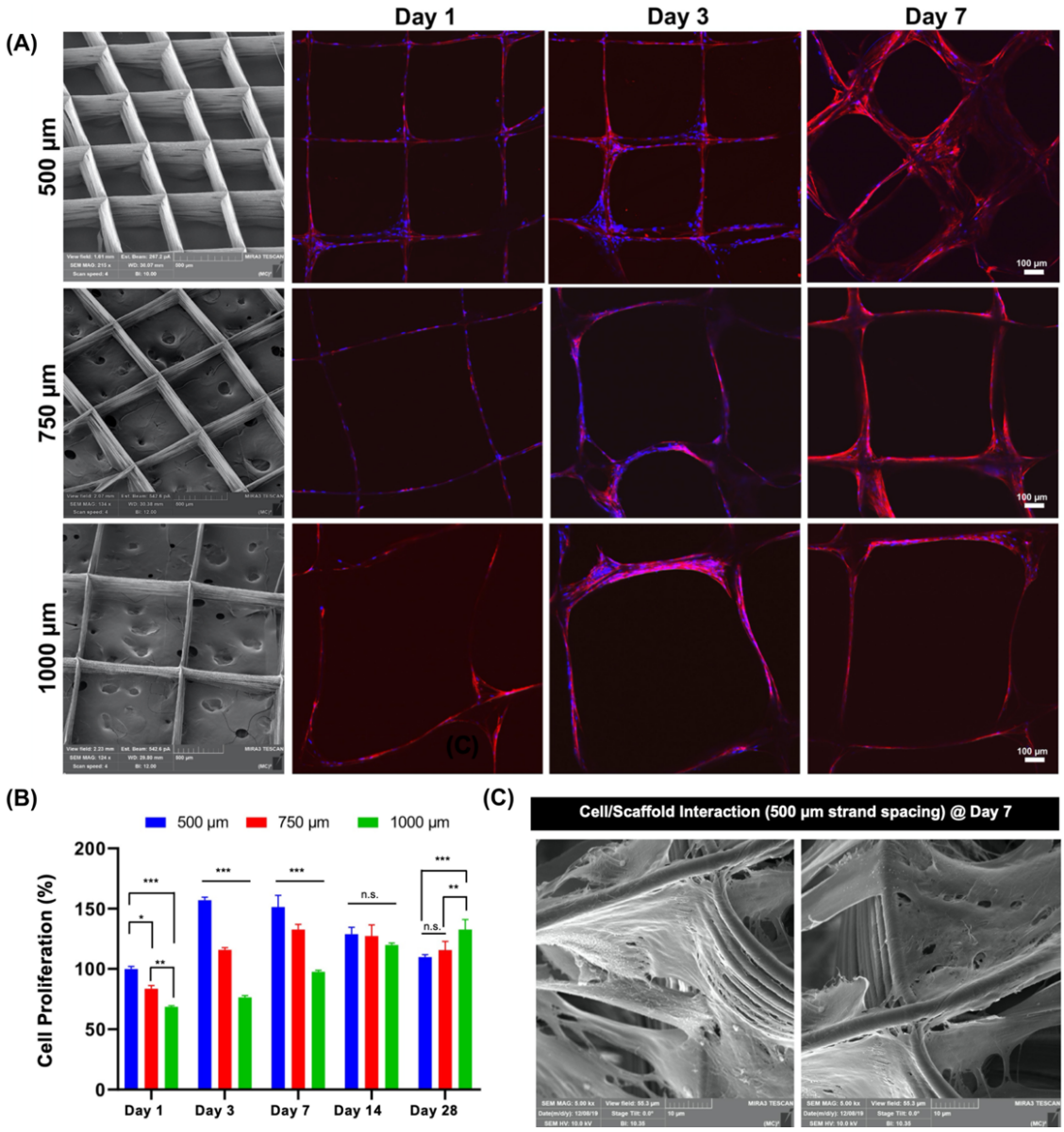

Figure 3-1 Effects of strand spacing on the attachment and proliferation of hPDLSCs.

(a) Representative SEM images of the various MEW PCL scaffolds show well-aligned and defect-free fiber morphology, and distinct strand spacings (500, 750, and 1000 µm) at 0-90°-oriented junctions. Confocal microscopy images of hPDLSCs seeded on the scaffolds after 1, 3, and 7 days of culture. Of note, hPDLSCs show more prominent attachment and proliferation on PCL scaffolds with a 500 µm strand spacing. DAPI (blue) and phalloidin (red) fluorescent staining (scale bar = 100 µm). (b) hPDLSCs' proliferation on MEW scaffolds measured using alamarBlue assay over 28 days of culture. Mean±SD (n=3). ANOVA: ***p<.001, **p<.01, *p<.05. (c) SEM images of hPDLSCs on MEW PCL scaffold at 7 days.

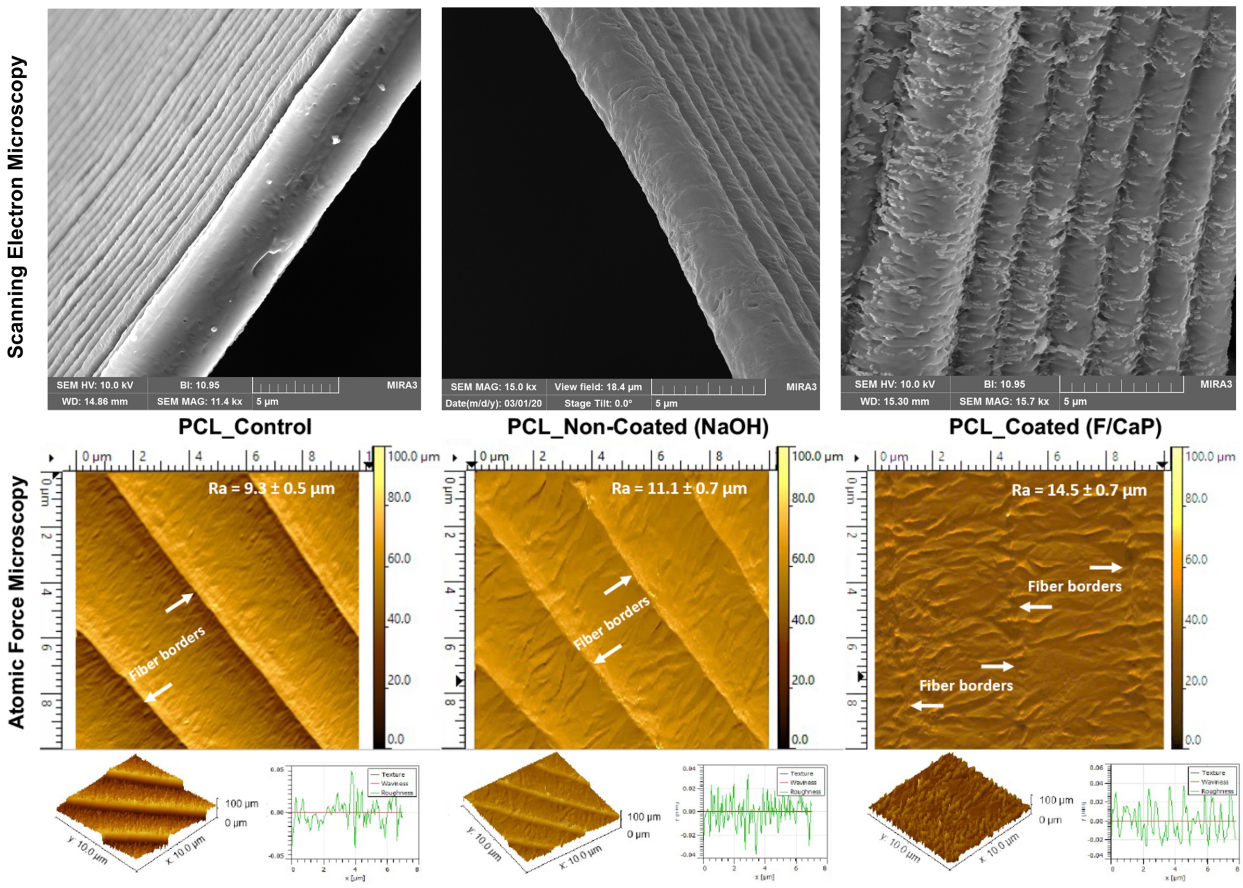

Figure 3-2 Representative SEM (top) and AFM (bottom) images of the MEW scaffolds show distinct surface texture: control (non-etched), NaOH-etched, and F/CaP-coated scaffolds.

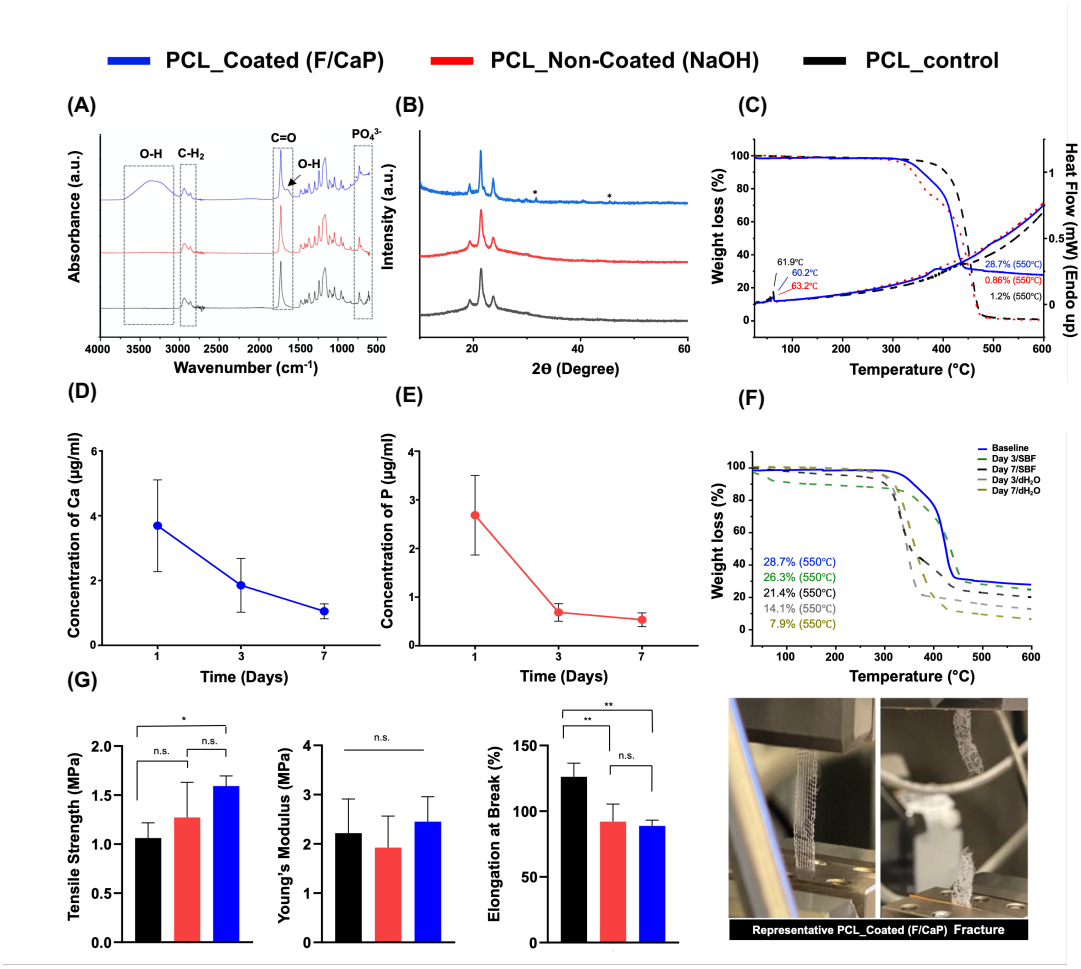

Figure 3-3 Chemical and mechanical analyses of pristine, NaOH-etched, and F/CaP-coated scaffolds

(a) FTIR data show the chemical functional groups related to phosphate ~ 565 cm^{-1} and ~ 960 cm^{-1} in F/CaP-coated scaffolds, confirming successful chemical modification. (*) indicates the presence of OH-F trace. (b) XRD data show peaks similar to pristine PCL and weak peaks appearing at ca. 25.9° and 31.8°; these weak peaks can be attributed to the presence of weak crystalline structure. (c) The TGA-DSC curves of pristine (non-etched), NaOH-etched, and F/CaP-coated scaffolds, (d-e) Ions' release from F/CaP-coated scaffolds were measured in supernatants by means of ICP-MS, (d) Ca ion concentration and (e) P ion concentration in 10 ml dH_2O for time periods ranging from day 1 to 7. (f) Residual mass of the mineral phase after weight loss measured using TGA, after incubation in dH_2O and SBF for time periods ranging from day 3 to 7. (g) Uni-axial tensile testing setup showing a MEW PCL scaffold (500 *µ*m strand spacing) prior to and after testing. Tensile strength, in MPa; Young's modulus, in MPa; and elongation at break, in %. Overall, F/CaP-coated scaffolds show enhanced tensile strength and Young's *modulus compared to their non-coated and pristine counterparts. Mean±SD (n=4). ANOVA: ***p<.001, **p<.01, *p<.05*

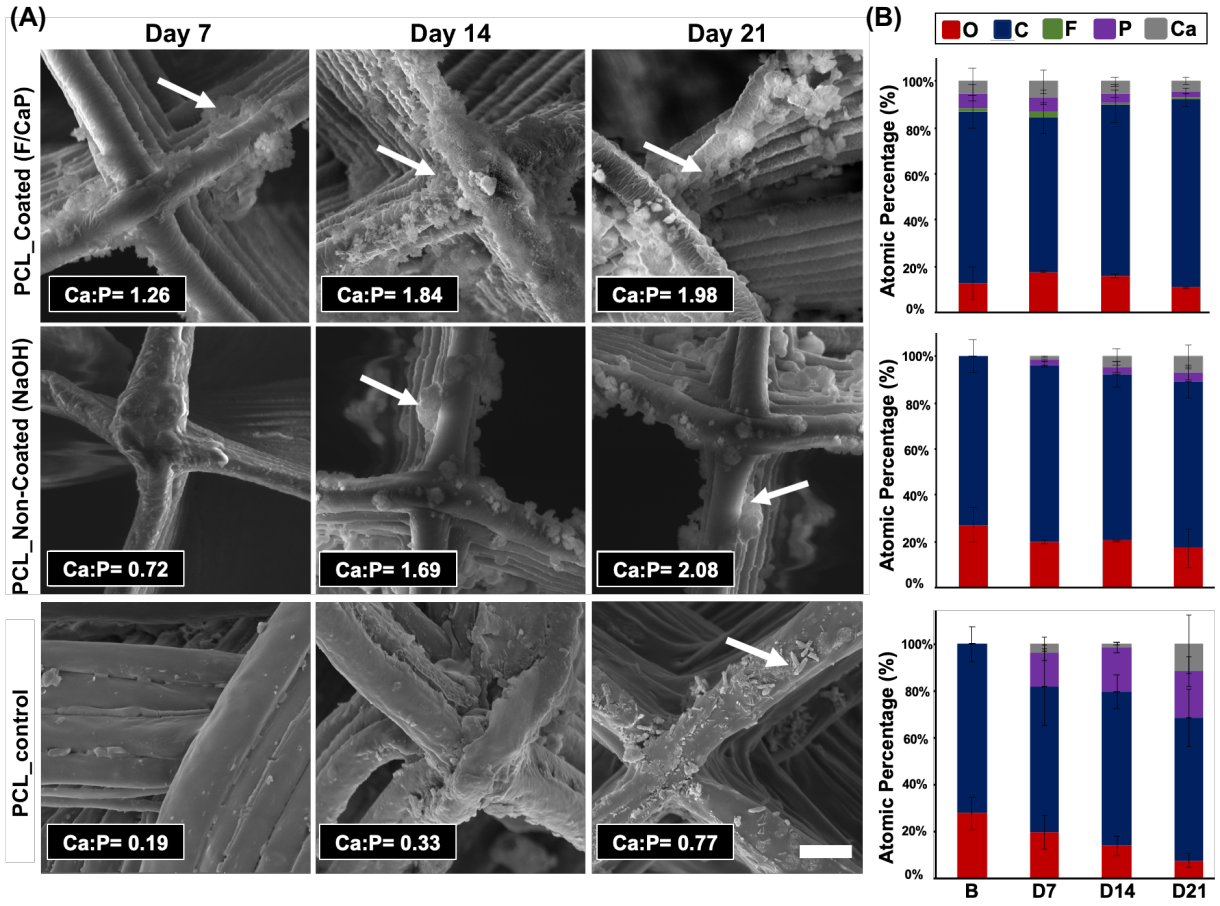

Figure 3-4 Morphological and chemical (elemental) analyses of MEW PCL scaffolds after SBF immersion

(a) Representative SEM images and EDS semi-quantitative chemical analyses of F/CaP-coated, non-coated, and pristine scaffolds immersed in SBF at 37°C for 7, 14, and 21 days. The red arrows indicate apatite formation. (b) Atomic wt.% of crystals deposited on surfaces of all groups (Carbon (blue), Oxygen (red), Calcium (grey), Phosphorous (purple), Fluorine (green).

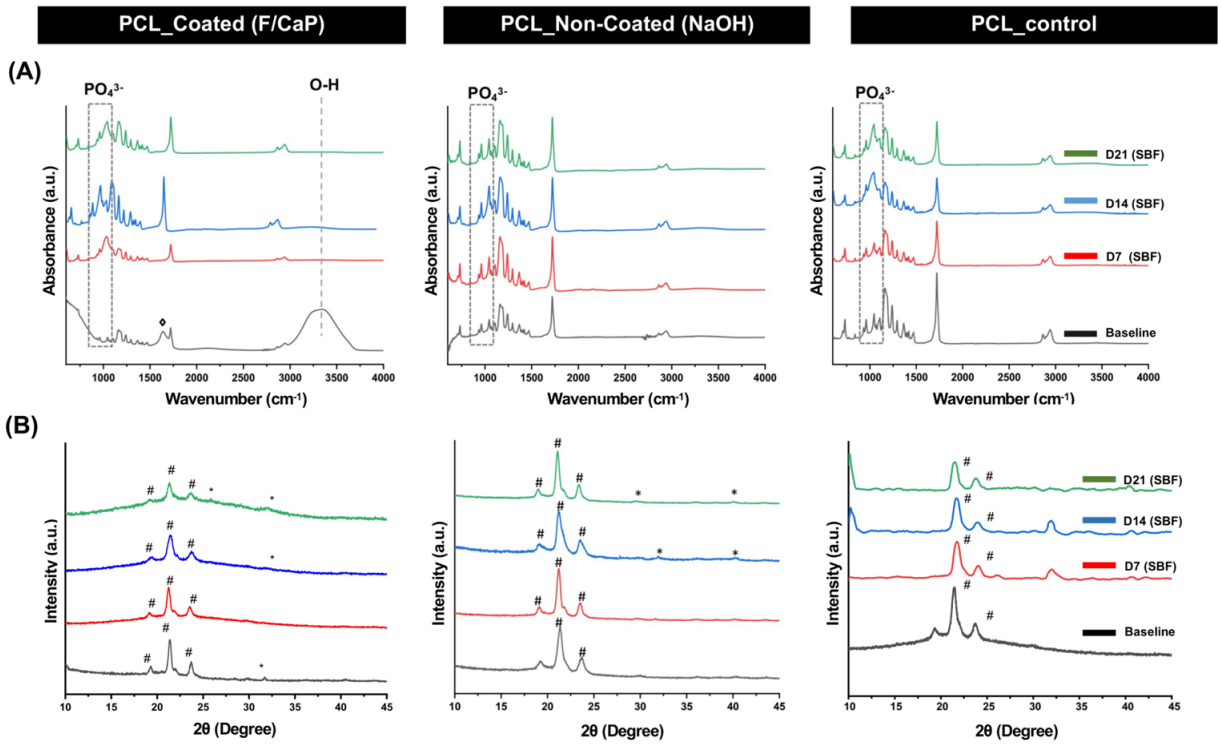

Figure 3-5 Chemical analyses of the F/CaP-coated, non-coated (NaOH-etched), and pristine scaffolds after SBF immersion

(a) FTIR data show the chemical functional groups related to apatite formation on the surface of the fibers of the distinct scaffolds. (b) XRD data reveal peaks associated with apatite after SBF immersion for F/CaP-coated, non-coated (NaOH-etched), and pristine scaffolds. (# PCL, * apatite, and ◊ carbonated apatite).

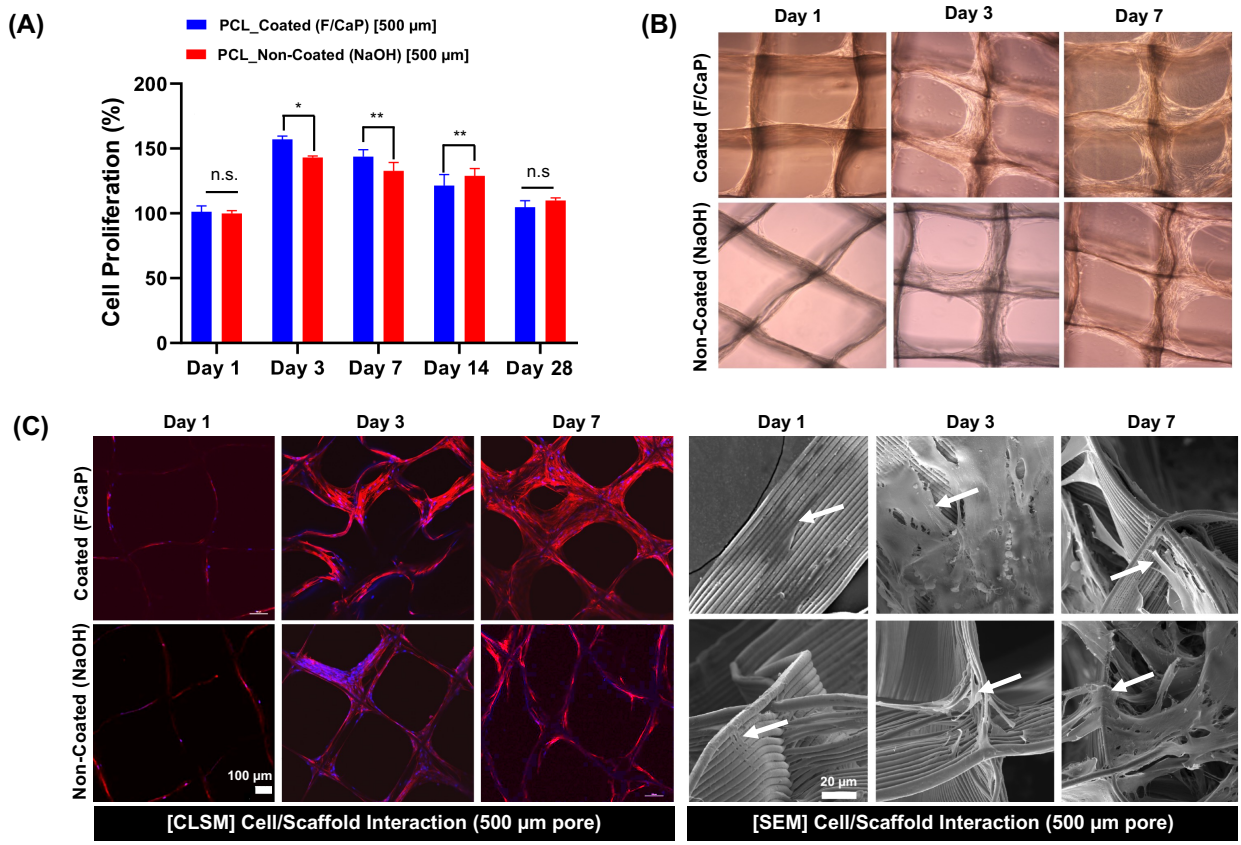

Figure 3-6 Attachment and proliferation of hPDLSCs on MEW PCL scaffolds
(a) Cell proliferation on F/CaP-coated and non-coated scaffolds (500 µm strand spacing) using alamarBlue assay over 28 days. Mean±SD (n=3). ANOVA: ***p<.001, **p<.01, *p<.05. (b) Optical microscopy images of F/CaP-coated and non-coated scaffolds during *in vitro* culture, indicating a gradual enhanced proliferation. (c) Confocal microscopy images show significant cell bridging in 500 µm F/CaP-coated scaffolds at day 7. DAPI (blue) and phalloidin (red) fluorescent staining of hPDLSCs seeded on MEW PCL scaffolds (scale bar = 100 µm) and representative SEM images of hPDLSCs proliferation on F/CaP-coated and non-coated scaffolds after 7 days. Note the characteristic cell spreading along the fibrous walls of the scaffolds. A more pronounced spreading was detected along the nanostructured F/CaP-coated scaffolds (white arrows indicate important filopodia protrusion along and around the fibers).

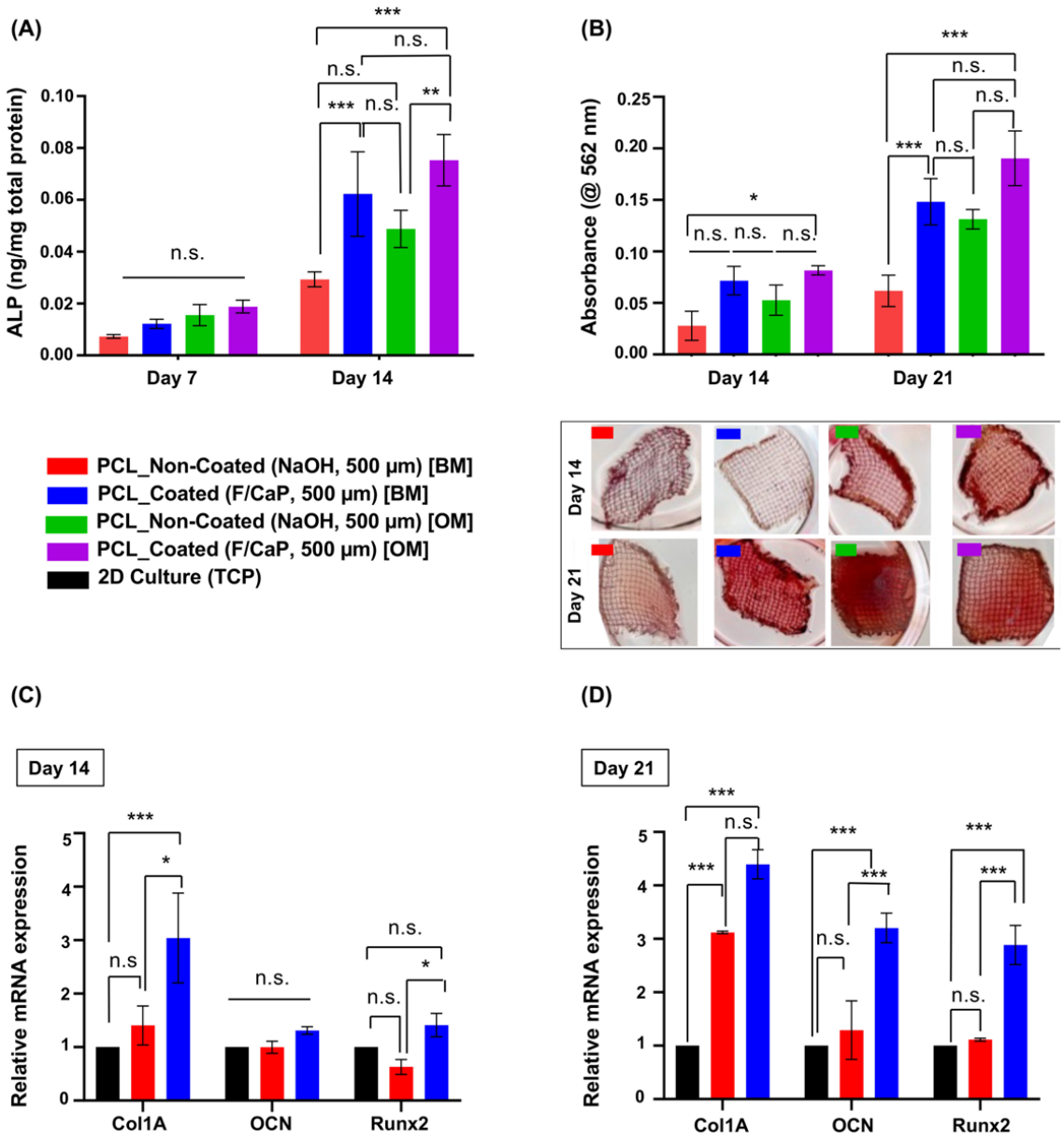

Figure 3-7 Osteogenic differentiation by means of alkaline phosphatase (ALP) activity, quantification of mineralized nodule formation using Alizarin red staining (ARS), and gene expression of osteogenic markers

(a) ALP activity after 7 and 14 days for hPDLSCs seeded on F/CaP-coated scaffolds were significantly higher than non-coated scaffolds in basal (BM) and osteogenic (OM) culturing conditions. (b) ARS quantification and optical images of hPDLSCs seeded on F/CaP-coated, scaffolds in both BM and OM were significantly higher than non-coated (500 µm strand spacing) scaffolds after 14 and 21 days. (c-d) The mRNA levels on day 14 and day 21 of selected osteogenic markers were significantly higher in the F/CaP-coated scaffolds than those in their non-coated counterparts. Mean±SD (n=3). ANOVA: ***p<.001, **p<.01, *p<.05.

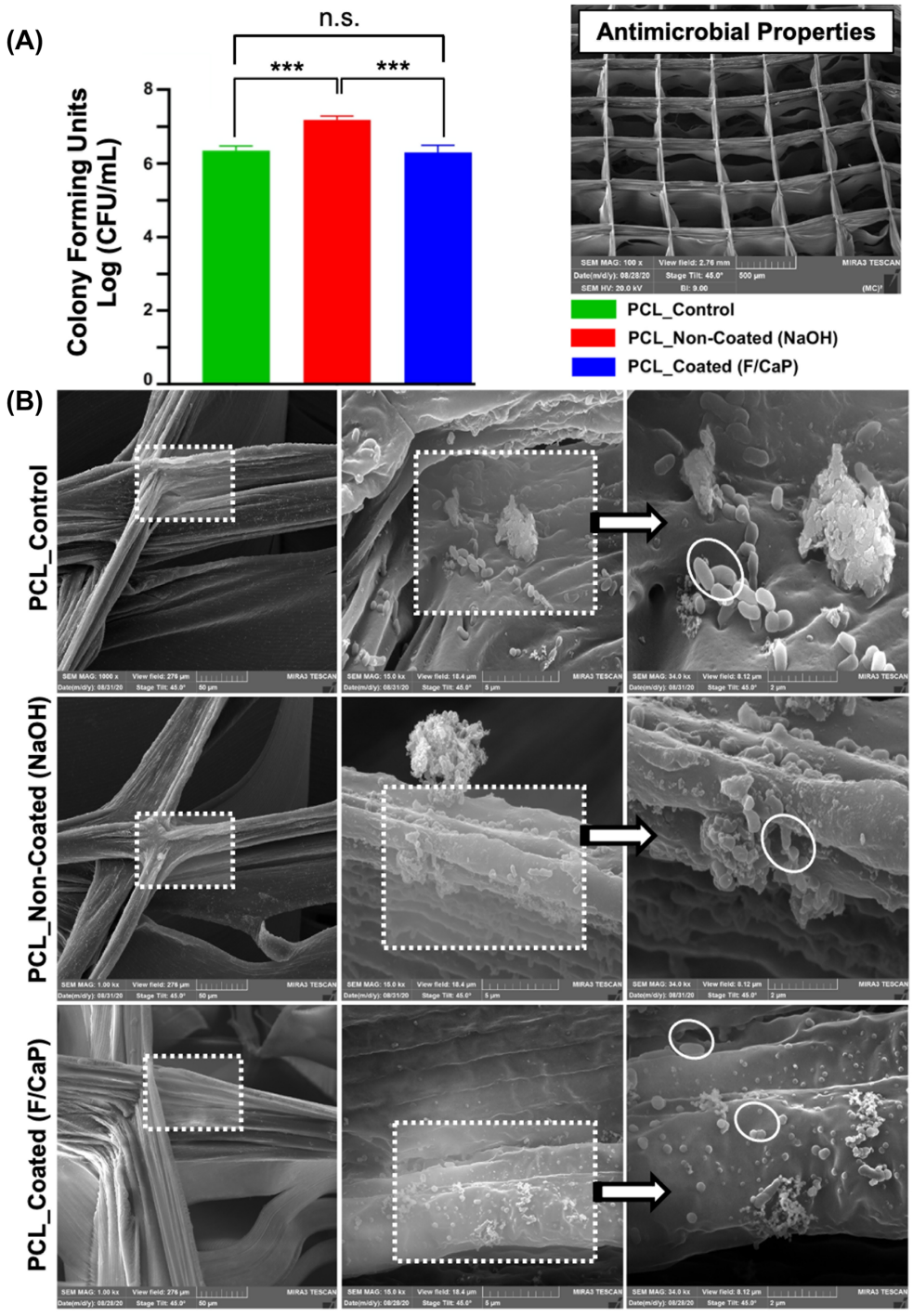

Figure 3-8 Colony-forming units in broths of Gram-negative bacteria, P. gingivalis grown on pristine PCL, non-coated, and F/CaP-coated scaffolds
(a) Colony forming unit graph, Mean±SD (n=6). ANOVA: ***p<.001, **p<.01, *p<.05. **(b)** Representative SEM images of 2-days *P. gingivalis* biofilm formation, demonstrates that bacteria attach to the scaffolds' surface of different groups.

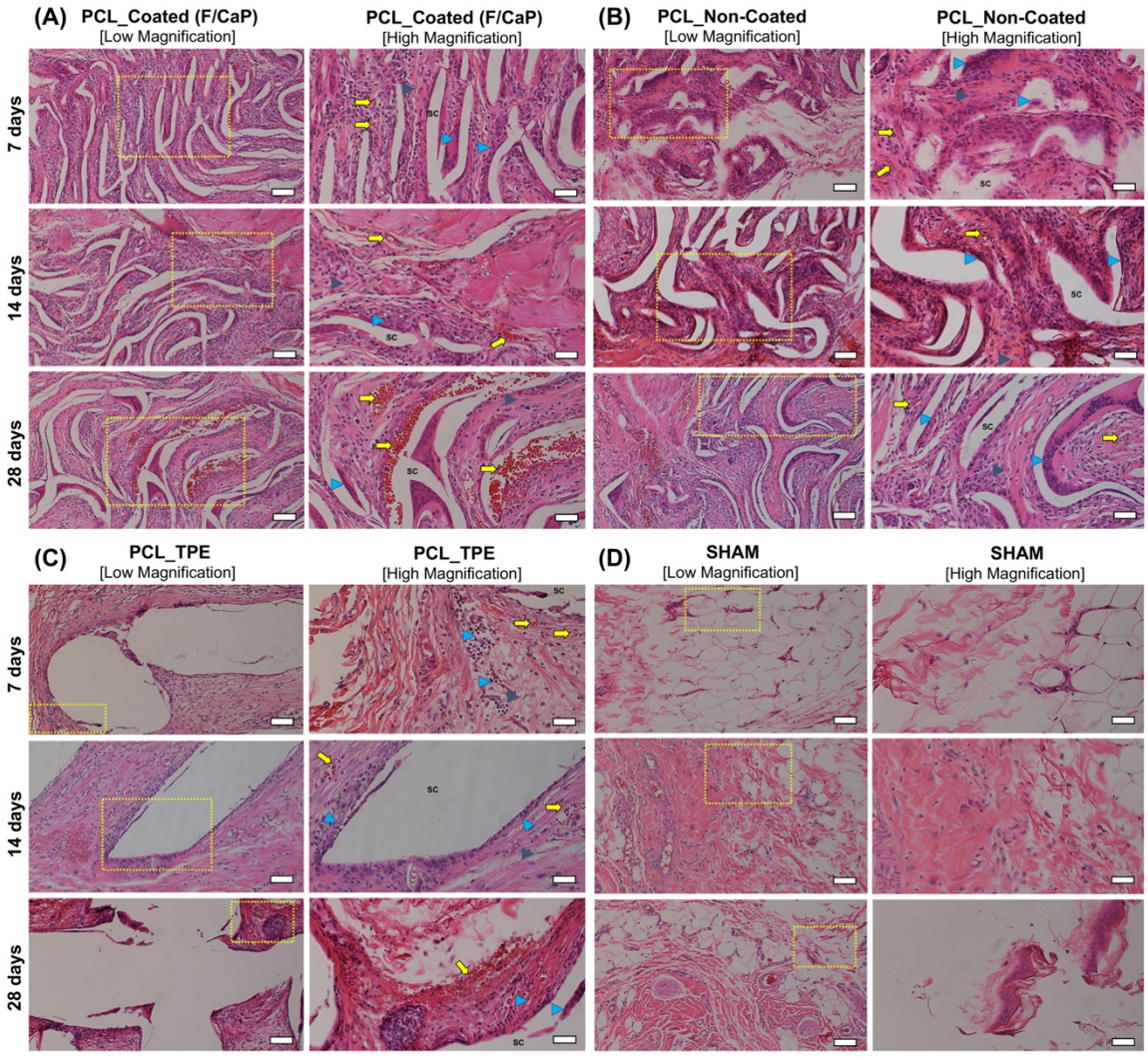

Figure 3-9 Panoramic view (scale bar = 200 µm) and 4× magnification (scale bar 100 µm) of representative H&E staining of the implanted scaffolds

(a-b) F/CaP-coated, and **(c-d)** non-coated scaffolds after 7 days and 14 days, respectively, compared to **(E-F)** polymer thermal extrusion (PTE) after 7 days and 6 months. Black dashed lines delineate the implanted scaffold border, highlighting the tissue ingrowth over time.

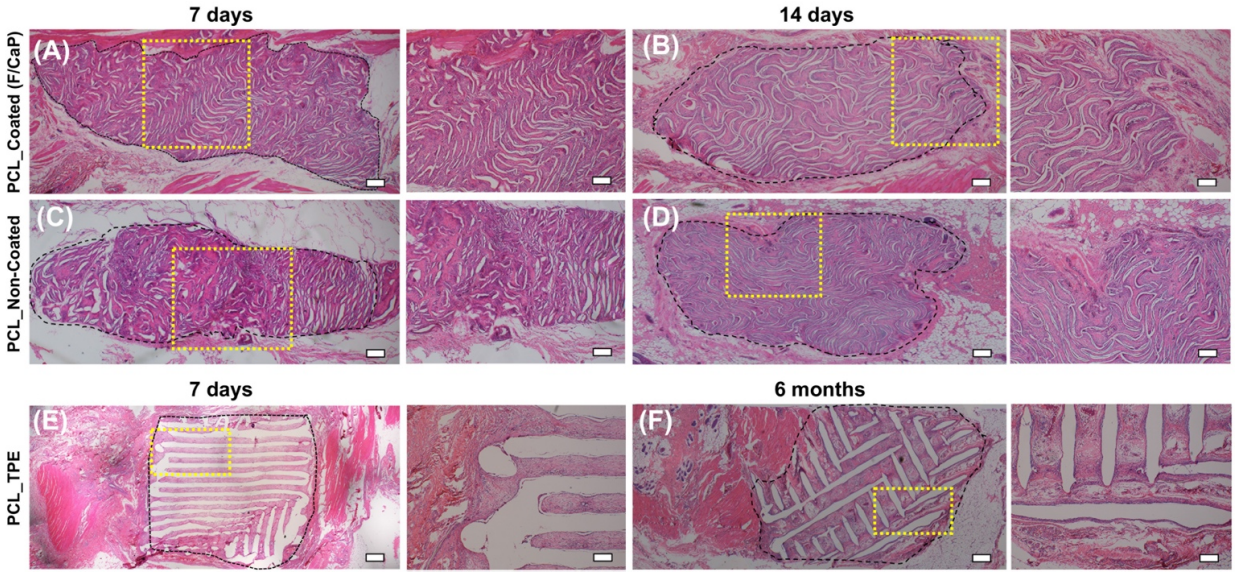

Figure 3-10 Representative H&E staining and histological analysis of the implanted scaffolds

(a) F/CaP-coated, **(b)** non-coated, **(c)** polymer thermal extrusion (PTE), and **(d)** sham – control after 7, 14, and 28 days *in vivo* (10× [low magnification, scale bar = 50 μm] and 20× [high magnification, scale bar = 25 μm]). Scaffold: Sc, Blood vessels: Yellow arrow, Inflammatory cells: Blue Arrowhead; and Fibroblasts: Grey arrowhead.

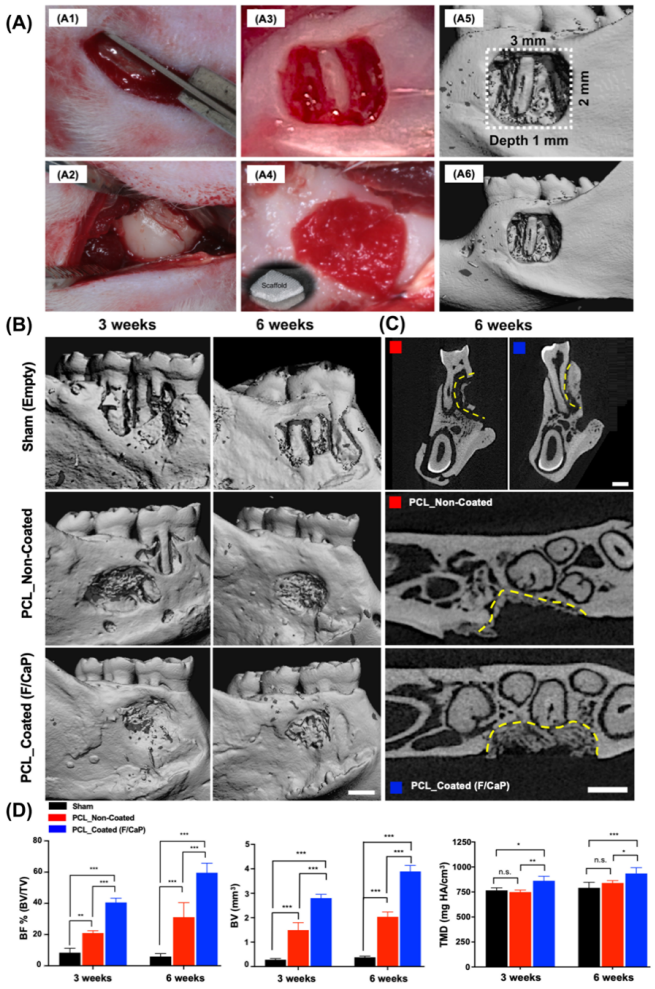

Figure 3-11 Generation and characterization of rat mandibular periodontal fenestration defect model

(a1-a3*)* Macrophotographs of a rat mandible after the incision, flap elevation, creation of the defect. **(a4)** implantation of F/CaP-coated scaffold in the defect, it has the ability to absorb of blood instantly and acts as clot retention. (a5-a6) Micro-CT 3D reconstruction images show the 3 × 2 mm × 1 mm standardized defect on the buccal side of the first and second molars of the rat. The distal root of the mandibular first molar was exposed in the middle of the defect**. (b)** Representative micro-CT images of the fenestration defect exposing the distal root of the first molar and the mesial root of the second molar at 3 and 6 weeks in the control, non-coated and F/CaP-coated groups. (c) 2D cross-sectional and transverse views highlight the visual differences between the area and density of bone regenerated within the defect (indicated by yellow lines). Scale bar = 1 mm. **(d)** Micro-CT assessments of bone volume, bone fill, and tissue mineral density at 3 and 6 weeks post-implantation within different groups. The F/CaP-coated group showed significant differences for bone volume and bone fill compared to both non-coated and control groups. Mean±SD (n=4). ANOVA: ***p<.001, **p<.01, *p<.05.

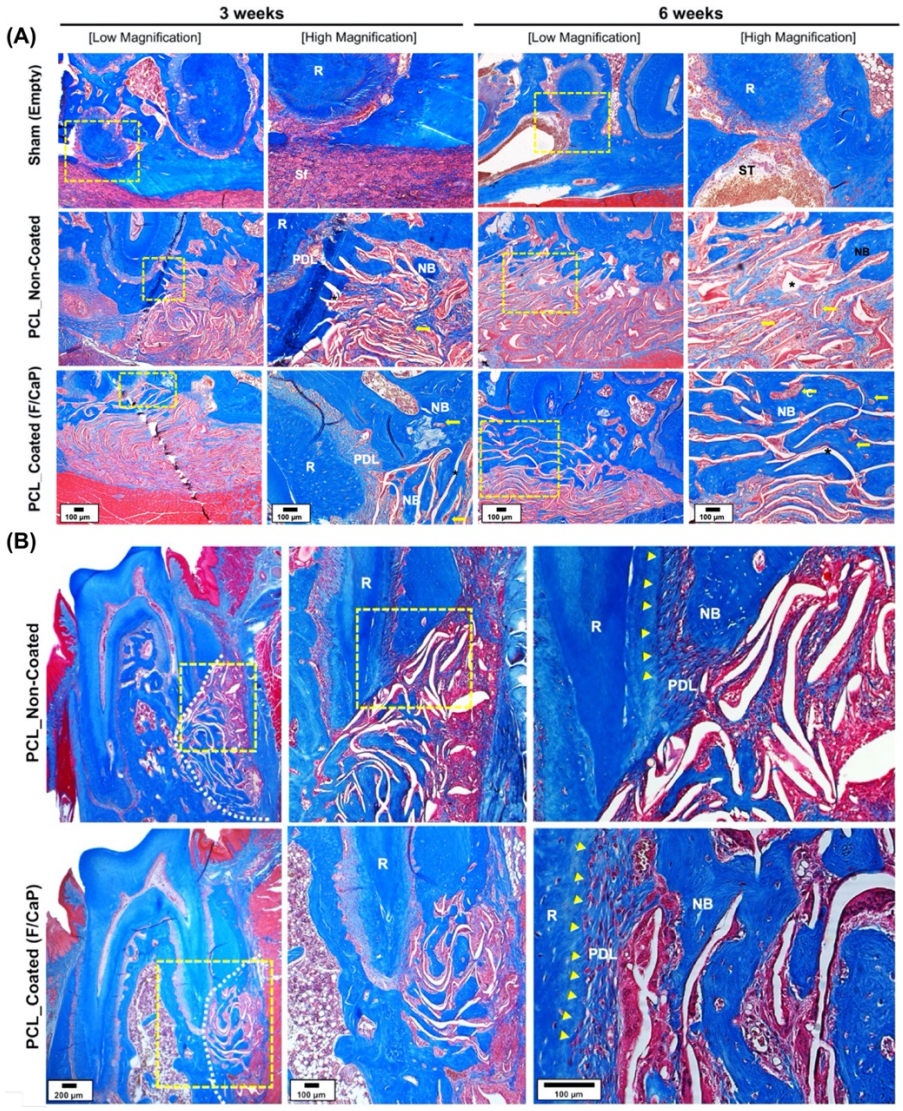

Figure 3-12 Histomorphological Assessment of Soft and Mineralized Tissue Formation

(a) Representative MT-stained horizontal cross-sections of non-coated and F/CaP-coated scaffold-treated defects at 3 and 6 weeks post-implantation. Photomicrographs of the defect area show newly formed bone and PDL. **(b)** Representative MT-stained longitudinal sections of non-coated and F/CaP-coated scaffold-treated defects at 6 weeks post-implantation. Analyses for periodontal regeneration on the tooth-root surface indicated neotissue formation and Sharpey's fiber insertions to new bone and cementum. White dotted line: defect site; Yellow arrows: vascularization; Asterisks (*): scaffold, Yellow arrowhead: cementum; New bone: NB; Root surface: R; Periodontal ligament: PDL; and Soft tissue infiltration: Sf.

CHAPTER 4

Personalized and Tissue-Specific Melt Electrowritten Scaffolds for Coordinated Regeneration of Soft and Hard Periodontal Tissues

Abstract

Periodontal disease is a chronic inflammatory condition that causes destructive damage to tooth-supporting tissues. The limited successful outcomes of clinically available approaches underscore the necessity for therapeutics that not only provide topographic guidance to cells but also modulate the local immune response. In the present study, three-dimensional (3D) MEW scaffolds with tissue-specific attributes were engineered to provide cues to drive periodontal ligament stem cells' (hPDLSCs) differentiation and macrophages polarization. hPDLSCs were capable to elongate along the axis of highly oriented (*i.e.*, aligned) fibers and spread along the walls of 250 μm and 500 μm strand spacings, while spread out morphology was noticed on random fibers. Moreover, macrophages exhibited elongated morphology in aligned and highly porous scaffolds, while maintaining their round-shape morphology in random fibers after 3 days of culture. Expression of periostin and IL-10 were significantly more prevalent on the aligned and porous scaffolds. While the 500 μm strand spacing shows higher expression of osteogenesis markers (Runx2) over 21 days, the random fibers show upregulation of M1

markers (IL-1 and IL-6). The *in vivo* findings indicated the potential for tissue-specific scaffolds to promote the organized regeneration of periodontal tissues and robust formation of new bone in the mandibular rat fenestration defect model. Collectively, our results indicate the necessity of an instructive biomaterial-based scaffold to direct stem cell differentiation and macrophage polarization for effective complex periodontal tissue regeneration.

KEYWORDS: *periodontitis, melt electrowriting, 3D printing, scaffold, macrophages, polarization, guidance, bone regeneration, periodontal regeneration*

4.1 Introduction

Periodontitis is a chronic inflammatory disease affecting approximately 47% of adults 30 years of age and older. If left untreated, it leads to severe destruction of the periodontium, *i.e.*, the alveolar bone, periodontal ligament (PDL), and cementum, ultimately leading to tooth loss.[1,2] Regrettably, regeneration of tooth-supporting structures has been a somewhat elusive goal in periodontics. Contemporary approaches to treat periodontitis involve thorough subgingival scaling and root planing, open flap surgery, guided tissue/bone regeneration (GTR/GBR).[2] The formation of new bone, cementum, and periodontal ligament (PDL) is possible using these modalities, though predictable outcomes are not always significant. Despite evidence that some level of periodontal regeneration may occur following currently available regenerative therapeutics,[3] full regeneration may be impractical in many cases, due to the complexity of tissue architecture. The ligament component of the periodontium is a multifunctional fibrous tissue and plays a crucial role in optimizing various biomechanical and biophysical responses to the masticatory force.[4]

Therefore, the acquisition of well-oriented PDL fibers with alveolar bone regeneration is of great significance in periodontal tissue engineering.

Periodontal regeneration requires simultaneous management of both soft and hard tissue interfaces. Indeed, it has been postulated that successful tissue integration *in vivo* could be facilitated through advanced scaffold design to reestablish the critical structure-function relationship inherent to the native hard-to-soft tissue interface. In melt electrowriting (MEW), biodegradable and FDA-approved polymers, such as poly(ε-caprolactone) (PCL), can be processed in their pure form, and typically, it leads to micron-sized fibers.[5] In predefined patterns, the fibers are stacked to create true 3D cell invasive scaffolds.[5,6] In this way, utilizing MEW to fabricate tissue-specific scaffolds for compartmentalized tissue healing is key to controlling the spatiotemporal events to allow simultaneous regeneration of soft (PDL) and hard (*i.e.*, cementum and alveolar bone) periodontal tissues. Noteworthy, our group has recently demonstrated that the presence of a fluorinated calcium phosphate (F/CaP) coating over MEW PCL scaffolds led to robust alveolar bone formation *in vivo*. Furthermore, the chemical composition of the developed nanostructured F/CaP coating revealed promising antimicrobial action against *Porphyromonas gingivalis*, a keystone Gram negative bacterial pathogen.

Although monophasic F/CaP coated scaffolds might enable tissue regeneration, recent literature states that it will be virtually impossible to form the angular structure of PDL at the bone–ligament interface, and the result would not be true regeneration of the lost structures. Moreover, scaffold orientation *i.e.* alignment has the potential to improve structural and functional integrity of tissue where the alignment is a principle of function such as cardiac, nerve, and PDL tissues.[7–9]

Meanwhile, biomaterial-based strategies, which provide 3D templates and biomimetic extracellular matrix (ECM) environments, have been proposed for periodontal tissue regeneration,[10] while simultaneously guiding immune responses.[11] The innate immune response plays important role after implantation of biomaterials to mitigate the pro-inflammatory reaction and allows macrophage polarization. Pro-inflammatory M1 macrophage conversion of M2 to anti-inflammatory phenotype macrophage is a key player in the overall inflammatory response at the site of biomaterial implantation. Thus, biomaterial-informed constructs are analogous, if not a conceivable substitute, for presently used soluble biomolecules in directing the response of progenitor cells to promote tissue healing and, ultimately, regeneration. Our approach focuses on using MEW to obtain a scaffold with dual function of presenting a porous structure and highly oriented fibers for the guidance of bulk and oriented tissue formation of both mineralized and soft tissue complex. Given that biomaterials can effectively be used to guide complex tissue regeneration or modulate the inflammatory response after periodontal tissue destruction, limit the extent of damage, and amplify the regenerative outcomes. In the present work, MEW was utilized to produce scaffolds at several defined orientations and strands spacing with advanced precision. Scaffolds that comprise a crosshatch pattern of 500μm strands spacing down to 250μm spacing, randomly oriented to highly aligned scaffolds were fabricated. Scaffolds were then seeded with hPDLSCs for analysis of cell behavior and thorough functional evaluation regarding gene expression of ligamentogenesis and osteogenic markers. The findings provide evidence of morphological and functional changes in response to scaffold alignment. Specifically, aligned fibers strongly support ligamentogenesis markers whereas highly porous

strands spacing of 500μm supports osteogenesis. Moreover, scaffolds orientation and strands spacing directly correlate to the morphological elongation of macrophages and differentiation toward M2 Phenotype. The *in vivo* findings confirmed that a structured scaffold of aligned PDL compartment and 500 μm spacing for bone compartment were optimal for coordinated periodontal tissue regeneration in a well-established rodent mandibular fenestration defect model. Altogether, this suggests that biomaterial-based constructs might set a platform for periodontal tissue regeneration as well as modulation of the immune response in inflammatory driven disease such as periodontitis. Despite that 3D environment created by MEW scaffolds at various orientations and strands spacing was sufficient for macrophage polarization and release of anti-inflammatory cytokines *in vitro*. Future studies to evaluate the effect of macrophage polarization in response to scaffold orientation and its effect on periodontal tissue damage and regeneration in *in vivo* setting of inflammatory created periodontal defect model are warranted.

4.2 Results and Discussion

4.2.1 Fabrication and characterization of MEW scaffolds

MEW was used to manufacture 3D fibrous scaffolds with distinct designs, namely crosshatch 0/90 with 250 μm strand spacing (small) and 500 μm strand spacing (large), as well as highly-oriented (aligned) and non-oriented (random) fiber configurations. SEM images of different fiber alignments and organizations are shown in **Figure 1**. Obviously, MEW results in formation of macrofibres with high porosity and smooth morphology. The random scaffold displayed overall porosity of 30.97% comparable to those observed in solution electrospinning.[12] Despite that MEW scaffolds follow a predefined design, the

higher voltage, and mass flow rates were critical variables to form electrical instability in order to allow random deposition of the polymer melt. Therefore, increasing the voltage and the feed rate were sufficient to create a randomly deposited design over the collecting plate. Indeed, due to the accurate nature of MEW fibers deposition, generating oriented fiber suspension over specific strands spacing is poor.[13] Thus, by decreasing the strands spacing to 100 µm, the remaining electrical charges within fibers started to create repelling forces. The repelling forces were advantageous to prevent fiber stacking. Accordingly, the formed scaffolds exhibited highly oriented fibers supported by the main strands at 0º, which was critical to maintaining the 3D characteristic of the scaffolds. Moreover, once the balance was achieved between electric voltage, pressure, feed rate, and adequate strand spacing to eliminate the effect of remnant charges, highly ordered uniform fibers stacking were achieved. Thus, highly ordered, small, and large strands of 250 µm and 500 µm spacing were created with homogenous interconnected porosity. The produced scaffolds display fiber diameters (in µm) ranging from 2.3 ± 0.1, 2.5 ± 0.2, 2.6 ± 0.3 and 4.2 ± 0.7 and porosity of 52.9%, 91.7%, 85.5 and 30.9% in aligned, large and small strand spacing to randomly deposited fibers, respectively.

4.2.2 hPDLSCs alignment and differentiation depends on scaffold architecture and fiber orientation

Specific orientations of fibrous tissues at tissue interfaces have vital roles in optimizing various biomechanical and biophysical responses *i.e.* absorption of external forces and their transmission and distribution into the bony structure.[14] For example, angulated PDLs that anchored the teeth inside the alveolar bone play a key role in absorptions and the distribution of masticatory/occlusal forces. Therefore, successful

regeneration of the angular structure of PDL at the bone–ligament interface is vital for formation of maturely functional tissues. However, there is still a significant challenge in managing the perpendicular angulations of the ligamentous compartment. A highly oriented guiding scaffold complex system could encourage the simultaneous regeneration of tooth-ligament-bone complexes via fabrication of structured scaffolds *i.e.* aligned fibers for PDL compartment and highly porous scaffold for bone compartment.[14] Guiding cells in a structurally preferential direction through substrate architecture have been shown to stimulate cell behaviors and further mimic the natural form and function of various tissues, such as ligament, cardiac, and nerve tissue.[9,15–17] Thus, our objective here is to optimize the PDL compartment scaffold parameter (*i.e.*, fiber organization) by determining its effects on hPDLSCs behavior and function.

First, in order to define the stemness of the hPDLSCs utilized throughout this investigation, the expression of specific cell surface markers CD90, CD105, and CD44 was evaluated.[18] Following proper isolation and expansion of human-derived PDLSCs, high levels of CD90 (>99.7%), CD105 (>99.96%), and CD 44 (>99.70) were identified. As expected, it fails to express the hematopoietic stem cell marker CD34 **(Figure 2)**. Meanwhile, the hPDLSCs could differentiate into osteogenesis, ligamentogenesis and, cementogenesis lineage, which make them appropriate for regeneration of periodontal complex.[19] Notably, the fate of PDLSCs is determined by the local microenvironment *i.e.,* the inclusion of soluble cues such as bioactive molecules and growth factors may direct osteogenic or fibroblast linage.[20] Equally important, biomaterial-based approach *i.e.* scaffold's stiffness and alignment, further facilitate hPDLSCs differentiation and maturation. [7,9]

Of note, PDLSCs responded to a certain substrate topography and alignment in an inimitable manner, modulating their proliferation and differentiation capacity. While hPDLSCs seeded on random and aligned fibers show higher proliferation compared to scaffolds with strands spacing **(Figure 3a)**. Small strands show a significantly higher proliferation rate compared to scaffolds with large strand spacing at day 1 through day 7 **(Figure 3a)**. In agreement with previously observed proliferation pattern in scaffold of 500 µm spacing to 1000 µm (F/CaP). The observation can be attributed to the limited porosity of randomly non oriented, highly oriented aligned fibers and small strands spacing compared to larger strands spacing that enhances the cells seeding efficiency and ultimately the proliferation.

The direct changes in hPDLSCs morphology that refer to contact guidance in different scaffolds are evident in **Figure 3b**. The constructs with parallelly oriented fibers allow hPDLSC to align parallel to the direction of fibers long axes **(Figure 3b)**, while in random and spaced constructs, hPDLSCs exhibit a polygonal shape, extended cytoskeleton in multiple directions, and disorganized cellular orientation. Interestingly, the pattern of cells spreading in randomly oriented scaffolds was comparable to that observed in the crosshatch pattern of 250 µm. However, the randomly oriented fibers presented characteristics similarly to previously observed in solution electrospun fibers where lack of sufficient porosity limit the cellular infiltration and ultimately results in 2D substrates covered with cells on its superficial layers. While highly ordered interconnected porous scaffold produced by crosshatch patterns provided a true 3D environment where cells were able to spreads throughout each pore and ultimately result in a more pronounced effect on tissue formation.[5]

While at day 3, the cells' cytoskeleton starts to spread at the corner of individual strands in the crosshatch patterns of 250 μm and 500 μm; at day 7, more extended behavior to fill in between strands is more evident in small strand spacing compared to the larger one. **(Figure 4a)**. Whereas, in randomly oriented fibers the nuclei exhibited multi directional angulation dictated by underlying fibers **(Figure 4b)**, the effect of aligned fibers on hPDLSCs is more dramatic due to contact guidance, which provides an elongated pattern of the cytoskeleton and nuclei alignment along fibers' axes **(Figure 4b)**. Thus, hPDLSCs adopted typical spindle-like shapes, characteristic of previously observed in human fibroblasts.[21]

Although many studies have suggested the possible correlation of contact guidance and periodontal tissue regeneration,[14,22] the associated functional changes in hPDLSCs have not been evaluated in highly aligned and random compared to the crosshatch patterns of fibrous MEW scaffolds **(Figure 5)**. Considerably, cell morphology corresponds to functional changes in MSC, those changes range between proliferation, differentiation, and linage commitment.[14,23,24] Under proper stimuli, hPDLSCs can be manipulated to adopt self-renewal and multiple lineages differentiation.[17,18] In order to evaluate the differentiation potential of hPDLSCs on scaffold with random or aligned orientation, and on small, or large strands spacing, the expression of coding genes specific for ligamentogenesis and osteogenesis was evaluated in the absence of differentiation factors.

hPDLSCs cultured on scaffolds with various orientations and strands spacing exhibited different mRNA expression profiles of periostin (POSTN), Scleraxis (SXC), Collagen III (COL3), and Runt-related transcription factor 2 (RUNX2), coding for

ligamentogenic and osteogenic differentiation. In particular, the matricellular protein, POSTN, is highly expressed in collagen-rich connective tissues, and its expression reveals integrity and maturation of the periodontal ligament matrix.[25,26] Strand spacing and alignment significantly change the expression level of POSTN mRNA at day 3, with far superior expression in aligned compared to random scaffolds and scaffolds with small and large strands spacing. On day 7, POSTN expression was upregulated in all scaffolds with a significant increase in the aligned group. Meanwhile, SXC transcription factor is specific for tendons and ligaments and is essential for cell differentiation and matrix organization, where evaluated.[27] Overall, the level of SXC expression in aligned scaffolds was higher than non-aligned structures *(i.e.,* randomly oriented fibrous scaffolds and crosshatch patterns) at days 3 and 7 (P<0.05). On the other hand, COL3 presented at the early phases of the wound healing and predominantly constituent of tendon/ligament-related extracellular matrix (ECM), contributes to the formation of the collagen bundle and the overall enhancement of PDL mechanical properties.[25] The expression of COL3 in aligned and small strand spacing (250 microns) crosshatch scaffolds were not significantly different; whereas, for the larger strand spacing it was significantly lower than former scaffolds with small strand spacing at day 3 (P<0.01). On day 7, the expression of COL3 increased in crosshatch scaffold with small and large spacing and reached comparable levels to the aligned fibers. In terms of osteogenic gene expression, Runt-related transcription factor 2 (RUNX2), which synchronizes osteoblast differentiation, is highly expressed in bone and periodontal ligaments.[28] RUNX2 expression was generally upregulated at days 3 in crosshatch scaffold with small strands spacing and was significantly higher in the randomly oriented scaffolds. On day 7, RUNX2 expression was

upregulated in crosshatch scaffolds with large strands spacing and downregulated in aligned scaffolds. Whereas at day 14, the pattern of RUNX2 expression tends to downregulate compared to day 7, however, it was significantly higher in crosshatch scaffold with small and large strands spacing compared to randomly oriented and aligned scaffolds ($P<0.05$).

Collectively, increased ligamentogenesis and partially decreased osteogenesis of hPDLSCs mediated by aligned fibers' architecture/configuration were noted. While in the absence of any differentiation factors, the upregulated expression of osteogenesis markers of hPDLSCs in crosshatch scaffolds is likely mediated by altered cell shapes in response to different scaffolds configuration, which ultimately alters the commitment of hPDLSCs fate. In agreement with previous work where MSCs commitment was dependent upon changes in cell shape, cytoskeletal tension, and RhoA signaling in response to mechanical cues.[29] In particular, aligned fibrous substrates show the ability to promote differentiation of cells into tendons/ligaments,[30] whereas, non-aligned fiber configuration allows cells to exhibit a more spread out morphology and direct osteogenic fate.[6]

Designing scaffolds to closely mimic native tissues might be helpful for enhanced PDL and bone formation through improving the microstructure and perhaps the function of regenerated tissue.[31] Hence, based on our *in vitro* findings, the presence of the aligned fibers results in a robust expression of ligamentogenic markers. Those markers are essential for proper matrix formation and maturation of PDL *in vivo*.[31] In the present investigation, we did not use any differentiation medium to culture the hPDLSCs; our prime motivation was to demonstrate the possibility of multilineages' differentiation based

on scaffolds' configuration to allow for the formation of tissue-specific scaffolds. Therefore, we hypothesized that the presence of scaffolds with tissue-specific architecture/configuration would allow for simultaneous regeneration of both hard and soft tissues and further formation of mature PDL by directing the initial attachment, morphology, and activation of initial signaling pathways essential for ligamentogenesis and osteogenesis.

4.2.3 Macrophage elongation and polarization depends on scaffold architecture/configuration

Biomaterials for tissue engineering guide for cell attachment and differentiation, and conceivably the potential to mitigate inflammatory response after implantation.[32,33] Upon biomaterial implantation, blood plasma and proteins attach to its surfaces, promoting host cells, including monocytes, fibroblasts, and macrophages, to interact with the biomaterials.[34] Persistent inflammation causes the formation of fibrotic tissue that encapsulates the biomaterial, leading to implantation failure.[35] Hence, monocyte-derived myeloid cells and macrophages play a vital role in controlling the biomaterial-triggered inflammatory response.[35]

Conventional immunomodulatory strategies have been explored in preclinical periodontitis via incorporation of anti-inflammatory molecules.[36,37] The proposed mechanism for anti-inflammatory molecules is to halt the inflammation and boost a regulatory immune response via macrophages polarization.[38] Furthermore, macrophages polarization and stimulation of M2 phenotype showed an inhibitory effect of bone loss in murine periodontitis model.[39,40] Herein, we hypothesized that scaffold architecture and overall fiber configuration in a biomaterial-based approach could play a role on

macrophage polarization and counterpart the regeneration of tooth supporting structure. To investigate the immunomodulatory effect via controlling scaffolds orientation and strands spacing, RAW 264.7 cells were seeded on scaffolds, *i.e.*, random, aligned, small, and large strand spacing. Furthermore, *E. coli* lipopolysaccharide (LPS), a well-known inducer of the expression of inflammatory markers, was added to culture media, and the phenotype of macrophages was determined by qPCR and ELISA.

Macrophage subpopulations M1 and M2 are distinguished by morphology and secreting distinctive cytokines; each plays a pivotal role in the immune response.[11,41] Physical cues in the local microenvironment regulate macrophage phenotypic polarization and exert elongation-driven polarization.[42,11] In order to explore the relation of macrophage cell shape and polarization, RAW 264.7 cells were seeded on scaffolds with various fiber configurations and alignments *i.e.* random, aligned, and scaffolds with small and large strands spacing **(Figure 6)**. RAW 264.7 cells cultured on a random scaffold were able to maintain round appearance at day 1, while cells' elongation was more prominent when macrophages were cultured on an aligned scaffold. Meanwhile, cell spreading behavior and elongation remained comparable in non-stimulated and LPS-stimulated RAW 264.7 cells on all tested scaffolds **(Figure 6a&b)**. Remarkably, even in an inflammatory stimulated *milieu*, fiber alignment and strands spacing tend to influence macrophage elongation. Furthermore, the elongation is believed to promote changes in the expression of phenotypical markers for M2.[42]

As expected, at non-stimulated conditions, cells cultured on scaffolds at different alignment and strands spacing failed to express the inflammatory markers IL-1β and IL-6 and were found to express M2 marker IL-10. LPS-stimulated macrophages showed

stronger upregulation for IL-1, in contrast, the expression of IL-6 was maintained constant at day 1 through day 7 despite continuous induction of LPS into culture media. Meanwhile, stronger upregulation of IL-10 was also detected at day 1, as an adaptive mechanism in LPS stimulated macrophages in order to down regulate the expression of TNF-α, IL-1, and IL-6, proinflammatory cytokines.[43–45] At day 3 and day 7, the IL-10 continues to express a significantly higher level in aligned scaffolds and scaffolds with small and large strands spacing compared to control (TCP) (P<0.05). While random scaffold was not significantly different from the control (TCP) **(Figure 7)**. In accordance with previous studies, where 2D cultures and random scaffolds stimulate the release of pro-inflammatory cytokines.[11,46] These data support the hypothesis that cell elongation might promote macrophage polarization and further release of M2 cytokines, although it maintains a constant level of the inflammatory cytokines over 7 days due to continuous induction of LPS into the culture medium.

The profiles of gene expression in LPS-stimulated RAW 264.7 were evaluated over 7 days **(Figure 8)**. The expression is highly dictated by scaffolds orientation; RAW 264.7 cultivated on aligned and scaffolds with small and large strands spacing showed upregulation of M2 Markers IL-10 and MRC-1 and downregulation of the M1 markers, IL-1β, compared to random and control (TCP) **(Figure 8)**. While the expression of IL-1β at day 3 and day 7 was not significant in all tested groups, it was downregulated compared to control (TCP). Whereas at day 7, the MRC-1 showed a stronger downregulation in random fibers and was significant compared to aligned and crosshatch design with small strands spacing. Taken together, the data suggested that a highly aligned and crosshatch scaffold design promotes macrophage polarization toward M2, the prohealing phenotype.

It is believed that the M2 phenotype possesses distinct functionality from the M1 to upregulate the factors involved in repair and regeneration via stimulation of cell proliferation and deposition of the extracellular matrix and angiogenic effect to support tissue regeneration.[47]

4.2.4 Biocompatibility of collagen-infused MEW PCL scaffolds in vivo

Given that the collagen phase provides sufficient support for the scaffold and offers a biomimetic local biological microenvironment to emulates those of native tissues and to enhance the vuscularization.[5] First, the biocompatibility of the fabricated F/CaP-coated and non-coated scaffolds in the presence and absence of collagen was evaluated in a well-established subcutaneous model. This model provides insight to explore cellular infiltration properties, blood vessels' formation, and potential inflammatory response elicited by the scaffolds due to their composition and/or degradation byproducts. Hematoxylin and eosin (H&E) images of processed scaffolds post-implantation (*i.e.*, F/CaP-coated, non-coated, F/CaP-coated+collagen, and non-coated+collagen) are shown in **Figure 9**. Implants were retrieved 7-, 14-, or 28-days post-implantation; the histological sections show a collagenous ECM and significant ingrowth of host tissues. Moreover, no noticeable signs of inflammation were identified in any of the implanted scaffolds. The scaffolds revealed significant integration with the host tissues with numerous blood vessels infiltration into F/CaP-coated and F/CaP-coated+collagen. Blood vessel density increased over 28 days in F/CaP coated and non-coated scaffolds, and that attributed to the high porosity of MEW constructs~ 91.7% **(Figure 10a&b)**. Apparently, blood vessels infiltration was greater in F/CaP-coated scaffolds, as previously observed.[56] The release of Ca ions from F/CaP-coated scaffolds, encourages the release

of vascular endothelial growth factor (VEGF) from endothelial progenitor and subsequently enhance the vascularization.[48,49] Moreover, patent vessels stained by anti-human CD31 were evident throughout all F/CaP coated and collagen infused scaffolds. The anti-CD31 staining cells became favorably high in the coated group compared to the non-coated group. Amplified ingrowth of CD31 positive vessels was evident in collagen infused groups with a significant increase in the F/CaP-coated scaffolds compared to non-coated. Enhanced vascularization can be attributed to the ability of type I collagen to facilitate endothelial cells' migration and enhance angiogenesis.[50]

4.2.5 In vivo evaluation of tissue-specific scaffold's guidance for periodontal regeneration

The proposed scaffold is expected to exhibit cues to guide fibrous formation. In order to elucidate the importance of scaffold guidance on periodontal regeneration, tissue specific scaffolds were fabricated via MEW and further infused with collagen type I to enhance the biocompatibility and blood vessels infiltration. Moreover, the regenerative potential of the proposed scaffold was tested *in vivo* following classical fenestration defect model.

The tissue-specific scaffolds exhibited different fibers' orientation; SEM images in Figure 11a. show highly aligned oriented fibers for PDL compartment at ~ 200 µm height resemble those of native PDL space and a highly porous bone compartment of large (500 µm) strands spacing at ~ 800 µm height. Furthermore, SEM micrograph of collagen-infused scaffolds shows uniform infiltration of the collagen into the highly porous F/CaP coated scaffolds of large strand spacing. Collagen type I, upon dissolving in acetic acid, exhibits a low viscosity that turns upon neutralization and temperature control to exhibit

self-assembly and hydrogen bond to form a solidified gel. The FTIR spectra of F/CaP coated scaffold showed vibrational bands from PCL at 2943 cm^{-1}, 2866 cm^{-1}, and 1700 cm^{-1}, as consistent with previous findings.[51] Additionally, collagen-infused F/CaP coated scaffold showed vibrational bands at 1650 cm^{-1}, 1540 cm^{-1}, and 3310 cm^{-1} attributed to the infused collagen **(Figure 1b)**.[51] In aggregate, the SEM and FTIR findings strongly suggest effective fabrication of collagen-infused MEW scaffolds.

The outcomes of tissue regeneration were evaluated in periodontal fenestration defect models in rat mandible **(Figure 11c)**. Tissue-specific scaffolds resulted in a simultaneous regeneration of PDL-bone interface. The compositional and structural organization of the fabricated scaffolds impart biomimetic functionality to tissue-engineered bone and soft tissues. The microCT analysis revealed a different level of bone formation at defect sites **(Figure 12)**. The control group showed partial tissue healing even after 6 wks. comparable to collagen group. While the tissue specific scaffolds showed significant healing, alternatively, the tissue specific infused with collagen demonstrated a more advanced formation of mineralized tissue at 4 and 8 wks. **(Figure 12a)**. Furthermore, abundant formation of new bone (BV) with a proper PDL space was observed and was statistically significant in the tissue-specific constructs compared to self-healing and collagen groups **(Figure 12b)**. Tissue mineral density (TMD) demonstrating maturity of bone showed significant difference ($p<0.001$) between tissue specific scaffold infused with collagen versus other groups at 3 weeks. Although at 6 weeks no differences between groups were detected.

The enhanced bone formation can be attributed to strands spacing of 500μm, was sufficient to supports mineralized tissue formation via improved vascularization and

further, the presence of F/CaP coating improves the bioactivity and influences mineralized tissue deposition. In agreement with Abbasi et al., a pore size of 500 μm resulted in the highest formation of newly formed bone as compared to a smaller pore size of 250 μm, while heterogeneous gradient significantly allowed for more new bone formation.[52]

Histological evaluation of the newly formed tissues revealed distinct architecture was comparable to natural periodontal tissues. While the control group showed soft tissue invasion because of epithelial tissue downgrowth, collagen implanted scaffolds exhibited high biocompatibility, due to the presence of integrin binding sites, which promote direct cellular interaction.[50] However, collagen alone fails to fully regenerate both hard and soft tissues. Remarkably, aligned/F-CaP coated scaffold provides guidance for complex tissue formation and the amount of new bone formation was higher in aligned/F/CaP-coated scaffolds compared to self-healing and collagen groups. While both tissue specific scaffolds maintained PDL space that resembles those of natural periodontal tissue **(Figure 13)**.

Additionally, the integration of polarized anchoring fibers oriented toward a mineralizing surface promotes adequate maturation and exhibits important biomechanical properties to regulate tissue adaptability and its long-term stability.[22] While F/CaP coated MEW scaffolds might allow tissue regeneration, as we previously reported, recent research suggests that forming the angular structure of PDL at the bone-ligament interface would be nearly impossible, and the result will not be true regeneration of the lost structures. Aiming to unveil the importance of tissue-specific scaffolds, immunohistochemical staining shows that the newly formed PDL tissue has mature structures for the groups that have tissue specific guidance **(Figure 14)**. Periostin

expression has been paired with PDL maturation to establish homeostasis within periodontal tissues.[31] At 6 weeks, the groups with tissue-specific scaffolds showed higher periostin expression similar to the remaining intact PDL area of the same tooth **(Figure 14)**. Interestingly, despite the amount of bone regeneration being higher in the collagen-infused scaffold group due to improved vascularization as noted previously, lower expression of periostin is evident compared to collagen-free tissue specific scaffolds. These findings are attributed to lack of organization caused by collagen infiltration, as it provides more binding sites for progenitor cells' infiltration. While the presence of tissue-specific scaffold alone was sufficient to reestablish mature PDL **(Figure 14)**. In aggregate, these findings indicate that structurally preferential alignment promotes mature PDL-like tissue formation over time, and the presence of F/CaP coating further enhances mineralized tissue formation.

4.3 Conclusions

This study presented structurally and compositionally biomimetic scaffolds for simultaneous regeneration of complex periodontal tissues. The results show that scaffolds' alignment and strands spacing have significantly increased expression of ligamentogenesis and osteogenesis, while this provides an immunomodulatory effect on macrophage toward M2 pro healing phenotype, even when the media is supplemented with LPS inflammatory inducer. These findings mandate for an instructive biomaterial-based approach to guide stem cell differentiation and macrophages' polarization.

4.4 Experimental Section

Materials and Chemicals. Poly(ε-caprolactone) (PCL, Mn:5000) was procured from CELLINK (Göthenburg, Sweden). All other chemical reagents and solutions were purchased from Sigma-Aldrich (St. Louis, MO, USA), unless otherwise noted—sodium hydroxide (NaOH, ≥ 98%), ethanol (99.5%), ethylenediaminetetraacetic acid calcium disodium salt (EDTA-Ca), potassium phosphate (KH_2PO_4 ≥ 99%), potassium fluoride (KF ≥ 99.9%), hexamethyldisilazane (HMDS ≥ 99%), hexadecylpyridinium chloride monohydrate (CPC), paraformaldehyde (PFA), and ascorbic acid-2 phosphate. Distilled-deionized (DI) water from a Millipore Milli-Q ultrapure water system (MilliporeSigma, Burlington, MA, USA) was used in the experiments. Phosphate-buffered saline (PBS) was procured from GIBCO Invitrogen (Carlsbad, CA, USA). Meanwhile, a 15% heat-inactivated fetal bovine serum (FBS) solution, alfa-minimum essential medium (α-MEM), and a 1% penicillin–streptomycin solution, were purchased from HyClone (Life Technologies Corporation, Gibco, Grand Island, NY, USA). Collagen type I PhotoCol® (Lot# 8292) was purchased from Advanced BioMatrix (San Diego, CA, USA).

Melt Electrowriting (MEW) and Scaffold Design. Poly caprolactone (PCL) is an FDA-approved polymer commonly used to fabricate scaffold using MEW technique due to its thermal stability and proper degradation behavior and overall biocompatibility *in vivo* for periodontal regeneration.[53] Here, MEW scaffolds were fabricated in a biosafety cabinet using a multi-head bioprinting platform (3DDiscovery, regenHU Ltd., Villaz-St-Pierre, Switzerland). The system contains a MEW printhead supplied with high-voltage power that pneumatically draws the polymer via a regulated feeding system. Moreover, the electrical heating system allows for control of the temperature of the metal cartridge to

melt the housed polymer (PCL) pellets. The design of the printing path was produced using BioCAD; a G-code file was created and saved to HMI software for printing. Briefly, polymer pellets were placed into the metal cartridge overlaid with a 26G nozzle, then heated to 90°C for a duration of 30 min to form a homogeneous polymer melt at 0.07 MPa system's pressure.[5] Scaffolds at highly aligned orientation and 0/90°crosshatch designs were printed at parameters of 40 mm/s feed rate, voltage of -7 kV, and at a distance of 4 mm from the collector at an ambient temperature of 21.5°C and a humidity level of ~ 38.5%. While randomly oriented fibers were printed at 0.1 MPa system's pressure, 40 mm/s feed rate and voltage of -10 kV. The 0/90°crosshatch laydown pattern has 500 µm strand spacing or 250 µm strand spacing. The aligned scaffolds have a major strand at 0° of 250 µm spacing and densely packed aligned fibers designed with 100µm strands spacing at 90°. The tissue specific scaffolds were designed to form a construct encompass 800 layers for the bone side and 200 layers for the PDL side.

In order to increase the hydrophilicity of PCL, the scaffolds were treated with 5M NaOH aqueous solution, as previously reported.[54] In brief, the scaffolds were washed with 70% ethanol for 15 min, then they were immersed in NaOH solution at RT for 4 h. In order to neutralize the pH, the scaffolds were rinsed thoroughly with DI water and left to air-dry overnight. To coat the scaffolds to enhance their bioactivity of the bone compartment, the F/CaP coating process was performed using a previously reported method for coating and characterization.[56] Finally, the scaffolds were sterilized using 70% ethanol and UV light for further *in vitro* and *in vivo* experiments.

Preparation of collagen type I. Collagen hydrogels were synthesized following the manufacturer's protocol. Briefly, Collagen type I solution (3 mg/mL) was dissolved in an

acetic acid. Prior to infusion to cells seeded with MEW fibers, the solution was neutralized using a neutralization agent provided in the kit. Then, the collagen was allowed to gellate at 37°C for 30 min inside the incubator. After gelation, cell growth media was added.

Morphological and Chemical Analyses. The morphology of the processed MEW PCL scaffolds (*i.e.*, 250 μm strand spacing, 500 μm strand spacing, aligned and random) were assessed using a scanning electron microscope (SEM, MIRA3, FEG-SEM, TESCAN Brno, Kohoutovice, Czech Republic). The presence of specific chemical group coding for F/CaP-coated PCL scaffold, collagen, and collagen infused scaffolds were used to determine successful formation of F/CaP-infused collagen. 16 scans with spectra between 4000 and 600 cm^{-1} at 4 cm^{-1} resolutions were recoded using an FTIR instrument in the Attenuated Total Reflectance-Fourier transform infrared spectrometer (ATR-FTIR, Thermo-Nicolet iS-50, Thermo Fisher Scientific Inc., Waltham MA, USA). Baseline correction spectra were centered and normalized for analysis.

Cell Culture. Human periodontal ligament (PDL) tissues were scraped from the middle segment of the root surface as previously reported.[18] Freshly obtained tissues were cultured on alpha-minimum essential medium (α-MEM), then the cells were collected, centrifuged, and resuspended for 60 min in solution containing PBS, 4 mg/mL dispase II, and 2 mg/mL collagenase type II at 37°C. The mixture was inactivated using α-MEM media containing FBS and 100 μM ascorbic acid 2 phosphate. The cells were allowed to grow in T-25 flasks and passaged as needed for further experiments.

Flow cytometry. In order to assess the presence and expression of MSC markers, Flow cytometry was performed following the criteria proposed by the Mesenchymal and Tissue Stem Cell Committee of the International Society of Cellular Therapy (ISCT): CD45,

CD90, CD105, CD34.[18,55] PDLSCs were harvested from T75 flasks, washed with PBS, and incubated with blocking solution, followed by incubation with specific antibodies conjugated with a fluorochrome, PE anti-human CD90 antibody, FITC anti-human CD34 antibody, APC anti-human CD105, and APC-H7 anti-human CD44 antibody. Then, samples were washed and placed in 100μL PBS followed by analysis. Flow cytometry was performed on the Sony MA900 Cell Sorter; the collected data were analyzed using FlowJo software (TreeStar).

Cell Proliferation. Human-derived periodontal ligament stem cells (hPDLSCs) at passage 5 were harvested and seeded on scaffolds (8×8 mm^2) at a density of 6×10^4 in 24-well low attachment plates (Corning Life Sciences, Tewksbury, MA, USA) and cultured in α-MEM supplemented with 15% FBS and % penicillin-streptomycin solution. The plates were incubated in an atmosphere of 95% relative humidity and 5% CO_2 at 37°C. To determine PDLSCs proliferation, MTS assay (CellTiter 96 AQueous One Solution Assay, Promega Corporation, Madison, WI, USA) was performed at selected time points over 7 days in brief at predetermined time points; the cells were then incubated for 2 h with MTS solution, followed by measuring absorbance in a microplate reader at 490 nm (Spectra iD3; Molecular Devices, LLC, San Jose, CA, USA).

Macrophage polarization. RAW 264.7 cell lines (American Type Culture Collection, Manassas, VA, USA) [ATCC® TIB-71™]), at passage 4, were used. The cells were harvested using a cells' scraper and seeded on (8×8 mm^2) scaffolds at a density of 6×10^4 in 24-well low attachment plates (Corning Life Sciences, Tewksbury, MA, USA) and cultured in DMEM high glucose medium supplemented with 10% FBS, in an atmosphere of 5% CO_2 and 95% humidity at 37°C, followed by qPCR and ELISA.

Cell/scaffold Interaction. Confluent PDLSCs and RAW 264.7 at passage 5 were harvested and seeded on the distinct MEW PCL scaffolds. Briefly, 6×10^4 cells/scaffold were seeded and cultured for 3 and 7 days. For SEM images, the cells were fixed in 4% PFA for 48 h at 4°C. Then, the scaffolds were dehydrated in ascending concentrations of ethanol (up to 100%), followed by overnight incubation in HMDS. Finally, the constructs were mounted on Al stubs using double-sided adhesive carbon tape, and then a thin layer of Au was sputter-coated for 70 sec (SPI-Module Carbon/Sputter Coater, Thermo Fisher Scientific Inc., West Chester, PA, USA) prior to SEM imaging. For fluorescence images, PDLSCs were fixed in 4% PFA for 30 min at 4°C, then washed in PBS (3×). The cells were subsequently permeabilized using 0.1% Triton X-100 solution for 5 min. After PBS (2×) rinsing, the constructs were blocked using 1.5% bovine serum albumin (BSA) in PBS for 30 min, and then stained with TRITC-conjugated phalloidin and DAPI (1:1200, Millipore Sigma) for 1h at RT, according to the manufacturer's instructions. Finally, the constructs were gently rinsed (3×) in PBS to remove phalloidin conjugate excess and placed on a glass slide for observation under confocal microscopes (Eclipse-Ti, Nikon Corporation, Tokyo, Japan).

mRNA expressions using real-time PCR. The expression of commonly used ligamentogenic (Periostin (POSTN, Hs01566750_m1), Scleraxis (SCX, Hs03054634_g1), Collagen III (Col3, Hs00943809_m1)) and osteogenic Runt-related transcription factor 2 (Runx2, Hs01047973_m1) genes were analyzed by a quantitative polymerase chain reaction (qPCR). Glyceraldehyde 3-phosphate dehydrogenase (GAPDH, Hs02758991_g1) was used as the housekeeping gene. Furthermore, for macrophage polarization, M1 markers, IL-1 receptor ligands (IL1, Mm00434228), M2

markers IL-10 receptor ligands (IL-10, Il10 Mm01288386 M1), and mannose receptor CD206 (MRC1, Mm01288386) were analyzed at days 1, 3, and 7. In brief, the cells were harvested, and the total RNA was isolated (Purelink RNA Mini Kit, Invitrogen Corporation), followed by cDNA synthesis using iScript RT Supermix (Bio-Rad Laboratories, Inc., Hercules, CA, USA). Finally, the ΔΔCq method was applied to measure the relative amount of gene expression from the quantification cycle (Cq) values retrieved by qPCR analysis. qPCR results were normalized to the reference sample.

Cytokine quantification via mouse quantikine ELISA kit. IL1β, IL-6, and IL-10 cytokine release levels of LPS-stimulated macrophages cultured on different scaffolds were evaluated using the Mouse Quantikine ELISA Kit (R&D Systems, Inc., Minneapolis, MN, USA), according to the manufacturer's instructions. The cytokines level was measured using the supernatants extracted at days 1, 3, and 7. The absorbance was measured on a plate reader (Tecan, Spectra iD3; Molecular Devices, LLC, San Jose, CA, USA) at 450 nm and corrected with the absorbance at the reference wavelength of 570 nm.

***In Vivo* biocompatibility and blood vessels formation.** All animal procedures were approved by the University of Michigan Institutional Animal Care and Use Committee (IACUC, protocol #PRO00008502). Nine 6-week-old male Fischer 344 rats (250-300 g) were used for the experiments (Envigo RMS, Inc., Oxford, MI, USA). All surgical procedures were performed under general anesthesia induced with isoflurane inhalation (Piramal Critical Care Inc., Bethlehem, PA, USA) (4-5%) and maintained with isoflurane (1-3%). After anesthesia, 5 subcutaneous pockets (for Sham, and 4 scaffold groups, *i.e.*, non-coated, F/CaP-coated, non-coated+COL, and F/CaP-coated+COL) were bluntly created through short dorsal skin incisions (10 mm in length), and square-shaped

samples (8×8 mm^2 and 0.45-mm thick) of F/CaP-coated and non-coated MEW PCL scaffolds were implanted (n=3/group/time point) per animal. At the end of each time point, the animals were euthanized using CO_2, and the samples were collected with the surrounding peri-implantation tissue and fixed in 10% buffered formalin. After fixation, the samples were embedded in paraffin and sectioned at 6 μm thick sections. The samples were then stained with H&E and images of the staind slides were obtained using light microscopy to evaluate tissue ingrowth, blood vessels infiltration and inflammatory response. (Nikon E800, Nikon Corporation).

Periodontal fenestration defect creation and new bone formation. All animal procedures were approved by the University of Michigan Institutional Animal Care and Use Committee (IACUC, protocol #PRO00008502). Twenty-four 6-week-old male Fischer 344 rats (300-320 g) were used for the experiments (Envigo RMS, Inc., Oxford, MI, USA). All surgical procedures were performed under general anesthesia induced with isoflurane inhalation (Piramal Critical Care Inc., Bethlehem, PA, USA) (4-5%) and maintained with an amount of isoflurane in between (1-3%). After proper anesthesia, periodontal fenestration defects were created surgically at 2×3 mm (height × width) and 1 mm in depth in the rat mandible. In brief, the alveolar bone, followed by cementum and other soft tissue components around the root, were removed. Prior to the scaffolds' placement, 20% barium sulfate ($BaSO_4$) was dissolved in distilled water, then the scaffolds were immersed in $BaSO_4$ to acquire a higher intensity and grayscale Hounsfield Unit. The scaffolds (n=6/group/time point) were placed inside the defects and evaluated for periodontal tissue regeneration after 3 and 6 weeks of healing. At predetermined time

points of 3- and 6-weeks post-implantation, the mandible was retrieved and fixed in formalin prior to micro-computed tomography and histological analyses.

Micro-computed tomography (microCT). Newly formed alveolar bone at each periodontal defect was evaluated using μCT 100 (SCANCO Medical AG, Brüttisellen, Zurich, Switzerland), following the scan parameters of 360° rotation using 70 kV, 114 μA monochromatic x-rays and 25 μm voxel sizes. The frames' exposure time was maintained at an average of 500 ms. To reconstruct the 3D images of the defect area, SCANCO Medical System software was used. Then, the 3D image was used to trace the original defect circumferential, which hereafter identified as the region of interest (ROI). For each sample, ROI was analyzed to quantify the following components: bone volume (BV), bone fill (BF, BV/TV), and tissue mineral density (TMD).

Histological analysis. Following the microCT scans, the mandibles of each group were decalcified with 10% EDTA solution for 3 weeks. The decalcified samples were dehydrated in an ascending alcohol concentration series and later embedded in paraffin prior to cutting sections in to 4-μm. The sections were followed by staining with Masson's trichrome. The samples were then imaged using a light microscope equipped with a digital camera (Nikon E800, Nikon Corporation) to detect mineralized bone formation.

Immunofluorescence analysis. 4 μm-thick sections were dewaxed at 60°C for 15 min, then rehydrated in ethanol gradients. In ordered to reduce endogenous peroxidase activity, the sections were incubated in 3% H_2O_2 for 20 min at RT. For blocking unspecific binding, the slides were incubated with 3% bovine serum albumin (BSA) for 10 min at RT, followed by incubation of primary antibodies: anti-periostin (rabbit polyclonal, ab14041, Abcam, Cambridge, MA, USA) (Dilution 1:500): overnight at 4°C. The slides were then

incubated with Alexa-conjugated secondary antibodies: Alexa Flour goat anti-rabbit IgG (H+L) (dilution 1:200) for 1 h at RT. Then, a drop of vectashield antifade mounting media with DAPI was added to the slide to visualize the cell nuclei. The untreated lingual side of the distal root of the same tooth was used as control for visualization of native PDL tissues. The negative controls section was incubated in PBS instead of the primary antibody. The images were obtained at 4× and 20× for anti-periostin use (Nikon E800, Nikon Corporation). For blood vessels' formation, the fixed slides of subcutaneously retrieved scaffolds were stained using anti-CD31 (mouse monoclonal, ab215911, Abcam). The images were obtained at 358 nm and 545 nm excitation wavelength for blue and red fluorescence at 10 × magnification using BZ-×710 (Keyence Corporation of America, Itasca, IL, USA). The area of CD31 positive signals was measured using Image J software.

Statistics. Statistical analyses were performed using the GraphPad Prism 5 software package (GraphPad Software, San Diego, CA, USA). Data are presented as Mean ± SD, unless otherwise noted. Group comparisons were performed using one-way or two-way ANOVA, followed by Tukey's multiple comparison post-hoc tests. A two-sided 5% significance level was used for all tests.

AUTHOR INFORMATION

Corresponding Author

*E-mail: mbottino@umich.edu

Author Contributions

Arwa Daghrery engineered all scaffolds presented in this work and also the material, biological and animal experiments including material characterization, cell culture, molecular and biochemical characterizations, periodontal fenestration animal surgeries and histological analysis. Jessica A. Ferreira assisted with surgery and micro-CT analysis. Jinping Xu assisted with Flow cytometry and immunohistochemistry. Mariane M. Azuma provided input with the ELISA assays and macrophages experiments. MCB supervised, revised, and finalized the manuscript, and is the corresponding author.

Notes

The authors declare no competing financial interest.

Acknowledgements

M.C.B. acknowledges the National Institutes of Health (NIH – National Institute of Dental and Craniofacial Research, grants K08DE023552 and R01DE026578), the OsteoScience Foundation (Peter Geistlich Research Award), the International Association for Dental Research (IADR-GSK Innovation in Oral Care Award), and the American Academy of Implant Dentistry Foundation (AAIDF). The content is solely the responsibility of the authors and does not necessarily represent the official views of the National Institutes of Health.

4.5 References

(1) Eke, P. I.; Dye, B. A.; Wei, L.; Thornton-Evans, G. O.; Genco, R. J. Prevalence of Periodontitis in Adults in the United States: 2009 and 2010. *J Dent Res* **2012**, *91* (10), 914–920. https://doi.org/10.1177/0022034512457373.

(2) Ivanovski, S.; Vaquette, C.; Gronthos, S.; Hutmacher, D. W.; Bartold, P. M. Multiphasic Scaffolds for Periodontal Tissue Engineering. *J Dent Res* **2014**, *93* (12), 1212–1221. https://doi.org/10.1177/0022034514544301.

(3) Pellegrini, G.; Pagni, G.; Rasperini, G. Surgical Approaches Based on Biological Objectives: GTR versus GBR Techniques. *Int J Dent* **2013**, *2013*. https://doi.org/10.1155/2013/521547.

(4) Kaku, M.; Yamauchi, M. Mechano-Regulation of Collagen Biosynthesis in Periodontal Ligament. *J Prosthodont Res* **2014**, *58* (4), 193–207. https://doi.org/10.1016/j.jpor.2014.08.003.

(5) Dubey, N.; Ferreira, J. A.; Daghrery, A.; Aytac, Z.; Malda, J.; Bhaduri, S. B.; Bottino, M. C. Highly Tunable Bioactive Fiber-Reinforced Hydrogel for Guided Bone Regeneration. *Acta Biomaterialia* **2020**. https://doi.org/10.1016/j.actbio.2020.06.011.

(6) Abbasi, N.; Ivanovski, S.; Gulati, K.; Love, R. M.; Hamlet, S. Role of Offset and Gradient Architectures of 3-D Melt Electrowritten Scaffold on Differentiation and Mineralization of Osteoblasts. *Biomaterials Research* **2020**, *24* (1), 2. https://doi.org/10.1186/s40824-019-0180-z.

(7) Suhaeri, M.; Subbiah, R.; Kim, S.-H.; Kim, C.-H.; Oh, S. J.; Kim, S.-H.; Park, K. Novel Platform of Cardiomyocyte Culture and Coculture via Fibroblast-Derived Matrix-Coupled Aligned Electrospun Nanofiber. *ACS Appl Mater Interfaces* **2017**, *9* (1), 224–235. https://doi.org/10.1021/acsami.6b14020.

(8) Li, X.; Li, M.; Sun, J.; Zhuang, Y.; Shi, J.; Guan, D.; Chen, Y.; Dai, J. Radially Aligned Electrospun Fibers with Continuous Gradient of SDF1α for the Guidance of Neural Stem Cells. *Small* **2016**, *12* (36), 5009–5018. https://doi.org/10.1002/smll.201601285.

(9) Ren, S.; Yao, Y.; Zhang, H.; Fan, R.; Yu, Y.; Yang, J.; Zhang, R.; Liu, C.; Sun, W.; Miao, L. Aligned Fibers Fabricated by Near-Field Electrospinning Influence the Orientation and Differentiation of HPDLSCs for Periodontal Regeneration. *J Biomed Nanotechnol* **2017**, *13* (12), 1725–1734. https://doi.org/10.1166/jbn.2017.2451.

(10) Sheikh, Z.; Hamdan, N.; Ikeda, Y.; Grynpas, M.; Ganss, B.; Glogauer, M. Natural Graft Tissues and Synthetic Biomaterials for Periodontal and Alveolar Bone Reconstructive Applications: A Review. *Biomater Res* **2017**, *21* (1), 9. https://doi.org/10.1186/s40824-017-0095-5.

(11) Tylek, T.; Blum, C.; Hrynevich, A.; Schlegelmilch, K.; Schilling, T.; Dalton, P. D.; Groll, J. Precisely Defined Fiber Scaffolds with 40 Mm Porosity Induce Elongation Driven M2-like Polarization of Human Macrophages. *Biofabrication* **2020**, *12* (2), 025007. https://doi.org/10.1088/1758-5090/ab5f4e.

(12) Daghrery, A.; Aytac, Z.; Dubey, N.; Mei, L.; Schwendeman, A.; Bottino, M. C. Electrospinning of Dexamethasone/Cyclodextrin Inclusion Complex Polymer Fibers for Dental Pulp Therapy. *Colloids and Surfaces B: Biointerfaces* **2020**, 111011. https://doi.org/10.1016/j.colsurfb.2020.111011.

(13) Dalton, P. D.; Grafahrend, D.; Klinkhammer, K.; Klee, D.; Möller, M. Electrospinning of Polymer Melts: Phenomenological Observations. *Polymer* **2007**, *48* (23), 6823–6833. https://doi.org/10.1016/j.polymer.2007.09.037.

(14) Park, C. H.; Kim, K.-H.; Lee, Y.-M.; Giannobile, W. V.; Seol, Y.-J. 3D Printed, Microgroove Pattern-Driven Generation of Oriented Ligamentous Architectures. *Int J Mol Sci* **2017**, *18* (9). https://doi.org/10.3390/ijms18091927.

(15) Pilipchuk, S. P.; Monje, A.; Jiao, Y.; Hao, J.; Kruger, L.; Flanagan, C. L.; Hollister, S. J.; Giannobile, W. V. Integration of 3D Printed and Micropatterned Polycaprolactone Scaffolds for Guidance of Oriented Collagenous Tissue Formation In Vivo. *Adv Healthc Mater* **2016**, *5* (6), 676–687. https://doi.org/10.1002/adhm.201500758.

(16) Corey, J. M.; Lin, D. Y.; Mycek, K. B.; Chen, Q.; Samuel, S.; Feldman, E. L.; Martin, D. C. Aligned Electrospun Nanofibers Specify the Direction of Dorsal Root Ganglia Neurite Growth. *Journal of Biomedical Materials Research Part A* **2007**, *83A* (3), 636–645. https://doi.org/10.1002/jbm.a.31285.

(17) Yang, M.; Gao, X.; Shen, Z.; Shi, X.; Lin, Z. Gelatin-Assisted Conglutination of Aligned Polycaprolactone Nanofilms into a Multilayered Fibre-Guiding Scaffold for Periodontal Ligament Regeneration. *RSC Adv.* **2018**, *9* (1), 507–518. https://doi.org/10.1039/C8RA09073D.

(18) Yeasmin, S.; Ceccarelli, J.; Vigen, M.; Carrion, B.; Putnam, A. J.; Tarle, S. A.; Kaigler, D. Stem Cells Derived from Tooth Periodontal Ligament Enhance Functional Angiogenesis by Endothelial Cells. *Tissue Eng Part A* **2014**, *20* (7–8), 1188–1196. https://doi.org/10.1089/ten.tea.2013.0512.

(19) Chen, H.; Yang, H.; Weir, M. D.; Schneider, A.; Ren, K.; Homayounfar, N.; Oates, T. W.; Zhang, K.; Liu, J.; Hu, T.; Xu, H. H. K. An Antibacterial and Injectable

Calcium Phosphate Scaffold Delivering Human Periodontal Ligament Stem Cells for Bone Tissue Engineering. *RSC Adv.* **2020**, *10* (66), 40157–40170. https://doi.org/10.1039/D0RA06873J.

(20) Zhao, Z.; Liu, J.; Weir, M. D.; Zhang, N.; Zhang, L.; Xie, X.; Zhang, C.; Zhang, K.; Bai, Y.; Xu, H. H. K. Human Periodontal Ligament Stem Cells on Calcium Phosphate Scaffold Delivering Platelet Lysate to Enhance Bone Regeneration. *RSC Adv.* **2019**, *9* (70), 41161–41172. https://doi.org/10.1039/C9RA08336G.

(21) Lee, C. H.; Shin, H. J.; Cho, I. H.; Kang, Y.-M.; Kim, I. A.; Park, K.-D.; Shin, J.-W. Nanofiber Alignment and Direction of Mechanical Strain Affect the ECM Production of Human ACL Fibroblast. *Biomaterials* **2005**, *26* (11), 1261–1270. https://doi.org/10.1016/j.biomaterials.2004.04.037.

(22) Park, C. H.; Rios, H. F.; Jin, Q.; Sugai, J. V.; Padial-Molina, M.; Taut, A. D.; Flanagan, C. L.; Hollister, S. J.; Giannobile, W. V. Tissue Engineering Bone-Ligament Complexes Using Fiber-Guiding Scaffolds. *Biomaterials* **2012**, *33* (1), 137–145. https://doi.org/10.1016/j.biomaterials.2011.09.057.

(23) Andersson, A.-S.; Bäckhed, F.; von Euler, A.; Richter-Dahlfors, A.; Sutherland, D.; Kasemo, B. Nanoscale Features Influence Epithelial Cell Morphology and Cytokine Production. *Biomaterials* **2003**, *24* (20), 3427–3436. https://doi.org/10.1016/S0142-9612(03)00208-4.

(24) Ingber, D. E.; Folkman, J. Mechanochemical Switching between Growth and Differentiation during Fibroblast Growth Factor-Stimulated Angiogenesis in Vitro: Role of Extracellular Matrix. *Journal of Cell Biology* **1989**, *109* (1), 317–330. https://doi.org/10.1083/jcb.109.1.317.

(25) Jiang, W.; Li, L.; Zhang, D.; Huang, S.; Jing, Z.; Wu, Y.; Zhao, Z.; Zhao, L.; Zhou, S. Incorporation of Aligned PCL–PEG Nanofibers into Porous Chitosan Scaffolds Improved the Orientation of Collagen Fibers in Regenerated Periodontium. *Acta Biomaterialia* **2015**, *25*, 240–252. https://doi.org/10.1016/j.actbio.2015.07.023.

(26) Rios, H. F.; Ma, D.; Xie, Y.; Giannobile, W. V.; Bonewald, L. F.; Conway, S. J.; Feng, J. Q. Periostin Is Essential for the Integrity and Function of the Periodontal Ligament During Occlusal Loading in Mice. *Journal of Periodontology* **2008**, *79* (8), 1480–1490. https://doi.org/10.1902/jop.2008.070624.

(27) Takimoto, A.; Kawatsu, M.; Yoshimoto, Y.; Kawamoto, T.; Seiryu, M.; Takano-Yamamoto, T.; Hiraki, Y.; Shukunami, C. Scleraxis and Osterix Antagonistically Regulate Tensile Force-Responsive Remodeling of the Periodontal Ligament and Alveolar Bone. *Development* **2015**, *142* (4), 787–796. https://doi.org/10.1242/dev.116228.

(28) Yu, N.; Prodanov, L.; Riet, J. te; Yang, F.; Walboomers, X. F.; Jansen, J. A. Regulation of Periodontal Ligament Cell Behavior by Cyclic Mechanical Loading and Substrate Nanotexture. *Journal of Periodontology* **2013**, *84* (10), 1504–1513. https://doi.org/10.1902/jop.2012.120513.

(29) McBeath, R.; Pirone, D. M.; Nelson, C. M.; Bhadriraju, K.; Chen, C. S. Cell Shape, Cytoskeletal Tension, and RhoA Regulate Stem Cell Lineage Commitment. *Dev. Cell* **2004**, *6* (4), 483–495.

(30) Yin, Z.; Chen, X.; Chen, J. L.; Shen, W. L.; Hieu Nguyen, T. M.; Gao, L.; Ouyang, H. W. The Regulation of Tendon Stem Cell Differentiation by the Alignment of Nanofibers. *Biomaterials* **2010**, *31* (8), 2163–2175. https://doi.org/10.1016/j.biomaterials.2009.11.083.

(31) Pilipchuk, S. P.; Fretwurst, T.; Yu, N.; Larsson, L.; Kavanagh, N. M.; Asa'ad, F.; Cheng, K. C. K.; Lahann, J.; Giannobile, W. V. Micropatterned Scaffolds with Immobilized Growth Factor Genes Regenerate Bone and Periodontal Ligament-Like Tissues. *Adv Healthc Mater* **2018**, *7* (22), e1800750. https://doi.org/10.1002/adhm.201800750.

(32) Mariani, E.; Lisignoli, G.; Borzì, R. M.; Pulsatelli, L. Biomaterials: Foreign Bodies or Tuners for the Immune Response? *Int J Mol Sci* **2019**, *20* (3). https://doi.org/10.3390/ijms20030636.

(33) Velnar, T.; Bunc, G.; Klobucar, R.; Gradisnik, L. Biomaterials and Host versus Graft Response: A Short Review. *Bosn J Basic Med Sci* **2016**, *16* (2), 82–90. https://doi.org/10.17305/bjbms.2016.525.

(34) Anderson, J. M.; Rodriguez, A.; Chang, D. T. FOREIGN BODY REACTION TO BIOMATERIALS. *Semin Immunol* **2008**, *20* (2), 86–100. https://doi.org/10.1016/j.smim.2007.11.004.

(35) Sheikh, Z.; Brooks, P. J.; Barzilay, O.; Fine, N.; Glogauer, M. Macrophages, Foreign Body Giant Cells and Their Response to Implantable Biomaterials. *Materials (Basel)* **2015**, *8* (9), 5671–5701. https://doi.org/10.3390/ma8095269.

(36) Wang, L.; Guan, N.; Jin, Y.; Lin, X.; Gao, H. Subcutaneous Vaccination with Porphyromonas Gingivalis Ameliorates Periodontitis by Modulating Th17/Treg Imbalance in a Murine Model. *International Immunopharmacology* **2015**, *25* (1), 65–73. https://doi.org/10.1016/j.intimp.2015.01.007.

(37) Napimoga, M. H.; Silva, C. A. T. da; Carregaro, V.; Farnesi-de-Assunção, T. S.; Duarte, P. M.; Melo, N. F. S. de; Fraceto, L. F. Exogenous Administration of 15d-PGJ2–Loaded Nanocapsules Inhibits Bone Resorption in a Mouse Periodontitis Model. *The Journal of Immunology* **2012**, *189* (2), 1043–1052. https://doi.org/10.4049/jimmunol.1200730.

(38) Cafferata, E. A.; Alvarez, C.; Diaz, K. T.; Maureira, M.; Monasterio, G.; González, F. E.; Covarrubias, C.; Vernal, R. Multifunctional Nanocarriers for the Treatment of Periodontitis: Immunomodulatory, Antimicrobial, and Regenerative Strategies. *Oral Dis* **2019**, *25* (8), 1866–1878. https://doi.org/10.1111/odi.13023.

(39) Zhuang, Z.; Yoshizawa-Smith, S.; Glowacki, A.; Maltos, K.; Pacheco, C.; Shehabeldin, M.; Mulkeen, M.; Myers, N.; Chong, R.; Verdelis, K.; Garlet, G. P.; Little, S.; Sfeir, C. Induction of M2 Macrophages Prevents Bone Loss in Murine Periodontitis Models. *J Dent Res* **2019**, *98* (2), 200–208. https://doi.org/10.1177/0022034518805984.

(40) Ni, C.; Zhou, J.; Kong, N.; Bian, T.; Zhang, Y.; Huang, X.; Xiao, Y.; Yang, W.; Yan, F. Gold Nanoparticles Modulate the Crosstalk between Macrophages and Periodontal Ligament Cells for Periodontitis Treatment. *Biomaterials* **2019**, *206*, 115–132. https://doi.org/10.1016/j.biomaterials.2019.03.039.

(41) Ariganello, M. B.; Simionescu, D. T.; Labow, R. S.; Lee, J. M. Macrophage Differentiation and Polarization on a Decellularized Pericardial Biomaterial. *Biomaterials* **2011**, *32* (2), 439–449. https://doi.org/10.1016/j.biomaterials.2010.09.004.

(42) McWhorter, F. Y.; Wang, T.; Nguyen, P.; Chung, T.; Liu, W. F. Modulation of Macrophage Phenotype by Cell Shape. *PNAS* **2013**, *110* (43), 17253–17258. https://doi.org/10.1073/pnas.1308887110.

(43) Wu, C.-H.; Chen, T.-L.; Chen, T.-G.; Ho, W.-P.; Chiu, W.-T.; Chen, R.-M. Nitric Oxide Modulates Pro- and Anti-Inflammatory Cytokines in Lipopolysaccharide-Activated Macrophages. *Journal of Trauma and Acute Care Surgery* **2003**, *55* (3), 540–545. https://doi.org/10.1097/01.TA.0000033496.62796.3B.

(44) Fiorentino, D. F.; Zlotnik, A.; Vieira, P.; Mosmann, T. R.; Howard, M.; Moore, K. W.; O'Garra, A. IL-10 Acts on the Antigen-Presenting Cell to Inhibit Cytokine Production by Th1 Cells. *J Immunol* **1991**, *146* (10), 3444–3451.

(45) Oswald, I. P.; Wynn, T. A.; Sher, A.; James, S. L. Interleukin 10 Inhibits Macrophage Microbicidal Activity by Blocking the Endogenous Production of Tumor Necrosis Factor Alpha Required as a Costimulatory Factor for Interferon Gamma-Induced Activation. *Proc Natl Acad Sci U S A* **1992**, *89* (18), 8676–8680. https://doi.org/10.1073/pnas.89.18.8676.

(46) Saino, E.; Focarete, M. L.; Gualandi, C.; Emanuele, E.; Cornaglia, A. I.; Imbriani, M.; Visai, L. Effect of Electrospun Fiber Diameter and Alignment on Macrophage Activation and Secretion of Proinflammatory Cytokines and Chemokines. *Biomacromolecules* **2011**, *12* (5), 1900–1911. https://doi.org/10.1021/bm200248h.

(47) Atri, C.; Guerfali, F. Z.; Laouini, D. Role of Human Macrophage Polarization in Inflammation during Infectious Diseases. *Int J Mol Sci* **2018**, *19* (6). https://doi.org/10.3390/ijms19061801.

(48) A, A.; A, G.; M, N.; Ó, C.; Ja, P.; E, E. Control of Microenvironmental Cues with a Smart Biomaterial Composite Promotes Endothelial Progenitor Cell Angiogenesis. *Eur Cell Mater* **2012**, *24*, 90–106; discussion 106. https://doi.org/10.22203/ecm.v024a07.

(49) Barbeck, M.; Serra, T.; Booms, P.; Stojanovic, S.; Najman, S.; Engel, E.; Sader, R.; Kirkpatrick, C. J.; Navarro, M.; Ghanaati, S. Analysis of the in Vitro Degradation and the in Vivo Tissue Response to Bi-Layered 3D-Printed Scaffolds Combining PLA and Biphasic PLA/Bioglass Components – Guidance of the Inflammatory Response as Basis for Osteochondral Regeneration. *Bioactive Materials* **2017**, *2* (4), 208–223. https://doi.org/10.1016/j.bioactmat.2017.06.001.

(50) Singh, S.; Wu, B. M.; Dunn, J. C. Y. Delivery of VEGF Using Collagen-Coated Polycaprolactone Scaffolds Stimulate Angiogenesis. *J Biomed Mater Res A* **2012**, *100* (3), 720–727. https://doi.org/10.1002/jbm.a.34010.

(51) Yang, M.; Gao, X.; Shen, Z.; Shi, X.; Lin, Z. Gelatin-Assisted Conglutination of Aligned Polycaprolactone Nanofilms into a Multilayered Fibre-Guiding Scaffold for Periodontal Ligament Regeneration. *RSC Adv.* **2018**, *9* (1), 507–518. https://doi.org/10.1039/C8RA09073D.

(52) Abbasi, N.; Lee, R. S. B.; Ivanovski, S.; Love, R. M.; Hamlet, S. In Vivo Bone Regeneration Assessment of Offset and Gradient Melt Electrowritten (MEW) PCL Scaffolds. *Biomaterials Research* **2020**, *24* (1), 17. https://doi.org/10.1186/s40824-020-00196-1.

(53) Carter, S.-S. D.; Costa, P. F.; Vaquette, C.; Ivanovski, S.; Hutmacher, D. W.; Malda, J. Additive Biomanufacturing: An Advanced Approach for Periodontal Tissue Regeneration. *Ann Biomed Eng* **2017**, *45* (1), 12–22. https://doi.org/10.1007/s10439-016-1687-2.

(54) Visser, J.; Melchels, F. P. W.; Jeon, J. E.; van Bussel, E. M.; Kimpton, L. S.; Byrne, H. M.; Dhert, W. J. A.; Dalton, P. D.; Hutmacher, D. W.; Malda, J. Reinforcement of Hydrogels Using Three-Dimensionally Printed Microfibres. *Nature Communications* **2015**, *6* (1), 1–10. https://doi.org/10.1038/ncomms7933.

(55) Dominici, M.; Le Blanc, K.; Mueller, I.; Slaper-Cortenbach, I.; Marini, F.; Krause, D.; Deans, R.; Keating, A.; Prockop, D.; Horwitz, E. Minimal Criteria for Defining Multipotent Mesenchymal Stromal Cells. The International Society for Cellular Therapy Position Statement. *Cytotherapy* **2006**, *8* (4), 315–317. https://doi.org/10.1080/14653240600855905.

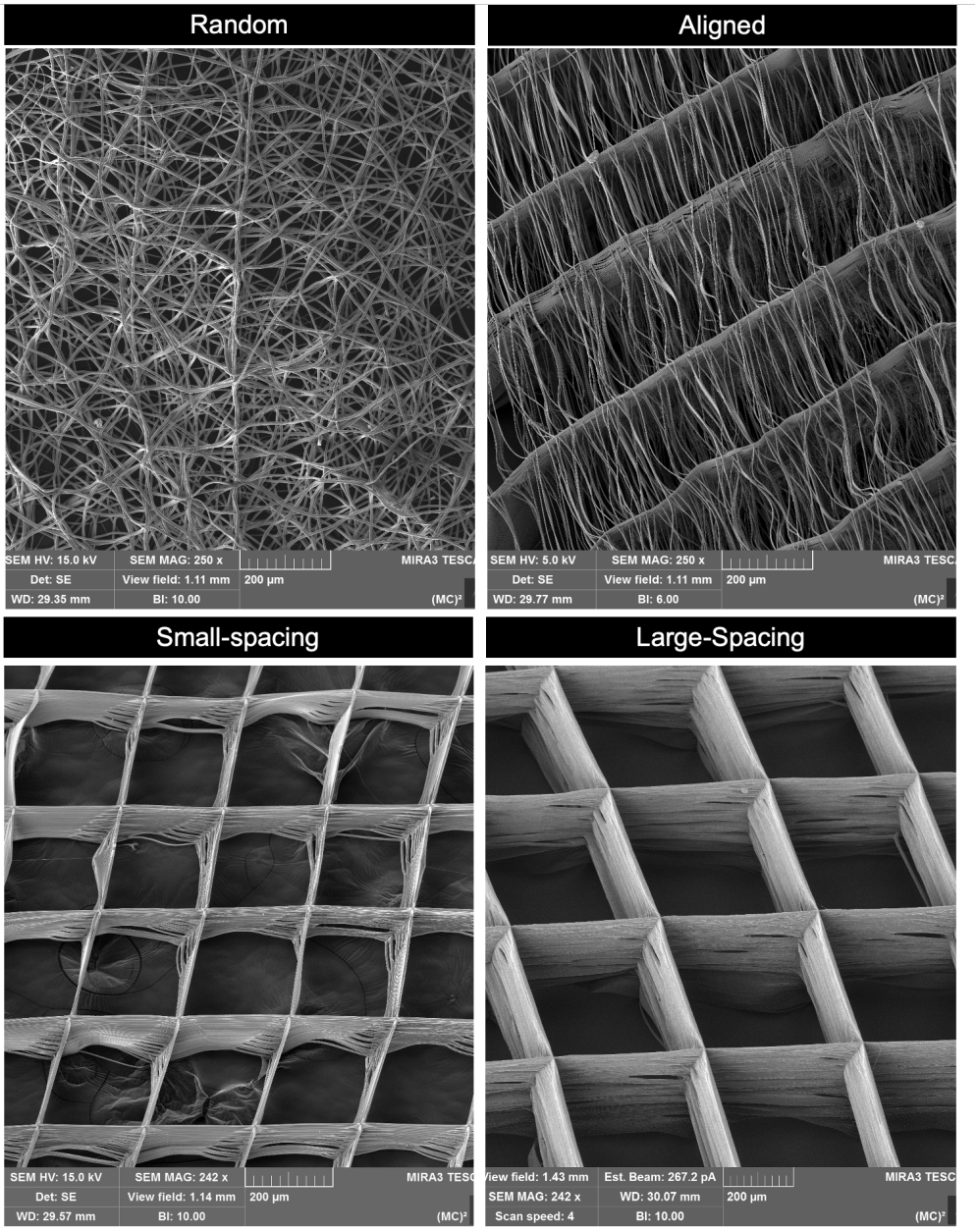

Figure 4.1 Representative SEM images of the various MEW PCL scaffolds show random, well-aligned and non-aligned scaffolds of 250 µm and 500 µm strands spacing at 0°/90°-crosshatch pattern.

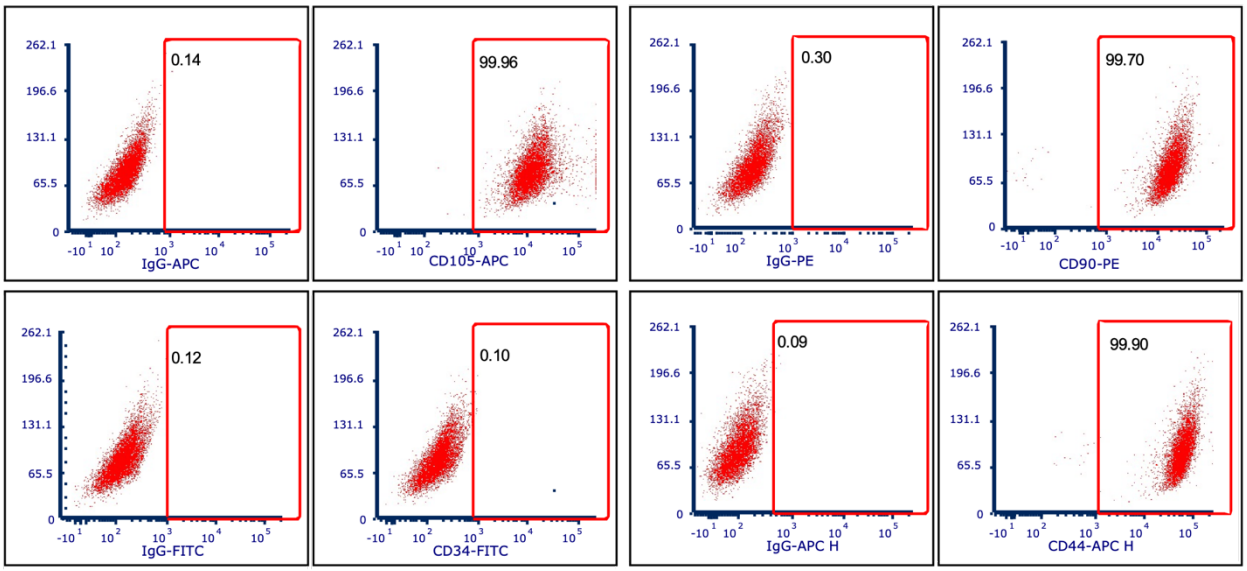

Figure 4.2 Characterizations of human periodontal ligament stem cells (hPDLSCs) via flow cytometry

hPDLSCs show positive expression for MSC markers CD90, CD105, and CD44, but negative expression for the hematopoietic marker CD34. The expression for CD90, CD105, CD44, and CD34 were 99.70%, 99.96%, 99.9%, and 0.10%, respectively.

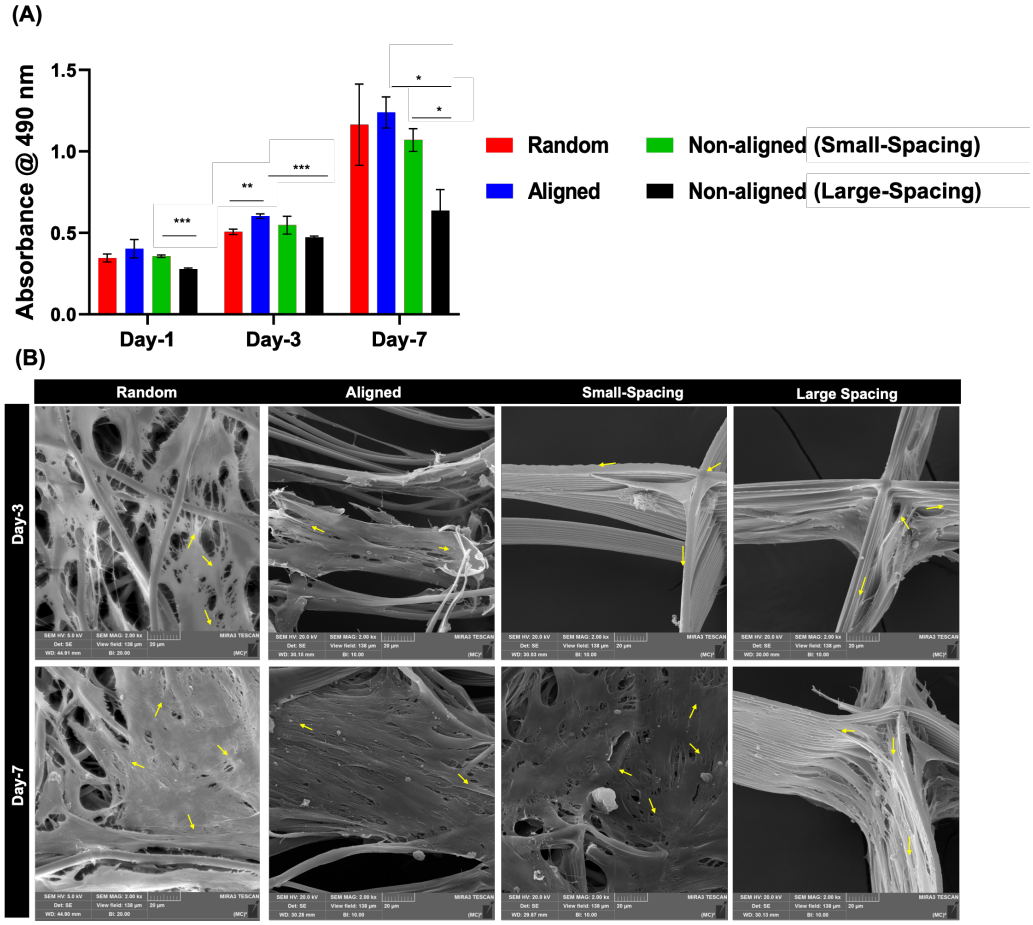

Figure 4-3 Attachment and proliferation of hPDLSCs on MEW PCL scaffolds with aligned and randomly oriented fiber configurations, and 250 µm and 500 µm strand spacings

(a) Cell viability of hPDLSCs seeded on the scaffolds using AlamarBlue assay over 7 days. **(b)** Representative SEM images of hPDLSCs proliferation on the scaffolds after 3 and 7 days. Note the characteristic cell spreading along the fibrous walls. A more pronounced spreading was detected along the scaffolds with randomly oriented fibers (white arrows indicate direction of filopodia protrusion). (Mean±SD, n=3). *p<0.05, **p<0.01, ***p<0.001.

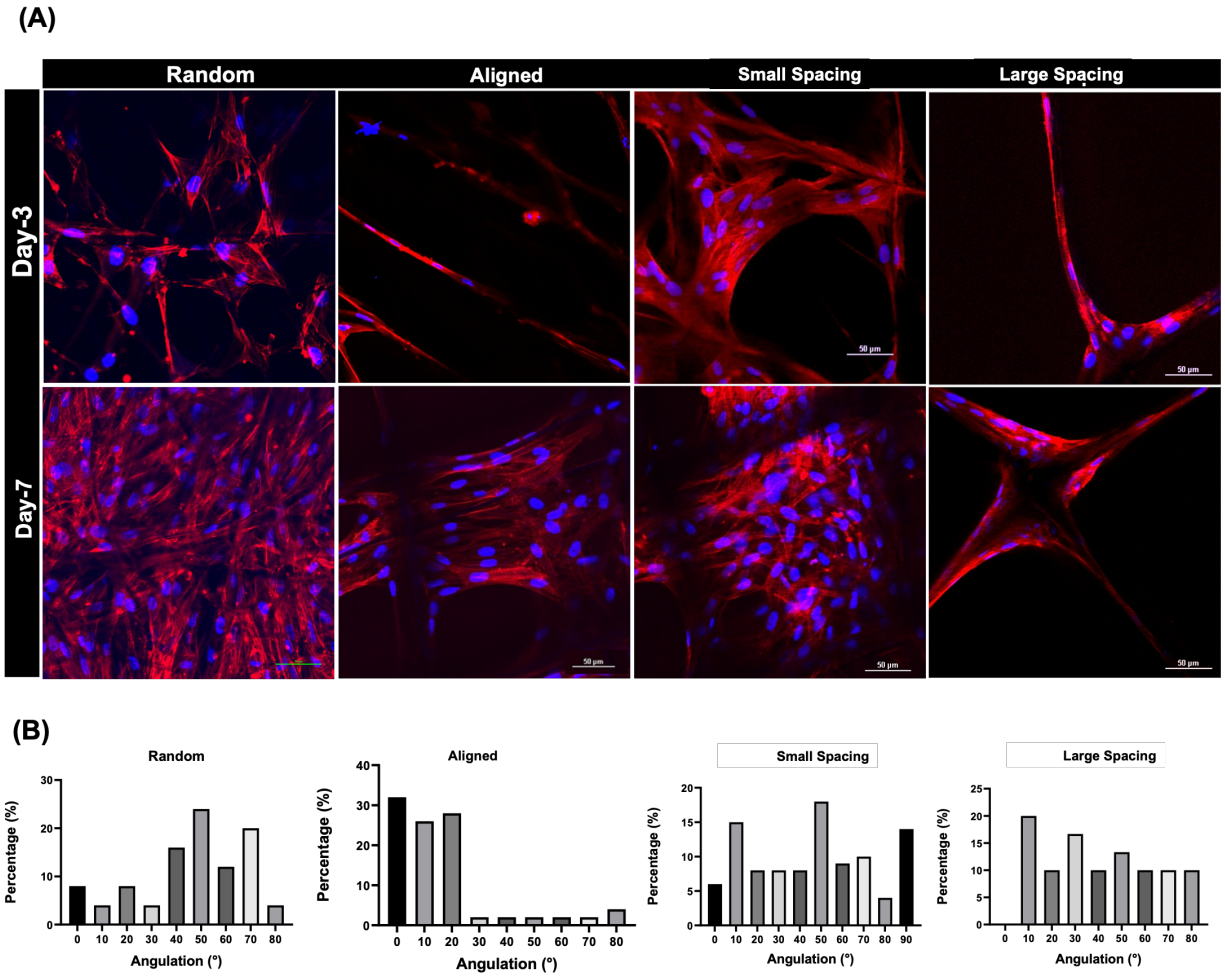

Figure 4-4 Patterns of alignment of Periodontal Ligament Cells on designated scaffolds

(a) Representative CLSM images show a variable pattern of cells' bridging, following the fibers' arrangements at day 3 and 7. DAPI (blue) and phalloidin (red) fluorescent staining (scale bar = 100 µm). **(b)** Histograms of PDLSCs nucleus angulation on scaffolds with aligned and randomly oriented fiber configurations as well as crosshatch 0/90 arrangement and 250 µm and 500 µm strand spacings corresponding to confocal images.

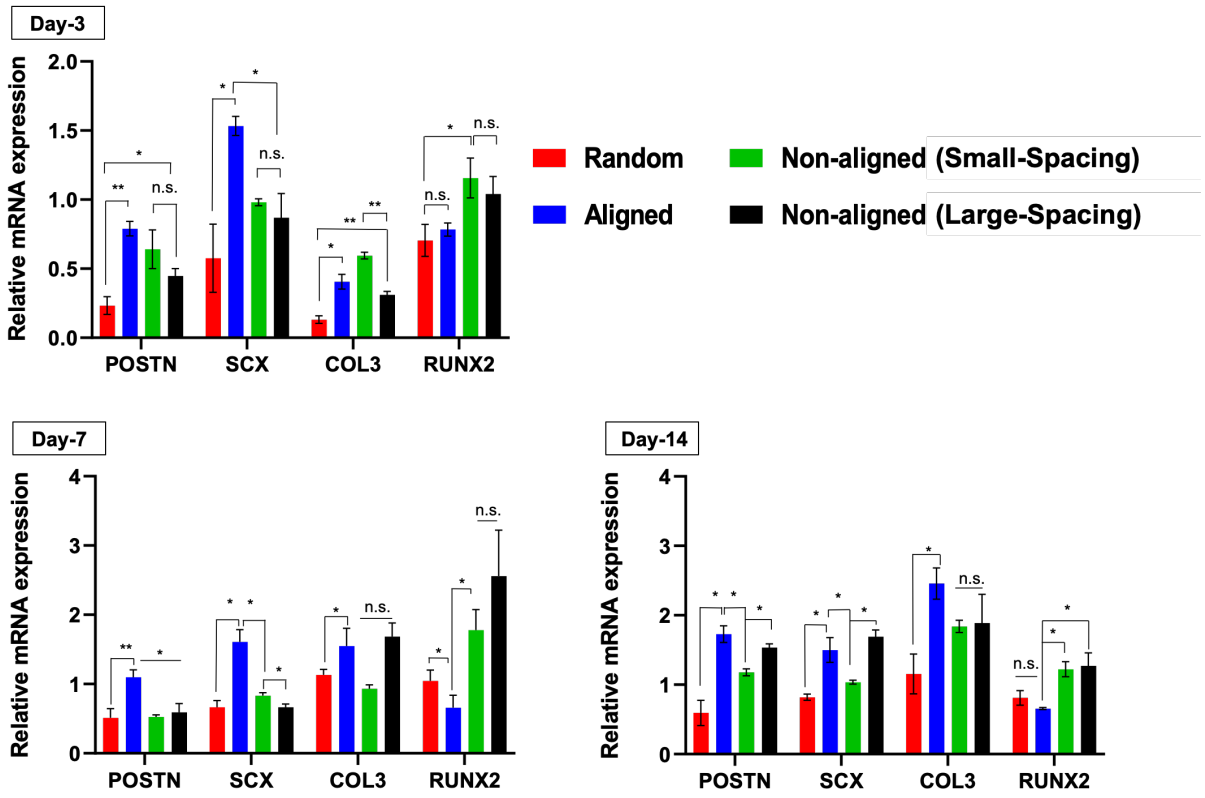

Figure 4-5 Ligamentogenic and osteogenic differentiation of hPDLSCs seeded on the various MEW PCL scaffolds

The mRNA levels at days 3, 7, and 14 of selected ligamentogenic genes (*i.e.*, periostin, Scleraxis, and Col3) were significantly higher in scaffolds with aligned fibers, whereas an osteogenic marker (Runx2) was significantly higher in crosshatch 0/90 scaffolds with 250 μm and 500 μm strand spacing. (Mean±SD, n=4). *p<0.05, **p<0.01.

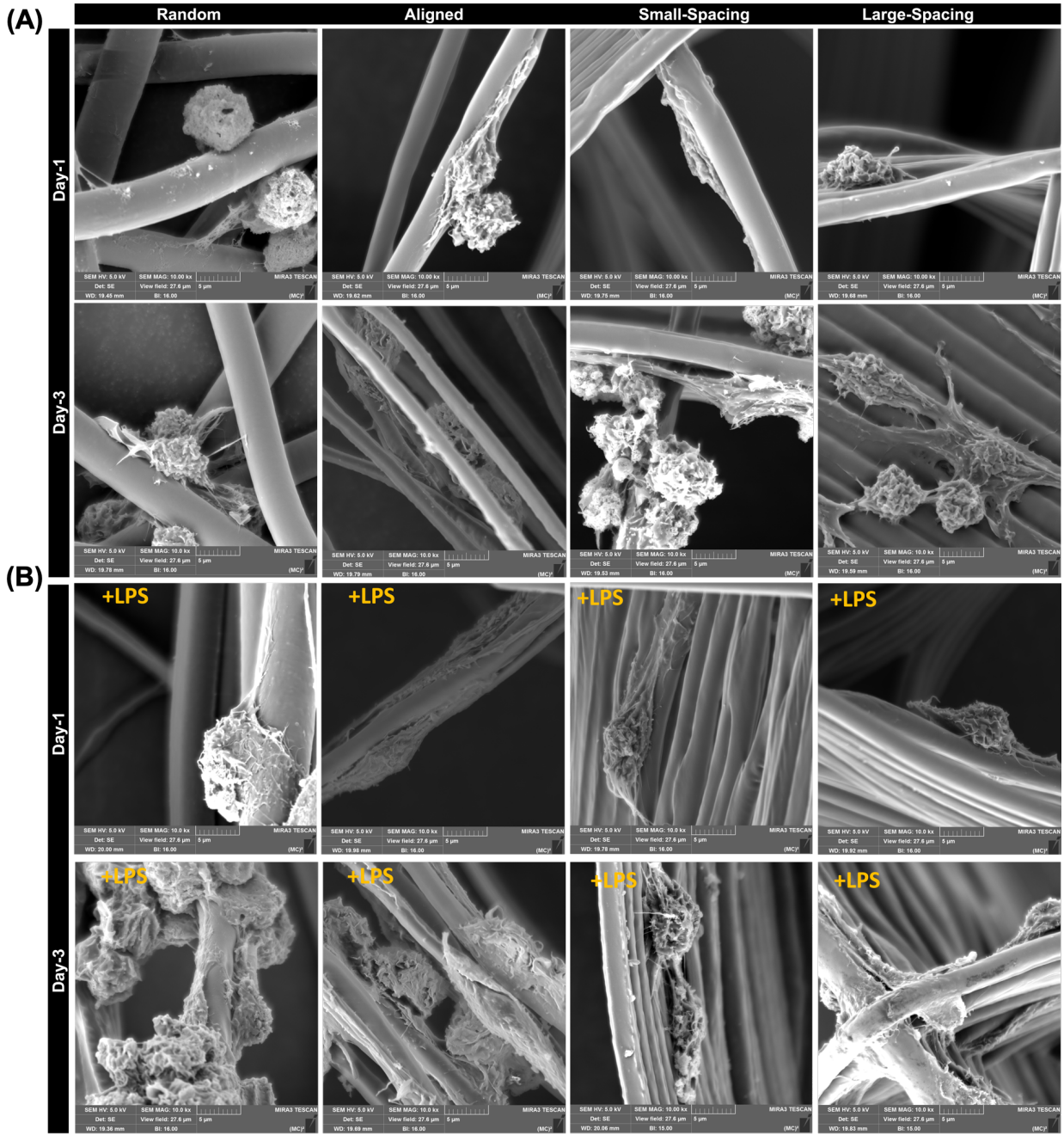

Figure 4-6 Representative SEM images showing RAW 264.7 cells' morphology of spontaneously differentiated and LPS-stimulated macrophages on scaffolds with varying fiber orientation *i.e.,* random, well-aligned and non-aligned scaffolds of 250 µm and 500 µm strands spacing at 0°/90°-oriented junctions

The images show mixed pattern of macrophages spreading, the round shape typical for M1 and more pronounced elongated pattern typical for M2 phenotype.

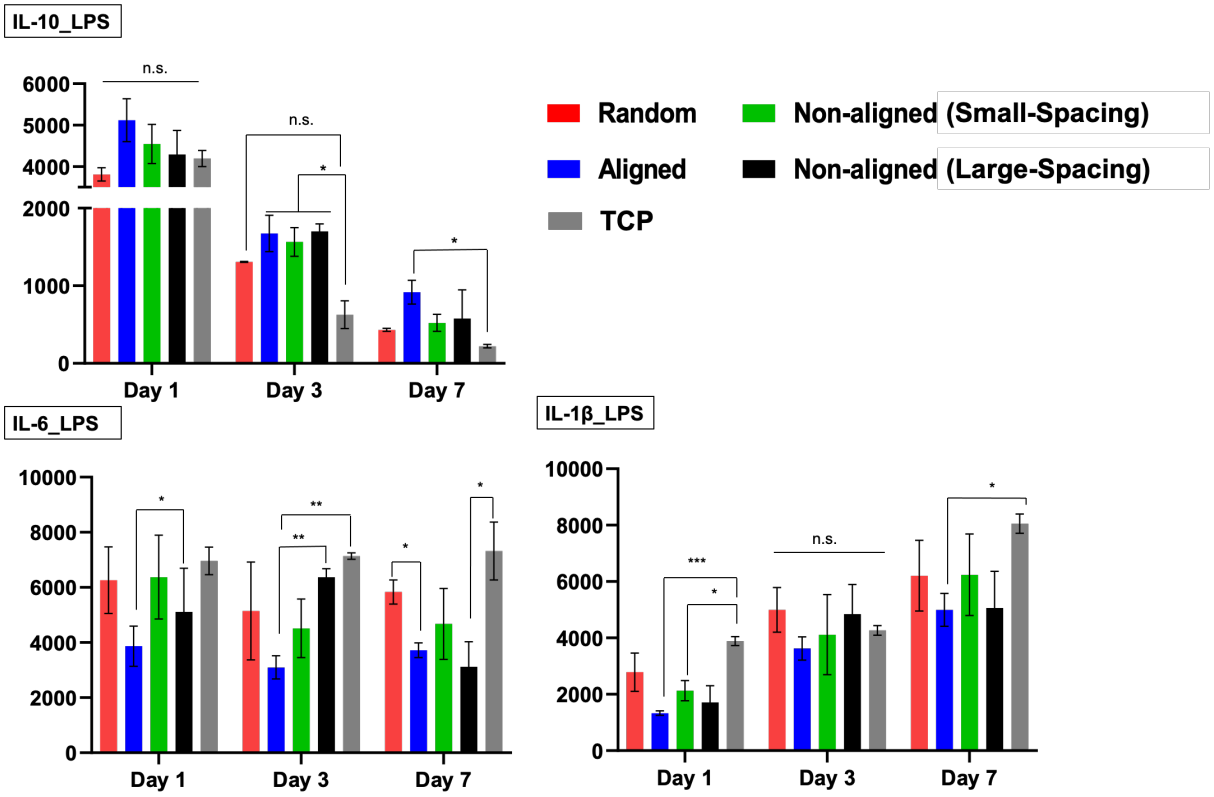

Figure 4-7 Cytokine release of LPS-stimulated macrophages on scaffolds with different fibers orientation/configurations

Released cytokines were measured using supernatants extracted after culturing macrophages on different scaffolds, and they were compared to control TCP over 7 days. (Mean ± SD, n=3). *p<0.05; **p<0.01, ***p<0.001.

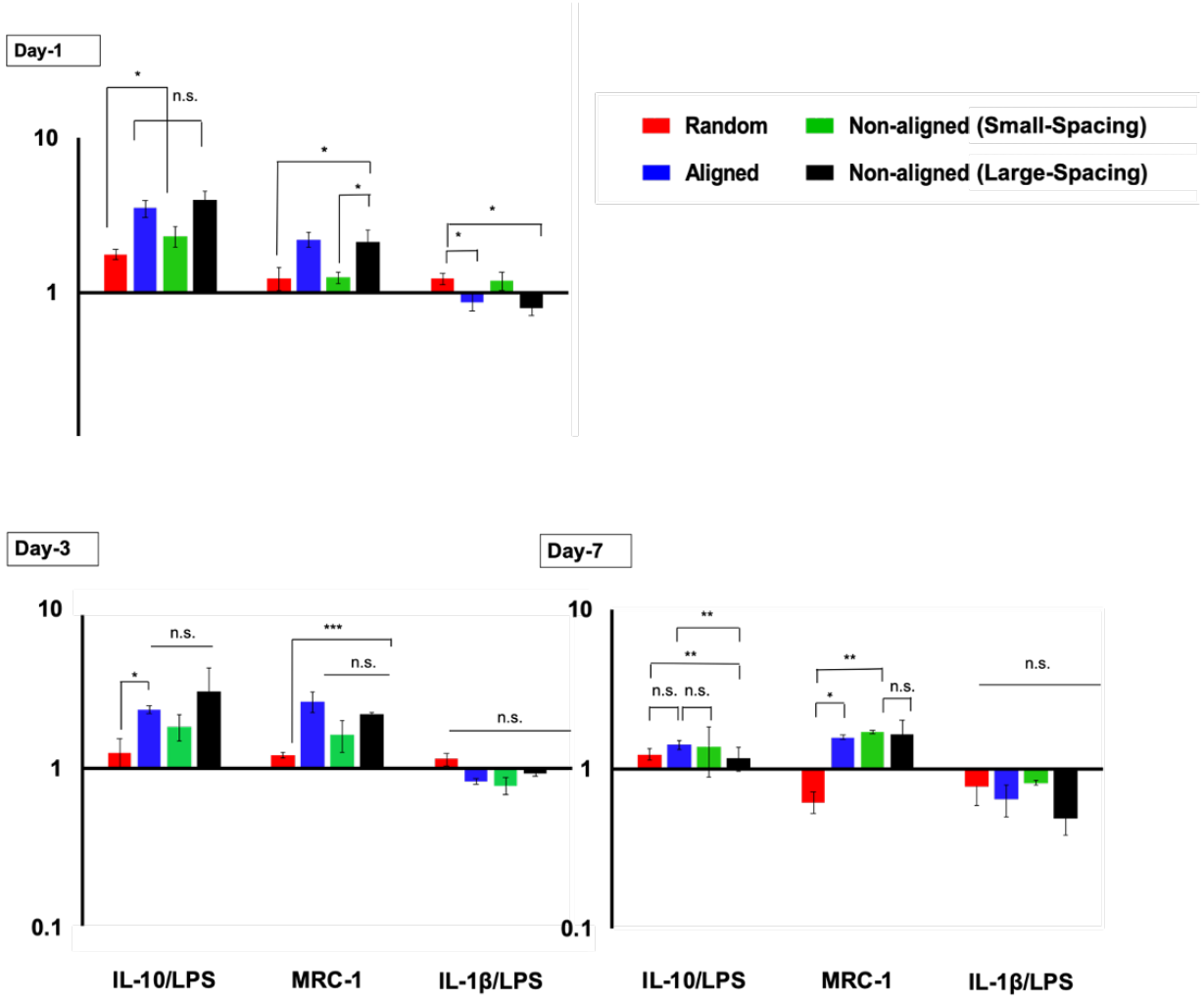

Figure 4-8 Gene expression profile of LPS-stimulated macrophages, the level of IL-10, MRC1 and IL-1β

Expression of specific markers was measured using qPCR for M1, IL-1β and IL-6 and for M2, IL-10 over 7 days; data was compared to TCP as reference sample. (Mean ± SD, n=3). *p<0.05; **p<0.01, ***p<0.001.

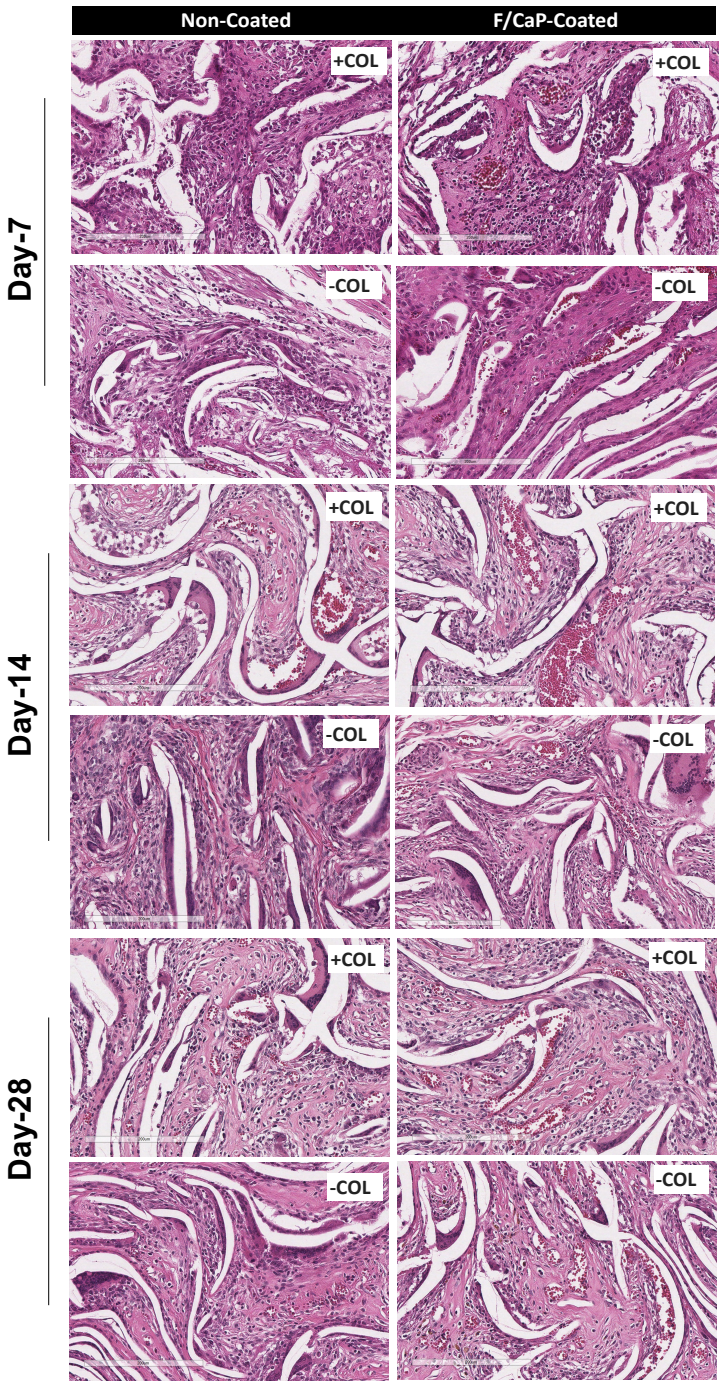

Figure 4-9 Representative H&E staining and histological analysis of the implanted scaffolds, namely F/CaP-coated, non-coated, F/CaP-coated_collagen, non-*coated collagen*, after 7, 14, and 28 days *in vivo* (20× [high magnification, scale bar = 200 µm]).

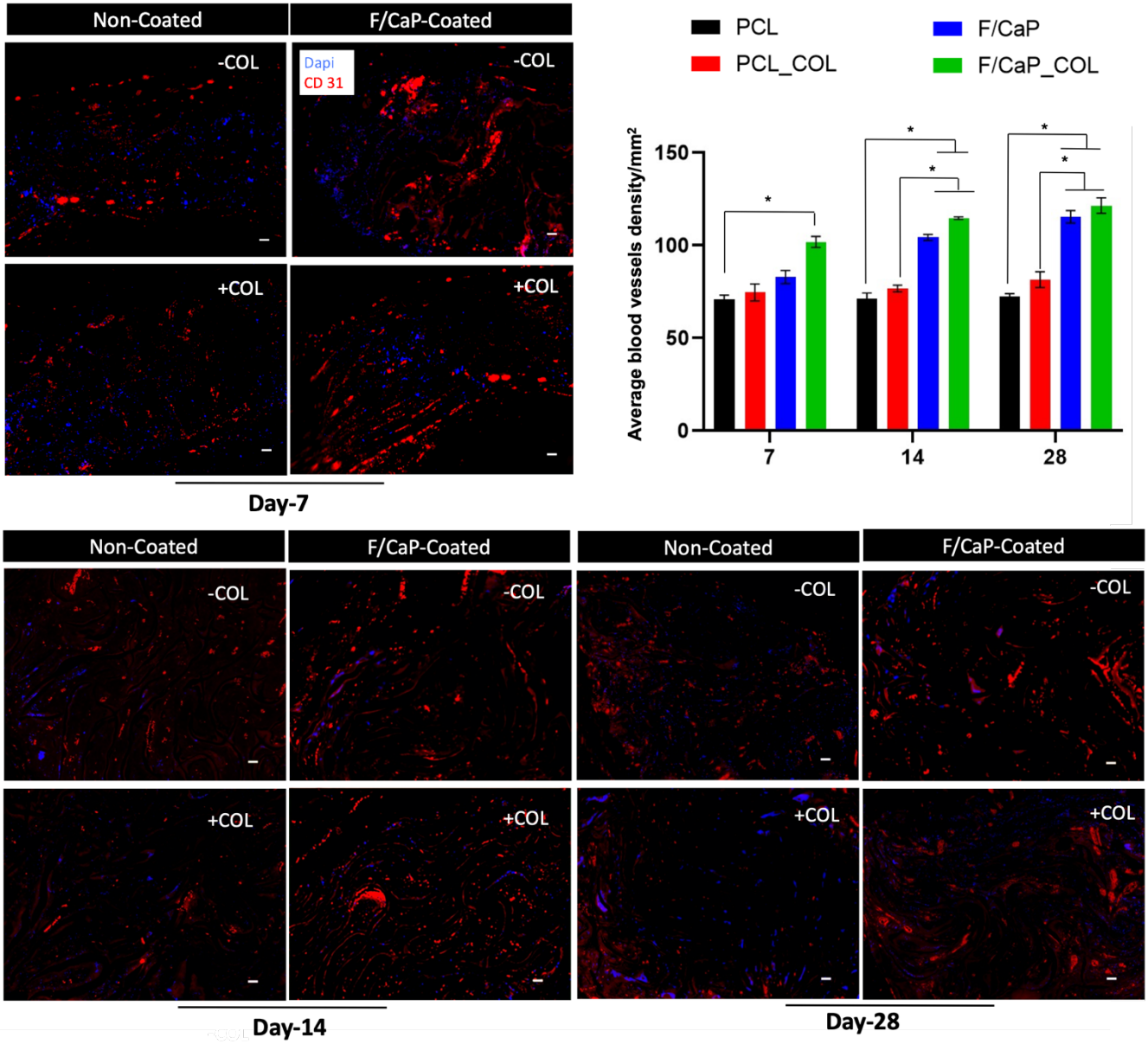

Figure 4-10 Immunofluorescence imaging of CD31/DAPI at days 7, 14, and 28
(a) Positive CD31 is in abundance in F/CaP-coated scaffolds and collagen-infused scaffolds compared to the non-coated group. Red indicates CD31, and blue indicates nuclei. Scale bar = 50 µm. **(b)** Bar graph shows the blood vessels density corresponding immunofluorescence images. Mean ± SD (n=3). ANOVA: *p<0.05.

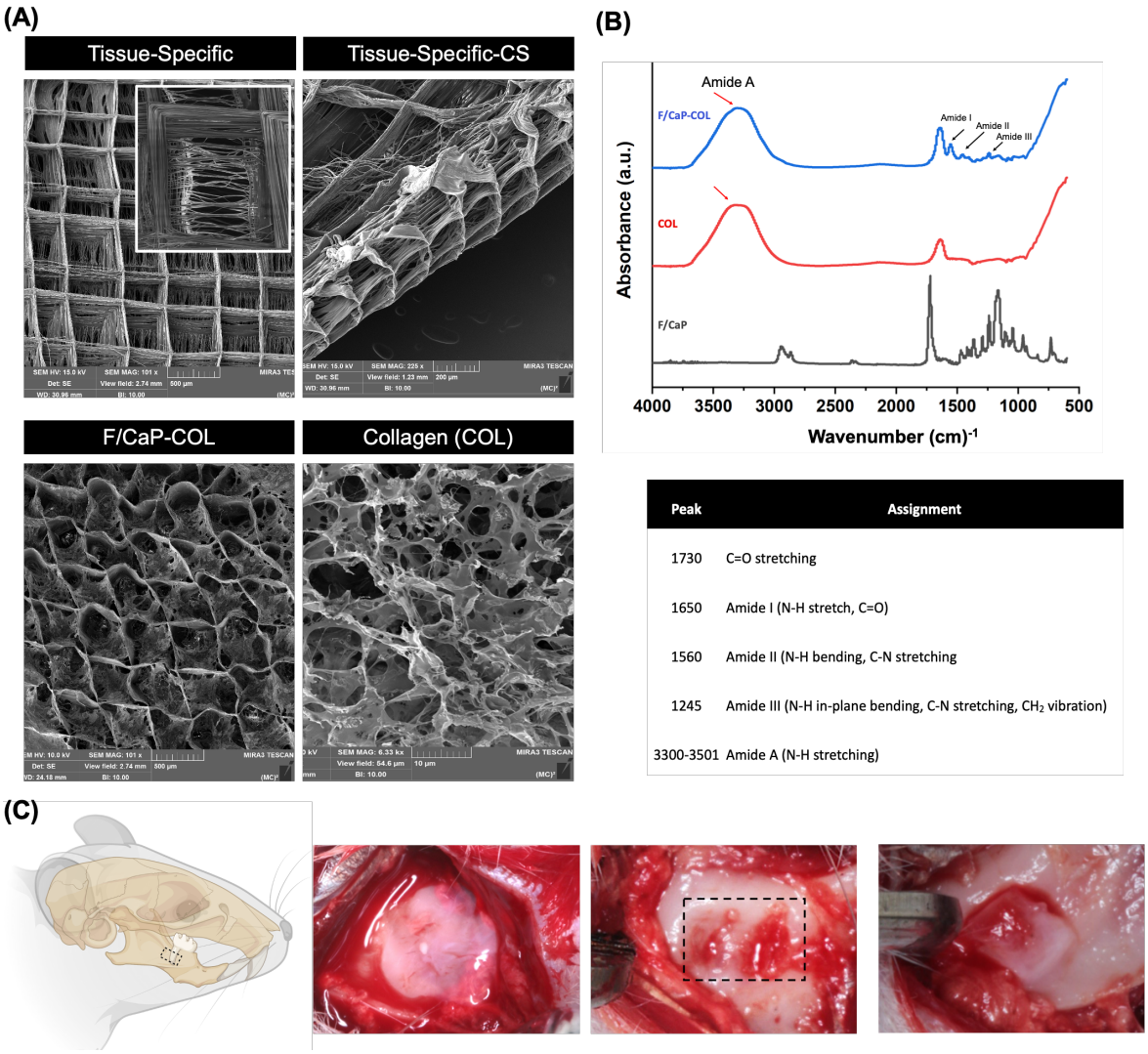

Figure 4-11 Fabrication and characterization of tissue specific scaffold
(a) Representative SEM images for tissue specific scaffold with aligned PDL compartment and 500µm strands spacing for bone compartments, and SEM images for collagen infused scaffolds. (**b)** FTIR spectra of collagen, F/CaP-coated MEW PCL scaffold, and F/CaP-coated MEW PCL scaffold infused with collagen. Data show chemical functional groups related to phosphate at ~ 565 cm^{-1} and ~ 960 cm^{-1} in F/CaP-coated scaffolds, while collagen-infused scaffolds and collagen also show the amide groups, confirming successful permeation of collagen within the MEW scaffolds. (*) indicates the presence of PCL. **(c)** Generation of the rat mandibular periodontal fenestration model. Photographs of a rat mandible after the incision, flap elevation, creation of the defect, and implantation of tissue specific scaffold in the defect region.

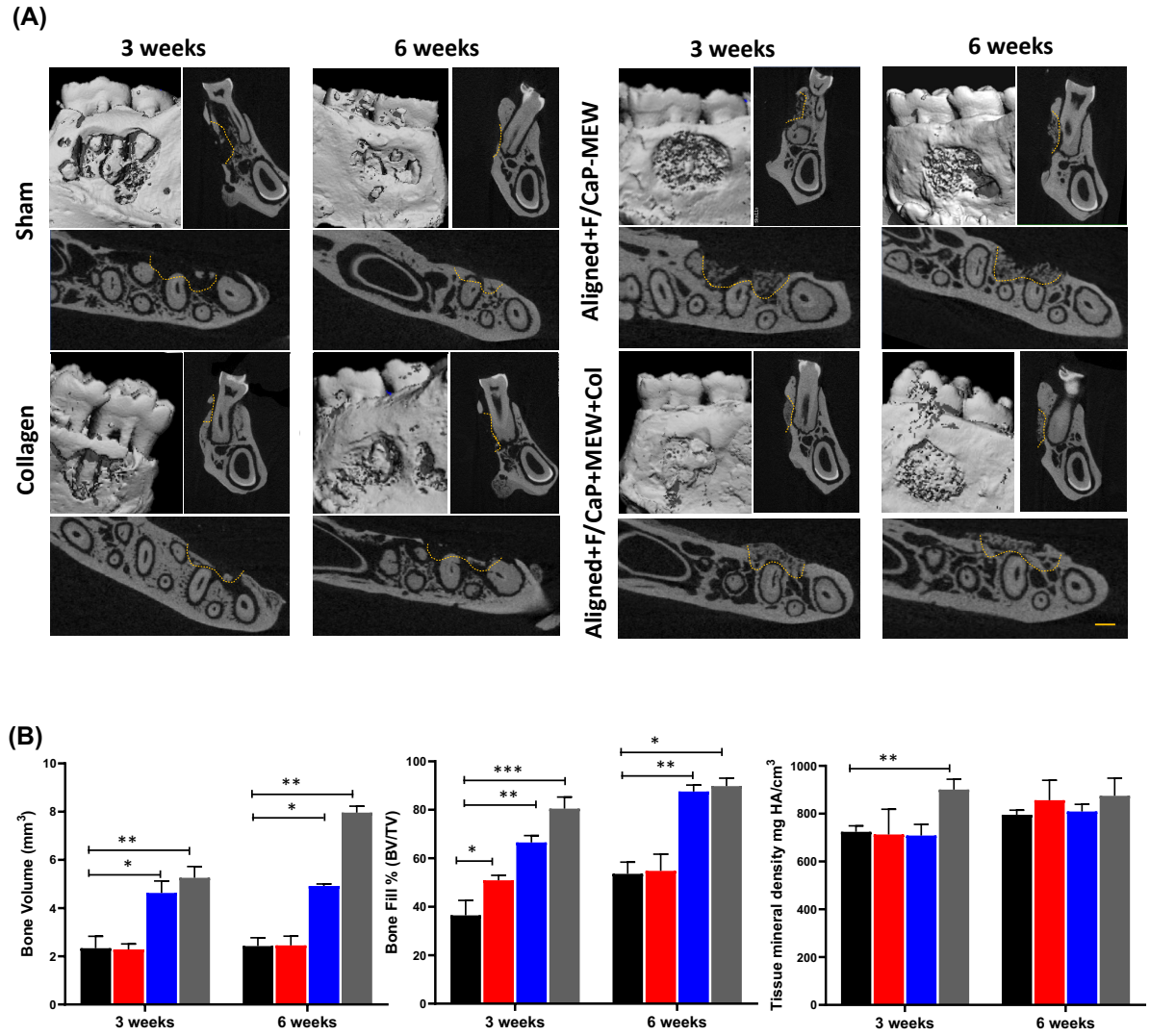

Figure 4-12 MicroCT assessment of bone formation

(a) Representative microCT images of the fenestration defect exposing the distal root of the second molar at 3 and 6 weeks in the Control (Sham), Collagen, and Biphasic scaffold with Aligned (PDL) compartment and non-coated and coated (F/CaP) and aligned and coated (F/CaP) + collagen. Transverse views highlight the visual differences between the area and density of bone regenerated within the defect. (Scale bar = 1 mm). (We need to check how we described in paper 1 these captions – Figure 11 through 14). **(b)** µCT assessments of bone volume, bone fill, and tissue mineral density at 3 and 6 weeks after surgery, within the different groups. The coated (F/CaP) group and the presence of collagen further shows significant differences for bone volume and bone fill compared to both the control and non-coated groups. Mean ± SD (n=6). ANOVA: *p<0.05; **p<0.01.

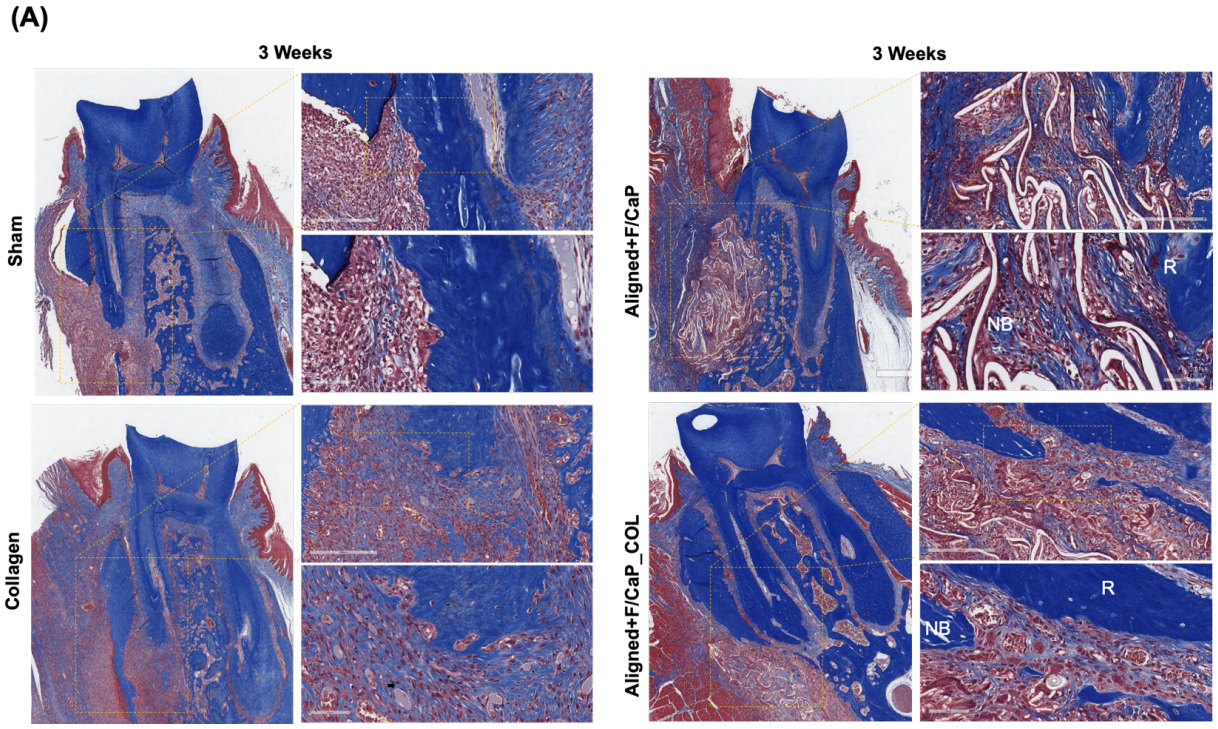
(A)
3 Weeks
3 Weeks
Sham
Collagen
Aligned+F/CaP
Aligned+F/CaP_COL
R
NB
R
NB

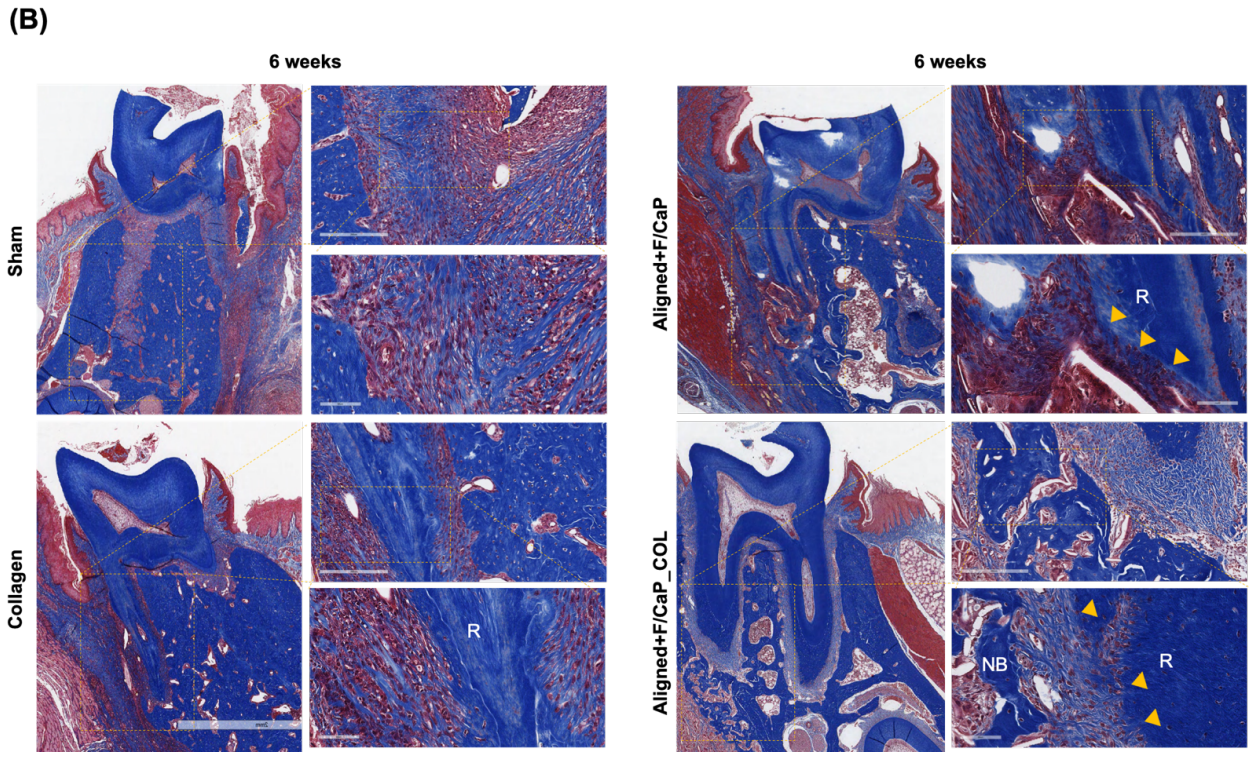

Figure 4-13 Masson's trichrome staining of scaffolds after 6 weeks *in vivo* Representative Masson's trichrome-stained horizontal cross-section of Control (Sham), Collagen, and tissue specific scaffolds with aligned fiber configuration (PDL) compartment and coated (F/CaP) fibers (bone compartment) and tissue specific scaffold infused with collagen at 3- weeks **(a)** and 6-weeks **(b)** post-implantation. Yellow dashed line highlights the area of scaffold placement and new bone formation. Yellow arrow for PDL, NB: new bone; R: Root surface.

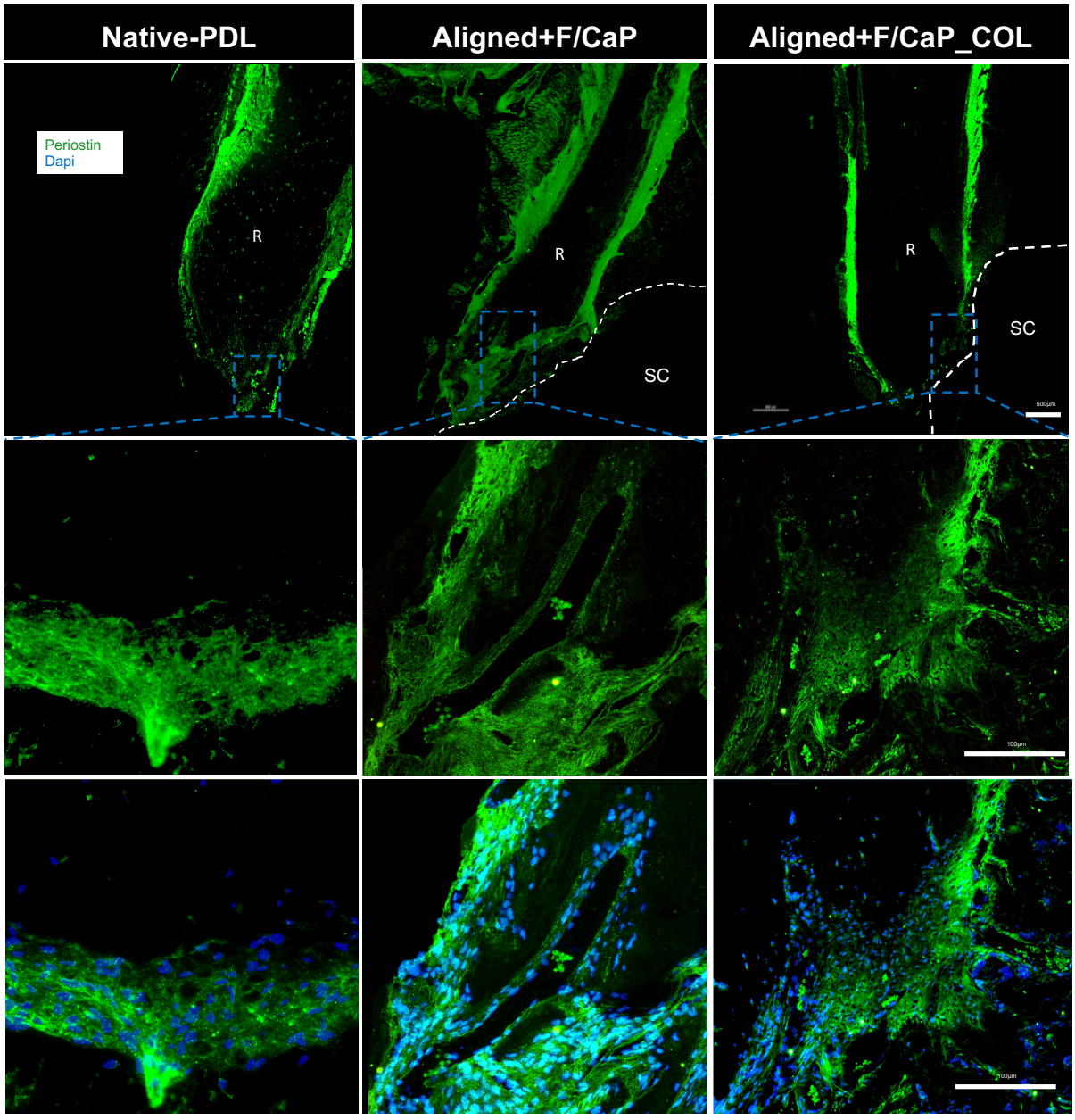

Figure 4-14 Immunofluorescence staining for the expression of periostin at the PDL space

Periostin expression profile is observed at week 6 in periodontal defects treated with aligned+F/CaP-coated and aligned+F/CaP-coated_collagen scaffolds and compared to native PDL tissues.

CHAPTER 5

Conclusions and Future Directions

5.1 Conclusions

The development of personalized and functional scaffolds is required to recapitulate the tissue-specific architecture and function of different tissues and tissue interfaces in the periodontium. While many studies have vastly explored functional materials for tissue interfaces via applying the principles of biomaterial architectures, application of growth factors, and/or the incorporation of cells, there is still a deficiency in fulfilling the necessary prerequisites to restoring tissue interfaces via cell and/or a growth factor-free approach. Moreover, most of the current literature, based on the integration of multilayers via different techniques, implies a non-continuous single-step process to create interconnectivity between the multilayers or introduce biomolecules and growth factors that suffer from sufficient bioavailability or via cells' transplantations that introduce other limitations and restricted outcomes. As described throughout the chapters, this work focuses on the use of innovative technology (melt electrowriting) that allow for the scaffold to be engineered at different configurations (*e.g.*, strand spacing, fiber orientation, among others) and for post-processing changes (*i.e.,* F/CaP coating) that introduce macro and

micro scale cues that can guide the formation of both hard and soft tissue of the periodontium via modulation of osteogenesis, ligamentogenesis, and improving vascularization and macrophage polarization.

From a clinical standpoint, although existing therapeutics can lead to some degree of tissue regeneration, low predictability, and efficacy in cases of extreme tissue destruction call for improved strategies that can better replicate the three-dimensional (3D) and multi-tissue complexity of periodontal defects.[1] Although the collective results from these studies demonstrate that the combination of electrospinning and 3D printing represents a promising approach for the fabrication of scaffolds for the regeneration of periodontal tissue interfaces, multiple techniques are required to fabricate each tissue-specific compartment, which then requires further processing steps to integrate them into a single scaffold. Precisely, no approaches are currently available to predictably regenerate defects with considerable bone loss and avoid tooth extraction. Thus, there are an emerging quest for personalized (tissue- and defect-specific) solutions that can guide the coordinated growth and development of the periodontium and the involved soft-to-hard tissue interfaces to prolong the lifetime of the patient's natural dentition.

There is clear evidence that F/CaP-coating improves the bioactivity of PCL by releasing calcium and phosphorus ions that modulate hPDLSCs' commitment toward osteogenic differentiation *in vitro*. Due to CaP's similarity to inorganic mineral phase crystals contained in bone, it has been found to modulate osteoclast and osteoblast activity.[2] As a result, calcium, and phosphate released by PCL/coated surfaces represent potent signals to trigger the osteogenic genes' expression and ALP activity in bone cells. Remarkably, F/CaP coating has shown to favorably display antimicrobial action, which,

in the case of periodontal regeneration are beneficial for preventing bacterial colonization, similar to Fluorapatite (FA)[3], and display bioactivity to favorably form bone-like apatite globules as seen in FA;[4] whereas the novel scaffold coating provides a constant source of the elements shown to provide osteogenic differentiation and antibacterial properties, both *in vitro* and *in vivo,* as described in Chapter 3. Furthermore, there is clear evidence that scaffold strands' spacing encourages cellular infiltration and blood vessels' formation, as shown using the subcutaneous model, as described in Chapter 3. Importantly, pre-clinical efficacy of the proposed strategy was determined following the classical fenestration defect model to evaluate whether the F/CaP-coated scaffolds would enhance bone regeneration while supporting physiological neoformation of the periodontal ligament (PDL) and cementum, specifically, strands spacing of 500 μm and F/CaP-coating are shown to be more significant parameters in bone formation.

Here, we believe that the highly ordered, porous MEW-F/CaP scaffold carries the properties of previously established GTR/GBR membranes for periodontal tissue regeneration.[5,6] The scaffold physically maintains the defect site and supports infiltration and attachment of host progenitors. Thus, it can support the simultaneous and coordinated growth of both soft (PDL) and hard (alveolar bone and cementum) periodontal tissues, while maintaining space for resident mesenchymal progenitors to direct regeneration of cementum (pre-cementoblasts), PDL (fibroblasts), and bone (pre-osteoblasts) with no need for a barrier membrane in a completely cell-free approach.

In Chapter 4 we continued to investigate the effects of highly-ordered tissue-specific scaffolds' architectures, where F/CaP osteoconductive scaffold stimulates alveolar bone regeneration, while aligned scaffolds serve as a guide for PDL formation

when implanted in a well-established periodontal defect model. There is clear evidence that scaffold-strands spacing and the alignment of fibers at specific configurations encourage bone and ligament formation, as shown using the periodontal fenestration defects model. More specifically, F/CaP MEW scaffold with strands spacing of 500 μm is shown to be a more significant parameter for bone compartments; whereas the unique porosity and fibers' alignments were competent to improve bone-PDL-like regeneration, which is critical to recapitulating the functional integrity of the periodontium, as described in Chapter 4.

5.2 Future Directions

Although additive manufacturing (AM) has been deployed to engineer personalized biomaterials for regenerative dental medicine, clinical studies in periodontics failed to demonstrate predictable results, even though a patient-specific scaffold was manufactured using poly(ε-caprolactone) (PCL). The bulky nature of the printed scaffold hinders the degradation rate beyond the optimum for matching those needed for periodontal tissues' regeneration.[7] Here, melt electrowriting (MEW) holds significant potential, since it allows for the generation of microscale fibers and controlled fiber deposition to ultimately create more physiologically relevant 3D scaffolds for periodontal regeneration. MEW represents a unique platform for generating defect and tissue-specific personalized scaffolds for periodontal tissue regeneration. The porous and microscale diameters of the scaffold do not compromise the overall quality of the construct and act as a barrier membrane that prevents soft tissue migration into the bone defect while maintaining space and providing a niche for resident progenitor cells from the residual

PDL, alveolar bone, and blood to recolonize the defect area and differentiate it into new periodontal apparatus.[6,8]

Collectively, the novel approach utilized in this work is the introduction of 3D-printed MEW techniques, where predesigned 3D allows for manipulating the configuration, thickness, and size of the scaffold, all referred to as personalized, and the defect-specific scaffolds-fabrication technique. Indeed, it represents the base towards the development of personalized scaffolds capable of enabling tissue-specific differentiation of progenitor cells, and thus guides the simultaneous and coordinated regenerative process.

Moreover, there are potential avenues yet to be explored to foster the outcomes of periodontal tissues' regeneration via the MEW technique. Scaffold design and the introduction of growth factors or biomolecules specific for each layer within melt electrospun constructs provide more specificity and predictably of the newly formed periodontium. Further, the convergence of multi-technique at the same setting provides a higher level of specificity, where cells'-hydrogel or biomolecules'-hydrogel simultaneous bioprinting with MEW allows for the direct incorporation of cells and bioactive molecules while supporting the integrity of the scaffolds. The single biofabrication platform using the convergence of 3D printing and bioprinting technologies enables the fabrication of scaffold systems with improved spatial control over cell positioning and biomolecules' distribution. Castilho et al. and Ruijter et al. presented such an approach via the convergence between bioprinting and MEW in a single biofabrication platform, which permitted fabrication of living constructs with the spatial distribution of mesenchymal stromal cells and improved biomechanical functionality.[10,11] Further, the combination of

existing CaP-based materials with a history of use in bone regeneration with MEW technology to guide collagenous tissue formation, is a promising venue for addressing tissue interfaces. Diloksumpan et al. presented such an approach to process a multiscale osteochondral construct processed via melt writing electrospun fibers-reinforced hydrogel-ceramic interfaces.[11] Overcoming the existing limitations at the material level or technique level through the improvement of mechanical integrity and the incorporation of bioactive molecules increases the success of predictability to guided tissue formation in complex structures.

It remains a challenge to develop mechanically competent constructs for alveolar bone regeneration using synthetic polymers with tunable biological and chemical properties.[7] The bulky nature of previously printed scaffold hinders the degradation rate beyond the optimum for matching those needed for periodontal tissues' regeneration.[7] In contrast, typically highly porous scaffolds, *i.e.,* MEW scaffolds, have the potential to increase the hydrolytic and enzymatic degradation rates of poly(α-esters) due to introducing a higher surface area, water sorption/swelling rates, and more reaction sites at the surface, which are fairly advantageous features for slow degrading polymers, such as PCL.[9]

In this work, the MEW scaffold with a fiber diameter of ~ 2.3 μm and porosity of ~ 97% has been utilized for periodontal regeneration. The *in vivo* study ranges from 3 to 6 weeks and shows remaining scaffold at the defect area that does not compromise either biocompatibility or tissue integration. Although the remaining scaffold is obvious histologically, it does not interfere with bony infill and blood vessels' ingrowth, compared

to preexisting FDM scaffolds, although the promising regenerative potential, long-term follow-up study of MEW scaffold degradation rates *in vivo* is highly recommended.

5.3 References

(1) Ivanovski, S.; Vaquette, C.; Gronthos, S.; Hutmacher, D. W.; Bartold, P. M. Multiphasic Scaffolds for Periodontal Tissue Engineering. *J Dent Res* **2014**, *93* (12), 1212–1221. https://doi.org/10.1177/0022034514544301.

(2) Vaquette, C.; Ivanovski, S.; Hamlet, S. M.; Hutmacher, D. W. Effect of Culture Conditions and Calcium Phosphate Coating on Ectopic Bone Formation. *Biomaterials* **2013**, *34* (22), 5538–5551. https://doi.org/10.1016/j.biomaterials.2013.03.088.

(3) Liu, J.; Jin, T.; Chang, S.; Czajka-Jakubowska, A.; Zhang, Z.; Nör, J. E.; Clarkson, B. H. The Effect of Novel Fluorapatite Surfaces on Osteoblast-Like Cell Adhesion, Growth, and Mineralization. *Tissue Eng Part A* **2010**, *16* (9), 2977–2986. https://doi.org/10.1089/ten.tea.2009.0632.

(4) Sikder, P.; Ferreira, J. A.; Fakhrabadi, E. A.; Kantorski, K. Z.; Liberatore, M. W.; Bottino, M. C.; Bhaduri, S. B. Bioactive Amorphous Magnesium Phosphate-Polyetheretherketone Composite Filaments for 3D Printing. *Dental Materials* **2020**, *36* (7), 865–883. https://doi.org/10.1016/j.dental.2020.04.008.

(5) Costa, P. F.; Vaquette, C.; Zhang, Q.; Reis, R. L.; Ivanovski, S.; Hutmacher, D. W. Advanced Tissue Engineering Scaffold Design for Regeneration of the Complex Hierarchical Periodontal Structure. *J. Clin. Periodontol.* **2014**, *41* (3), 283–294. https://doi.org/10.1111/jcpe.12214.

(6) Criscenti, G.; Longoni, A.; Luca, A. D.; Maria, C. D.; Blitterswijk, C. A. van; Vozzi, G.; Moroni, L. Triphasic Scaffolds for the Regeneration of the Bone–Ligament Interface. *Biofabrication* **2016**, *8* (1), 015009. https://doi.org/10.1088/1758-5090/8/1/015009.

(7) Rasperini, G.; Pilipchuk, S. P.; Flanagan, C. L.; Park, C. H.; Pagni, G.; Hollister, S. J.; Giannobile, W. V. 3D-Printed Bioresorbable Scaffold for Periodontal Repair: *Journal of Dental Research* **2015**. https://doi.org/10.1177/0022034515588303.

(8) Obregon, F.; Vaquette, C.; Ivanovski, S.; Hutmacher, D. W.; Bertassoni, L. E. Three-Dimensional Bioprinting for Regenerative Dentistry and Craniofacial Tissue

Engineering. *J Dent Res* **2015**, *94* (9 Suppl), 143S-52S. https://doi.org/10.1177/0022034515588885.

(9) Boia, R.; Dias, P. A. N.; Martins, J. M.; Galindo-Romero, C.; Aires, I. D.; Vidal-Sanz, M.; Agudo-Barriuso, M.; de Sousa, H. C.; Ambrósio, A. F.; Braga, M. E. M.; Santiago, A. R. Porous Poly(ε-Caprolactone) Implants: A Novel Strategy for Efficient Intraocular Drug Delivery. *Journal of Controlled Release* **2019**, *316*, 331–348. https://doi.org/10.1016/j.jconrel.2019.09.023.

(10) Castilho, M.; de Ruijter, M.; Beirne, S.; Villette, C. C.; Ito, K.; Wallace, G. G.; Malda, J. Multitechnology Biofabrication: A New Approach for the Manufacturing of Functional Tissue Structures? *Trends in Biotechnology* **2020**, *38* (12), 1316–1328. https://doi.org/10.1016/j.tibtech.2020.04.014.

(11) Diloksumpan, P.; Ruijter, M. de; Castilho, M.; Gbureck, U.; Vermonden, T.; Weeren, P. R. van; Malda, J.; Levato, R. Combining Multi-Scale 3D Printing Technologies to Engineer Reinforced Hydrogel-Ceramic Interfaces. *Biofabrication* **2020**, *12* (2), 025014. https://doi.org/10.1088/1758-5090/ab69d9.